Unsteady Shock Wave Effects on Transonic

Turbine Cascade Performance

by

Jeffrey C. Collie

thesis submitted to the Faculty of the

Virginia Polytechnic Institute and State University

in partial fulfillment of the requirements for the degree of

Master of Science

in

Mechanical Engineering

APPROVED:

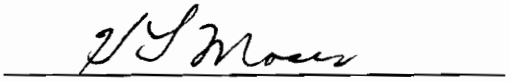

Dr. H.L. Moses, Chairman

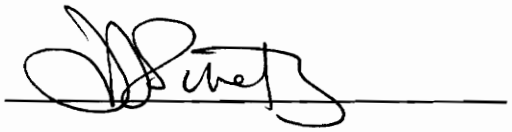

Dr. J.A. Schetz

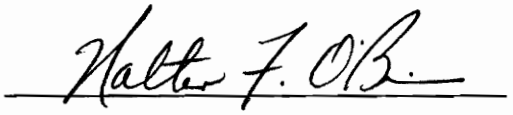

Dr. W.F.O'Brien

September 1991

Blacksburg, Virginia

Unsteady Shock Wave Effects on Transonic

Turbine Cascade Performance

by

Jeffrey C. Collie

Dr. H.L. Moses, Chairman

Mechanical Engineering

(ABSTRACT)

The capability for experimental assessment of unsteady shock wave effects on turbine blade performance has been developed. A novel shock-generation system utilizing a shotgun blast has been implemented into the Virginia Tech Wind Tunnel Transonic Cascade Facility. Specialized optical systems and high-performance pressure instrumentation were utilized to obtain both qualitative and quantitative information.

Shadowgraph photos of the unsteady shock wave propagation through the cascade indicate presence of a vortical region and its movement from the blade surface into the passage flow. A previously unseen distortion of the trailing edge shock wave is also identified. High-frequency blade surface pressure measurements reveal large fluctuations in surface pressure during shock passage. An estimate of unsteady blade lift is made which reveals a 120 percent peak-peak variation. Furthermore, an approximated loss coefficient was determined to fluctuate as much as 40 percent near the blade passage center. Comparisons are made with previously-published experimental and analytical results.

Acknowledgments

Thanks, first of all, to my wife Renée, who has patiently supported my pursuit of a master's degree at the expense of her own career advancement. She also proved to be a great lab helper and thesis typist — what a woman!

Thanks also to my committee members, Dr. Moses, Dr. Schetz, and Dr. O'Brien, whose excellent technical advisement I have greatly appreciated. Additional thanks go to the General Electric Aircraft Engine Company in Cincinnati, Ohio, for supporting this research. Specifically, Monty Shelton, Brent Gregory, and Hardev Singh have each assisted in preparation of this thesis.

Without the help of my fellow graduate students, this project certainly would not have been possible. Thanks to Tibor Kiss, Roger Doughty, and John Mills for their help with running the various tests; to John Alday for his assistance with the LeCroy system; to D.J. Osborne and Marybeth Morris for their instruction on operating the graphics software; to Chuck Wood and Ken Chadwick for computer help; and to all of the others who have assisted in so many ways.

I am greatly indebted to all the support guys from the mechanical and aerospace departments: Andy, Johnny, Jerry, Red, and Shorty from the ME machine shop; Jake, Kent, and Frank from the AOE machine shop; Gary Stafford, our tunnel technician; Billy,

Frank, Ben, and Randy from the ME instrument shop; and Bob Lineberry from the EE computer lab for his help with the time-delay circuit. Their assistance in developing all of the necessary hardware is truly appreciated.

Finally, thanks to Dr. Ng for use of his computer equipment; to Mr. Sittler for working so diligently to ensure that we always had a paycheck; and to Mrs. Riess, Lynn, Cathy, Caroline, Willie, and Jean for their superb administrative and clerical assistance.

Table of Contents

List of Figures

1.0 Introduction

During the past decade, aircraft gas turbine engine designers have become increasingly interested in unsteady effects on turbine blade performance. Numerous studies have been published which indicate that unsteady flow phenomena in the turbine stages have significant effects on blade performance. As a result, the general design assumptions of steady or quasi-steady flow have fallen under increasing scrutiny. In response to these relatively new findings, turbine blade designers are currently attempting to incorporate knowledge of unsteady flow behavior into new designs. Therefore, the demand for experimental data on unsteady phenomena in turbine stages has risen dramatically.

As described by Doorly [1], three major sources of flow unsteadiness exist in the interaction between adjacent turbine rotor and stator rows. Two of these, potential interaction and wake-passing effects, have received considerable attention in published literature (see chapter 2 for more detail). The third source of unsteadiness, shock-wave passing, has received somewhat less attention, especially in the areas of blade lift and profile loss. Therefore, it was the purpose of this research effort to develop an experimental method for advancement of the current understanding of unsteady shock wave effects on transonic turbine blading.

Shock waves produced at the trailing edges of transonic turbine rotor and stator blades impinge directly on the downstream blade row in an unsteady fashion. This periodic "chopping" of blades through the shock waves has been shown to have considerable effects on blade surface pressures and heat transfer [1-6]. It has been proposed by Giles

[6] that significant fluctuations in blade lift and a subsequent increase in stage loss may also result from this unsteady shock wave passage. In any case, very limited experimental information is currently available concerning unsteady shock effects on blade lift and loss.

The use of fully-rotating turbine rigs for detailed studies of shock wave effects is severely limited by high cost and mechanical complexities. Furthermore, as mentioned by Doorly [7], difficulties in flow visualization and instrumentation of rotating rigs are additional handicaps. Researchers at Oxford University have proven the capabilities of a rotating bar shock generator in simulating the unsteady shock wave propagation of an actual transonic turbine engine [1-5,7]. It was therefore the purpose of this Virginia Tech research project to develop a similar or alternate means of simulating the shock wave / blade interaction. The scope of this project included development of the shock generation method for implementation in the Virginia Tech Wind Tunnel Transonic Cascade Facility. Although conclusive results of shock wave effects on blade lift and loss were desired, it was understood that the major research emphasis was to be placed on developing a capable means of simulating the shock waves and photographing the shock propagation through the turbine blades.

2.0 Literature Review

As mentioned in the previous chapter, turbine stage flow unsteadiness originates from three general sources — potential interaction, wake passing, and shock wave propagation. Numerous studies have been published concerning unsteady potential and wake effects, somewhat fewer on shock effects, and still fewer concerning the effects of unsteady shock waves on blade lift and loss. Included below is a survey of work related to each of these fundamental areas. As may be expected, emphasis is placed on the shock wave-related literature because of its relevance to the present study.

2.1 Potential Interaction

As Doorly [8] explains, this form of unsteadiness stems from the relative motion between adjacent rotor and stator rows which results in a periodically varying inviscid flowfield for each blade. The extent of variation is inversely proportional to the row spacing. Studies on the potential interaction may be found in References 9-17, among others.

2.2 Unsteady Wake Effects

Associated with each turbine blade, whether rotating or stationary, is a low velocity wake region emanating from the trailing edge. As the downstream blade row periodically

"chops" through the wakes of the blades directly upstream, they are subjected to varying inlet velocity, flow incidence angles, and turbulence. Studies of unsteady wake effects are included in References 1,2,4,7,8, and 18-27, as well as various other publications.

2.3 Unsteady Shock Effects

In the case of turbine stages operating transonically, shock waves are produced at the trailing edges of both stator and rotor blades. These shock waves extend downstream and impinge directly on the succeeding blade row in an unsteady manner. Shock waves from the rotor blades travel with the blades, therefore impacting the downstream stator row periodically at the rotor blade passing frequency. In a similar fashion, rotor blades periodically "chop" through the stationary stator shocks, also at the rotor blade passing frequency. Needless to say, this shock behavior creates an extremely unsteady flowfield for the rotor and stator rows, affecting the blade performance in numerous ways.

Literature dealing with experimental studies of the effects of unsteady shock passing has been limited to the published works of researchers at the Oxford University Isentropic Light Piston Tunnel [28,29]. Beginning in the early 1980's, several studies at this facility have been published concerning unsteady shock effects as measured using a rotating bar shock generator [7,30]. The first of these studies, by Doorly and Oldfield [7], was conducted on a stationary cascade of first-stage turbine rotor blades. Shock waves produced by the upstream stator row in an actual engine were simulated using the rotating bar shock generator, a circular array of stranded steel wires spun at supersonic velocities relative to the cascade inlet flow. Heat transfer measurements on the blade surfaces indicated that the shock wave passing contributed to the initiation of turbulent patches in an otherwise laminar suction surface boundary layer.

A more detailed study of shock effects was presented by Doorly and Oldfield [1], using the same experimental arrangement as in Reference 7. This paper includes a relatively detailed analysis of the effect of weak shock waves on blade boundary layer transition and heat transfer. Their results indicate the presence of a "separation bubble", induced by contact of the shock wave with the blade suction surface. A sudden rise in heat transfer on the suction surface is attributed to a turbulent boundary layer patch which remains after collapse of the bubble. They found little effect of direct shock impingement on the heat transfer rate in a laminar boundary layer, and only slightly more in a tripped turbulent boundary layer. This paper also proposed that the shock wave does affect the boundary layer transition process associated with a wake. Several unsteady blade surface pressure plots are included which show pressure spikes due to the weak bow and recompression shock waves produced by the rotating bars.

Ashworth et al. [2], conducted a study at Oxford on a highly loaded rotor profile with stronger shock waves. In this case, the turbulent boundary layer patch was reported to move upstream along the blade surface toward the leading edge — the patch due to the weaker shocks in Doorly [2] was shown to be swept toward the trailing edge. Strong spikes in heat transfer were again attributed to a shock-induced boundary layer separation-reattachment process.

Johnson et al. provide a more complete description of the mechanisms responsible for the shock-induced heat transfer fluctuations [3]. This study presents a new theoretical compression heating model in addition to experimental data obtained with the Oxford rotating bar apparatus. Johnson introduces the idea of "compression heating" which leads to thermal conduction in the boundary layer close to the wall. The rapid pressure fluctuations associated with the shock passing are said to heat the boundary layer fluid by adiabatic compression. This behavior results in high conductive heat transfer at the

surface. Therefore, a theoretical model is described which predicts the fluctuating heat transfer levels using unsteady blade surface pressure data. Johnson concludes the paper with an outline of the various mechanisms which each contribute to the shock-induced heat transfer fluctuation.

Additional information on shock wave effects is presented by Johnson et al. [4]. Unsteady blade surface pressure plots indicate large pressure spikes associated with impingement of the recompression shock wave in addition to small pressure increases from the bar bow shocks. A detailed sequence of Schlieren photos provides an understanding of the shock wave propagation through the cascade. Furthermore, a plot of time-averaged blade lift is included which indicates some reduction in lift due to suction surface shock effects. Johnson et al. [5] offer a new explanation for the heat transfer spikes reported in References 1-3, and 7. In previous studies, the "bubble" identified in Schlieren pictures had been attributed to transient boundary layer separation. Johnson, on the other hand, proposes that a "vortical bubble" results from the shock wave bifurcation which occurs near the leading edge of the blade. The bubble encloses a strong vortex which pulls hot gases from outside the boundary layer to the blade surface, thus creating a sudden increase in surface heat transfer. Further discussion of References 4 and 5 is included in the results section of this thesis.

All discussion of unsteady shock studies up to this point has centered on results obtained in the Oxford University Wind Tunnel facility. It appears that the only additional literature concerning unsteady shock effects on transonic blading is a theoretical study by Giles [6]. Giles used an inviscid numerical code with time-inclined computational planes to model the formation and motion of shock waves. Included in Reference 6 is a sequence of computer-generated pressure contours indicating the behavior of shock wave interaction between subsequent blade rows. Giles' predictions show reasonable

agreement with the Schlieren photos taken at Oxford University. The paper also provides plots of unsteady lift for the rotor and stator blades. In the case of the stator, a 6% peak-to-peak variation is noted. However, the code predicts a 40% peak-to-peak variation in rotor lift, including several abrupt changes. Giles proposes that the highly unsteady lift will be accompanied by an unsteady trailing edge vortex sheet. Dissipation of kinetic energy associated with this vortex sheet may produce substantial loss increases for the rotor blades. Further discussion of Giles' work is included in the results section of this thesis.

It is quite apparent that much work is still necessary for complete understanding of the effects of unsteady shock interaction on transonic turbine blades. In particular, no experimental data exists on unsteady loss for transonic blades under the influence of passing shocks. Therefore, the research presented in this thesis has aimed to develop experimental methods for better understanding of unsteady shock wave propagation and its effects on blade lift and loss.

3.0 Test Facility

As mentioned previously, it was the goal of this research effort to develop an experimental method for advancement of the current understanding of unsteady shock wave effects on transonic turbine blading. The experiment was to be designed for use in the Virginia Tech Wind Tunnel Transonic Cascade Facility in Blacksburg, Virginia. The tunnel is a blowdown type, fed by four large, reciprocating compressors via storage tanks. Flow conditions to the test section are controlled by a pneumatic, electronic feedback-controlled valve. The tunnel is typically capable of 18 second run times. Figure 1 is a schematic of the wind tunnel indicating the main features of the facility. More detailed explanations of the wind tunnel facility are provided by Bertsch [31] and Doughty [32].

The experiment was intended to be general insofar as the turbine blade profile selection. In an actual transonic turbine stage, both the rotor and stator rows experience the effects of unsteady shock waves from upstream blades. Therefore, selection of rotor versus stator blading was not considered to be critical. An existing cascade of turbine blades which had previously undergone steady-state tunnel tests was chosen for this experiment. These blades were approximately one third larger than the turbine rotor blades of a modern transonic turbine engine and were modified at the leading edge for zero degree inlet and incidence angles in the tunnel. Figure 2 is a plot of the blade surface Mach number distribution under steady flow conditions.

Figure 3 shows a schematic of the cascade test section. As indicated, the vertical cascade consists of eleven blades numbered 1 to 11 from bottom to top. Blade passages are lettered A to J, also from bottom to top. Also shown on Fig. 3 are two sets of static pressure taps located just downstream of the cascade in one of the plexiglass endwalls. The taps located 6.35 mm in the axial direction behind the cascade are used to measure the isentropic exit Mach number for each run — this number is computed based on the average of the 13 taps ratioed with the cascade upstream total pressure. The second set of taps shown in Figure 3 was not utilized in this experiment. For information regarding the data acquisition system used to obtain the isentropic Mach number measurement, refer to Bertsch [31]. It should also be noted that the cascade exit Mach number could be set anywhere in the range from 0.7 to 1.35 for any given run.

Figure 4 gives a better indication of the blading geometry used in this experiment. Blade dimensions, as noted on Fig. 4, are axial chord = 3.81 cm, blade spacing = 3.72 cm, and true chord = 4.61 cm. As mentioned previously, the blades are oriented in the cascade for zero degree inlet and incidence angles. Figure 5 is a shadowgraph photo of the blades under steady-state flow conditions at a near-design Mach number of 1.16. Arrows are included to indicate trailing edge shock waves. The reader is warned not to confuse the shock waves with the static pressure tap tubing in the photograph. The nearly horizontal shock waves emanating from the blade trailing edges are the shocks which produce the unsteady effect on the downstream blade row in an actual turbine engine. Corresponding shocks from transonic stator blading would be very similar in structure to the rotor blade shocks of Figure 5.

Again, readers interested in more detailed descriptions of the wind tunnel facility and data reduction techniques are encouraged to consult the earlier theses of Bertsch [31] and Doughty [32]. However, it should be mentioned that, in this experiment, determination

of the cascade isentropic Mach number was the only data reduction technique common to the previous studies at this facility. Therefore, discussions of the mass-averaged loss coefficient and traversing pressure probe found in References 31 and 32 do not apply to the present study. Later sections of this thesis include further explanation of instrumentation used in this experiment.

4.0 Experimental Method

Capability for reliable, steady-state, transonic turbine cascade measurements has existed for the past several years at the VPI Transonic Cascade Facility. Results from previous studies have been published by Collie et al. [33] and Moses et al. [34]. An overall review of the facility and its capabilities is presented by Moses et al. [35]. Furthermore, Doughty et al. [36] includes results from a solidity study in a paper to be published in the near future. However, no capability previously existed for study of unsteady shock wave passing effects on transonic cascades at the VPI facility. Therefore, development of adequate experimental test apparatus was necessary before any data on shock effects could be obtained. This chapter presents an overall review of the hardware development and assessment which was accomplished in preparation for actual wind tunnel test data. Descriptions of several designs and methods which did not perform adequately are included to prevent future workers from repeating earlier failures.

4.1 Optical Systems

In order to facilitate clearer descriptions of test procedures in later sections of this thesis, it is first necessary to introduce the optical systems utilized for assessment of hardware designs. In general, two separate optical systems were applied in the unsteady shock experiments — shadowgraph still-photographs and shadowgraph high-speed movies. These are presented in separate sections below.

4.1.1 Shadowgraph Still-Photographs

As discussed in a later section of this thesis, the various alternatives for simulating the unsteady shock passage all generate shock waves with very high propagation velocities (greater than M=1.0). Obviously, waves moving at these very high speeds are virtually impossible to view with the naked eye. Therefore, in order to assess the characteristics of shock wave propagation, a shadowgraph optical system was developed by the author. By exposing the second derivative of flow density gradients, the shadowgraph technique allows for optical isolation of shock waves from other flowfield phenomena. One vital requirement of the system for the present application was the ability to "freeze" the high-speed propagation of the shock wave so that it could be captured clearly on film. Therefore, an extremely short-duration light flash was required. A Xenon High Intensity Nanopulse System was chosen as the light source. This system consists of a Novatron-789B Nanopulse Lamp and Model-437A Nanopulser as the driver. Features of the Nanopulse system include a 20 nanosecond flash duration, 1.59 mm arc length, and external trigger capability. The combination of short duration flash and nearly "point-source" light allowed the Nanopulse Lamp to perform exceptionally as the shadowgraph system light source.

A schematic of the overall shadowgraph system is shown in Figure 6. As identified on Figure 6, the major components include: the Nanopulser light source; 305 mm diameter collimating mirror; a 152 mm diameter focusing mirror; and a shutterless Polaroid camera. ASA 3000 Polaroid black-and-white high speed film was used for all of the shadowgraphs.

Another major requirement of the shadowgraph system was the capability to accurately synchronize the Nanopulser flashing with any specific position along the shock wave

propagation. This feature would be particularly necessary in obtaining a detailed sequence of shadowgraphs to indicate the shock propagation patterns. Therefore, an electronic time-delay circuit was developed to control the timing of the Nanopulser flash. This circuit was utilized in two distinct configurations. Originally, the circuit was designed to receive activation when the shock wave burst a small strip of foil. This arrangement was used in all pretesting of the shock-generating hardware, and will be discussed more fully in a later section. The second circuit configuration, utilized in the final wind tunnel tests, allowed for activation by a shock wave-induced voltage spike. Again, a more detailed discussion is presented in a later section. In both configurations, the time-delay circuit could be user-adjusted to accurately synchronize the light flash with any desired shock location along its propagation. Furthermore, the time-delay circuits were carefully calibrated on an oscilloscope, enabling the user to correlate a specific circuit delay setting with an actual time value. Electrical schematics of the two time-delay circuit arrangements are included as Figures A1 and A2 in Appendix A of this thesis.

4.1.2. Shadowgraph High-Speed Movies

As an alternative means of obtaining shadowgraph images of the shock wave propagation, shadowgraph high-speed movies were recorded. The advantage of high-speed movies over still shadowgraphs is the capability of the movies to obtain a sequence of pictures showing different shock positions **within the same shock propagation**. In contrast, only a single still shadowgraph could be obtained during each shock propagation. (Processing time, however, is much quicker for the still pictures due to the Polaroid format.)

Shadowgraph movies were recorded using a HyCam II 16 mm high speed rotating prism camera. Maximum framing rate for this model is 11,000 pictures per second in full-frame format. The camera was equipped with a TV-type zoom lens for greater versatility. In contrast to the still-shadowgraph system, movies required a constant high-intensity light source throughout each run. This light was provided by a 100 W mercury arc lamp rated at 170,000 cd/cm^2. The lamp was driven by a 100 W DC power supply containing less than 1 percent AC ripple. Although higher wattage lamps were available, the 100 W model was used due to its small arc size (to better simulate a point light source) and high average luminance.

Figure 7 is a schematic of the shadowgraph movie system. Identified on the schematic are the light source, focusing lenses, collimating mirror, ground glass, and camera. In contrast to the still-picture system, the shadowgraph images for the movie setup were not projected directly onto the film due to its small size (16 mm). Therefore, a plate of ground glass was situated directly behind the test location to provide a projection surface for the images. The camera was subsequently focused at the ground glass.

In order to "freeze" the high-speed shock motion on film, the camera had to be run at its maximum framing rate (11,000 pps). With a minimum expected shock velocity of approximately 335 m/s and an exposure time per frame of 36 microseconds (at 11,000 pps with standard 40 percent cycle time shutter), the shock could be expected to move approximately 1.22 cm during the exposure time of a single frame. Movies taken under these conditions proved unable to adequately freeze the shock motion for meaningful analysis. Therefore, special shutters were ordered to reduce the exposure time to 20 percent or 10 percent of the framing cycle time. Movies taken with each of these shutters suffered from lack of light, and were therefore also unhelpful. Numerous attempts were made to increase the light input to the movie film, including careful arrangement of the

light source / lens system to maximize brightness, searches for better ground glass materials, elimination of the ground glass completely, and adjustment of the camera lens aperture settings. However, no combination was found to produce acceptable high-speed movies. Fortunately, as will be discussed later, very accurate sequences of still photographs were obtained which provide extremely useful information of the shock propagation. It should be mentioned that although high-speed movies were not successful in filming the unsteady shock passage, these movies did prove to be extremely useful in capturing the relatively low-frequency fluctuations of the cascade trailing edge shock waves during "steady" tunnel flow.

If high-speed movies do prove to be necessary in later studies, the author recommends use of a Photec high speed movie camera. Its lower f2.8 internal aperture could allow considerably more light input to the film than the HyCam II camera. Furthermore, an optical arrangement allowing for projections of the shadowgraph image directly onto the 16 mm film might provide adequate light. However, there is a good possibility that light flare may occur, reducing image contrast.

4.2 Shock-Producing Hardware

The Virginia Tech Wind Tunnel Transonic Cascade Facility had previously contained no provision for generation of unsteady shock waves. Therefore, an initial task of the project was to first select, and then design and construct, hardware for unsteady shock generation. The following sections describe the procedures taken by the author for selection, design, fabrication, assessment, and implementation of a shock generating system.

4.2.1 Discussion of Alternatives

Several alternatives for producing unsteady effects in wind tunnels have appeared in previous literature. The sole device for shock wave generation to date was designed by Doorly at Oxford University and is discussed in References 1,7, and 30. This rotating bar shock generator consists of a circular array of stranded steel wires, all cantilevered from a central disk. The device is situated such that the wires pass through the wind tunnel side wall in front of the cascade. An air-driven turbocharger is used to spin the disk at speeds high enough to pass the wires through the tunnel at supersonic Mach numbers relative to the cascade inlet flow. Each wire subsequently generates a pair of shock waves as it passes through the tunnel — a bow shock from its leading edge and a recompression shock slightly behind the bow shock. Accompanying each pair of shocks is a wake, simulating the unsteady flow at the inlet to a turbine stage. The device can also be spun at lower speeds for studies of wake effects only. A similar system has been developed by Dullenkopf et al. and is discussed in the wake-effect study of Reference 20.

The rotating bar shock generator has evidently performed very well, and has led to great advances in the understanding of unsteady wake and shock effects as presented in References 1-5,7,8,27, and 30. However, circumstances of the current VPI study necessitated use of a simpler design to reduce costs and developmental time. This study was intended to be an introductory examination of shock effects and therefore possessed a relatively low budget. The mechanical complexities associated with a high speed rotating mechanism demand time and resources which were simply unavailable to this project.

An alternative means of unsteady wake production has been utilized by Pfeil et al. [21], Priddy and Bayley [37,38], and Liu and Rodi [22]. In each of these cases, a rotating

"squirrel-cage" device was applied. The squirrel cage consists of a circular cylinder of equally-spaced bars which is rotated about an axis parallel to the leading edge of the test model. In none of these studies was the arrangement spun at speeds high enough to produce shock waves. The squirrel-cage design, as applied to shock wave generation, would suffer from similar mechanical complexities as the rotating bar shock generator. Again, time and budget restrictions precluded this device from serious consideration for the VPI study.

Paxson and Mayle [23] utilized a catapult mechanism in their study of unsteady wake effects. This device consisted of a small diameter rod which was projected vertically, upstream of the cascade, by a "cross bow"-like catapult mechanism. Typical speed of the bar was 10 m/s for their experiment. A similar arrangement was considered for the current VPI study. It was proposed that a vertically-spaced "ladder" of bars could be catapulted upstream of the transonic cascade at supersonic relative Mach numbers. However, the idea was abandoned for lack of a suitable means of catapulting the ladder at supersonic velocities.

A shock tube system was also considered as a means for producing unsteady shock waves. Merritt and Aronson [39] demonstrated the capability to fire a shock tube generated shock wave into a supersonic wind tunnel test section for the study of bow wave-blast wave interactions. Utilizing a pressure-burst diaphragm shock tube, they were able to generate variable-strength single shock waves which could be shaped and directed to travel as desired into the wind tunnel. This method of shock generation is limited to single-shot shock production, a disadvantage as compared to the rotating arrangements. However, production of repeatable single shocks could be a workable solution since data from separate shocks could be compared and coupled. Overall, design and construction

of a shock tube system would be less costly and less time-intensive than any of the previously discussed mechanisms.

The final selection of a shock generating method was actually a variation on the shock tube system. The VPI apparatus consists of a standard 12 gauge shotgun which operates in a very similar manner to the shock tube of Merritt and Aronson [39]. The explosion from the shotgun shell creates a blast wave which can be shaped and directed over the cascade test section in the wind tunnel. Just as in the shock tube system, the shotgun produces single shock waves rather than the periodically passing shocks of the rotating arrangements. Very minor modification was necessary to the shotgun itself, and total cost and mechanical complexity of the system is minimal. A detailed discussion of the shotgun apparatus development follows.

4.2.2 Shotgun

A standard 12 gauge single barrel shotgun is used for the experiment. Modifications have been made to the stock of the gun to allow for electronically-controlled triggering. The stock is actually removed from the gun and has been replaced with an AC solenoid actuator. A hand-operated electronic switch (or other switching device) is connected to the solenoid through a small power supply and solid-state relay. Throwing of the switch activates the solenoid which in turn pulls the shotgun trigger via a single-bar linkage. Figure 8 is a photograph of the shotgun in the above configuration.

4.2.3 Experimental Test-Stand

In order to test the effectiveness of the shotgun in generating shock waves, an experimental test stand was utilized. This stand, constructed for use with a previous research project, served to hold the shotgun in position so that shadowgraph photos of the

shock waves could be taken. Figure 9 is a photograph of the test stand with the shotgun in position. As shown in the photo, the shotgun was mounted vertically with the barrel pointed upward. The end of the barrel was situated in an aluminum mounting block which could be tightened to secure the gun. The mounting block was bolted to a larger aluminum shooting block. This shooting block was solid with the exception of a straight-through hole for the shock passage. Figure 10 is a schematic of the mounting and shooting blocks. Both blocks were mounted on the test stand platform as shown in Fig. 9. This arrangement allowed for shadowgraph photos of the shock waves to be taken as the shock exited the shooting block into atmospheric conditions. As will be explained in the following section, no materials of considerable mass were allowed to escape from the shooting block. However, the test stand was equipped with a roof to help contain any shell packing materials within the rig.

4.2.4 Shotgun Shock Wave Production

It was fully expected that the blast of a shotgun shell could produce a shock wave, as evidenced by the explosive sound of the firing. However, very little was known concerning the characteristics of the shotgun shell necessary to produce a shock wave similar in strength to those in the actual turbine engine. Obviously, detonation of an ordinary 12 gauge shotgun shell would release a cluster of steel shot which would be nearly impossible to contain. Therefore, it was necessary to obtain a shell which could produce a blast of sufficient strength without releasing damaging projectiles.

Numerous experiments were conducted with various shell types using the experimental test stand and shadowgraph system. Activation of the time-delay circuit for the shadowgraphs was accomplished using foil-breakage. A small strip of aluminum foil was wired into the time-delay circuit as shown in Figure A1 of Appendix A. The foil

strip was placed directly over the exit of the shooting block using electrically insulated test probes. Upon firing of the shotgun, the blast wave passed through the shooting block, breaking the foil as it exited into atmosphere. Breakage of the foil disrupted the electrical connection, activating the time-delay circuit. The circuit could be adjusted to vary the time between foil breakage and light flashing, enabling shadowgraphs to be taken at various intervals as the shock propagated away from the shooting block. This method provided an excellent means of assessing the characteristics of the shock waves produced by the different shotgun shells.

Initial tests were conducted using Winchester X12-FBL "Popper-Load" blank shotgun shells. These were factory-prepared, smokeless shells intended for field training of hunting dogs. The packing used for these blank shells was a fine granular material called Grex. Although the shell explosion propelled the material out through the shotgun barrel, the packing particles were of small enough mass to prevent any considerable destruction to objects they may have impinged upon.

Figure 11 is a sequence of three shadowgraphs illustrating the shock wave propagation produced by the Popper-Loads. The dark particles beneath the shock wave in each picture are fragments of the foil strip used for light triggering. The highly turbulent flow behind the shock also appears in each photo. It should be mentioned that these pictures show the shock wave as it moves vertically upward, away from the shooting block. Therefore, the lower surface shown in the pictures is the shooting block with the test probes (to hold the foil) fastened at the hole exit. The brighter areas shown in Fig. 11c are due to the combustion flash of the shell explosion, causing overexposure of the film. This phenomena will be discussed more fully in a later section.

Figure 11 clearly indicates the spherical propagation pattern of the moving shock wave. This spherical shape is somewhat different that the spanwise-planar shock produced at the trailing edges of transonic turbine blades (refer to the shadowgraph of Fig. 5 for indication of the actual turbine blade shock shape). Therefore, it was necessary to "planarize" the shock wave to produce a more uniform shock for passage over the cascade blade span. A diverging "shock-shaper" was designed and fabricated to accomplish this goal. A schematic of the shock-shaper is shown in Figure 12. The shock-shaper was designed to planarize the shock only in the blade spanwise direction, therefore the shaper diverges in one dimension only. As shown in Fig. 12, the shock-shaper diverges from 2.54 cm at the inlet to 10.16 cm at the exit. The flat plate at the top of the shaper was added to prevent the shock from "curling" around the edges of the shock-shaper during testing.

Figure 13 is a schematic showing how the shock-shaper was mounted on the shooting block for use on the test stand. A sequence of shadowgraph photos showing the shock propagating away from the shock-shaper exit is included in Figure 14. As in Fig. 11, the dark particles are fragments of the foil strip. These pictures show definite improvement in the shape of the shock wave — the wave is essentially flat over its middle section, better simulating the actual blade trailing edge shock. (The flat plate at the exit of the shock-shaper had not yet been added in the photos of Fig. 14.)

Another crucial requirement of the shock wave generating method was the capability to produce very repeatable shock waves from shot to shot. This was especially important in relying on still shadowgraphs for analysis since only one picture could be taken for each shot. Figure 15 shows shadowgraph photos taken of the shock waves of five successive shots, each at the same time-delay setting. These shadowgraphs were taken with the shock-shaper oriented 90 degrees (about its vertical axis) from the arrangement in Fig.

14. (Notice how the shock wave shape has not been affected in this direction.) Comparison of the Figure 15 photos shows virtually no difference between the shock wave positions or shapes. Only in 15d does the shock appear to have propagated slightly further than in the other photos. These results were very encouraging, demonstrating that the shotgun / Popper-Load combination could produce very repeatable shock waves.

Although the Popper-Load shells seemed very capable of producing repeatable, strong shock waves, a disturbing problem surfaced in shadowgraph photos of the shock after longer propagation distances. As shown in the shadowgraph of Figure 16, the shell packing particles have actually moved out in front of the shock wave, resulting in an unacceptable distortion of the shock. It appears that the momentum associated with the small particles was sufficient enough to overtake the naturally attenuating shock wave. Unfortunately, in the case of the tunnel test section, the shock wave would have to propagate a comparable distance to that shown in Figure 16 before contacting the blades of interest. Therefore, some means of preventing the packing material from escaping the shooting block was absolutely necessary for a "clean" shock propagation.

Several solutions were proposed for the problem of the packing interference, with the first attempt aimed at a piston-type design. This design consisted of a hand-packed shell including shotgun powder and a polycarbonate plastic "sabot". The sabot was a slightly tapered solid cylindrical projectile machined to a diameter slightly less than the shotgun shell diameter. Standard empty shotgun shells were loaded with a specified amount of powder followed by the sabot. Explosion of the powder projected the sabot down the barrel in a piston/cylinder motion. It was hoped that the blast wave would travel ahead of the sabot through the barrel and shooting block. The sabot was caught at the exit of the shooting block by a metal lip, allowing the shock wave to propagate upward, unaffected by the shell residue trapped behind the sabot.

Tests of the sabot idea indicated that a shock wave was **not** generated. Numerous tests were conducted with varying amounts and types of shotgun powder (including Green Dot and Bulls-Eye), but it was evident that adequate pressure could not be generated behind the sabot to allow for proper combustion of the powder. Therefore, use of increasing amounts of powder in the shell simply resulted in more unburned powder residue, with no generation of a blast wave.

A second attempt to correct the shock distortion utilized the sabot in conjunction with a Mylar diaphragm at the exit of the shooting block. Movement of the sabot down the gun barrel acted to pressurize the air behind the diaphragm. When the pressure ahead of the sabot reached the diaphragm bursting pressure, a pressure wave would hopefully be generated from the diaphragm. Tests of this method indicated presence of shock propagation, but of considerably weaker strength than the Popper-Load shocks. Furthermore, adequate repeatability of the shock waves could not be achieved. Repeatability problems were most likely associated with unavoidable variations in the diaphragm material and mounting, variation in shell explosion, and variation in the frictional resistance on the sabot during travel through the barrel. It quickly became evident that the Popper-Load shells would be the best alternative due to the excellent repeatability and shock strength.

Brainstorming sessions were conducted to generate ideas on containing the Popper-Load packing within the shooting block. The most feasible idea consisted of a shooting block designed with a 90 degree bend as shown in Figure 17. The shotgun, mounted horizontally, would fire the shock wave into the shooting block as before. Figure 17 illustrates the movement of the wave through the shooting block. Instead of traveling straight through the shooting block as in the previous design, the shock wave would be forced to turn up 90 degrees. It was proposed that the packing particles would not be able

to negotiate the sharp turn and would instead accumulate at the plugged end of the passage.

Tests with the new shooting block proved that it performed very well. Virtually no packing material escaped from the shooting block in any of the shots. The shadowgraph photo of Fig. 18 was taken using the new shooting block without the shock shaper in place. Comparison with the photos of Fig. 11 indicates that the new shooting block has not adversely affected the shock strength or shape and therefore is an acceptable solution to the packing interference on the shock.

At this point, the shock generation system (with Popper-Loads) was capable of producing strong, repeatable, well-shaped shock waves with virtually no release of packing material. The only problem remaining to be tackled was the shotgun combustion "flash" which resulted in overexposure of the shadowgraph pictures. Figure 18 provides an example of the negative impact of the barrel flash on analysis of the shock propagation. This problem definitely needed correction to produce clear sequences of shock wave shadowgraphs.

A solution was achieved with the introduction of an optical interference filter to the shadowgraph system. Rather than eliminating the flash altogether, the filter simply prevented light produced by the barrel flash from reaching the film. The light output of the Nanopulser has a peak magnitude at a wavelength of approximately 300 nm. However, tests with a 10 nm bandwidth notch interference filter centered at 310 nm indicated that the barrel flash also produced light at this wavelength. Tests were then conducted with a 10 nm bandpass filter centered at 430 nm — these indicated that the barrel flash contained no light of 430 nm wavelength. It was also quite evident that a wider bandpass filter would be necessary to transmit adequate light from the Nanopulser.

Therefore, an Omega Optics 45 nm bandwidth notch interference filter centered at 396 nm was selected due to its relatively wide band and high peak transmittance (50 percent). Furthermore, this filter matched well with the specifications of the film (peak sensitivity at 425 nm).

Figure 19 is a shadowgraph photo of the Popper-Load shock wave with the filter in place. Comparison with the shadowgraph of Fig. 18 (no filter) indicates the tremendous reduction in barrel flash achieved with the filter. Unfortunately, the light from the Nanopulser has been attenuated somewhat, resulting in a shock image of reduced contrast. Nevertheless, the barrel flash had been eliminated from the shadowgraphs and reasonably clear pictures of the high-quality Popper-Load shock wave could now be obtained.

4.3 Shock Velocity Measurements

In order to simulate the unsteady shock effects on typical transonic turbine blades, it was desired to generate shock waves at least as strong as the trailing edge shocks from an actual turbine blade. Previous studies of transonic blades at the VPI facility have shown that the static pressure ratio across the trailing edge shock is approximately 1.3 at design conditions. However, this is a conservative estimate since the pressure measurements across the shock could be made no closer than approximately 3 mm on each side of the shock wave. Pressure measurements obtained immediately on each side of the shock wave would certainly indicate a higher pressure rise.

Accurate measurement of the true pressure ratio across the shotgun-generated shock wave is a somewhat formidable task due to the extremely high-speed propagation. However,

knowledge of the shock propagation velocity could allow for a reasonable estimate of the pressure ratio using normal shock tables. Therefore, a shock velocity measurement apparatus was arranged for use on the experimental test stand. This arrangement consisted of a vertically-mounted flat plate equipped with Kulite XCQ-062 high-speed pressure transducers as shown in Figures 20 and 21. (Discussion of the transducers and related data acquisition system is reserved for a later section.) The flat plate was oriented so that the shock wave traveled out from the shooting block and along the plate surface, passing over the transducers as a nearly normal shock.

The data acquisition system and shotgun were manually triggered simultaneously, allowing high-speed, 200 kHz pressure readings to be recorded as the shock passed over the transducers. Pressure spikes associated with the shock passage were easily and accurately identifiable from the pressure traces. Therefore, the time between shock passage over successive transducers was obtained. Knowing this time and the distance between transducers, shock velocity was computed easily. The excellent repeatability indicated in the shadowgraph photos was confirmed with the velocity measurements. Eight consecutive shocks were measured to have a propagation velocity of approximately 564 m/s, accurate to within ± 30 m/s, after a shock propagation distance of approximately 15.25 cm. The accuracy of the measurements was limited to the 5 microsecond time interval between data points. The tests also indicated that the shock velocity steadily decreased at a rate of 30 m/s every 5 cm.

With the sonic velocity of the test surroundings being approximately 335 m/s, the 564 m/s shock velocity translates to a Mach number of 1.68. Referring to the normal shock tables of Zucker [40], the M=1.68 corresponds to a static pressure ratio of approximately 3.13. Obviously, this pressure ratio is considerably greater than the conservative estimate

of 1.3 mentioned previously. Therefore, the shotgun-generated shock wave, as desired, is at least as strong as a realistic estimate of an actual blade trailing edge shock.

4.4 Tunnel Mounting of Shock Generation System

The preliminary testing described in the previous sections has proven the capability of the shotgun system to produce shock waves of sufficient strength, repeatability, and shape. Furthermore, the shock wave propagation could now be analyzed using shadowgraph photography as well as high speed pressure transducers. The final step in obtaining actual wind tunnel data on unsteady shock effects was to mount the system for use with the tunnel cascade test section.

In an actual turbine, the relative motion between the stator blade trailing edge shock waves and the rotor blades is such that the waves move from the suction side of the rotor blades toward the pressure side. Proper simulation of this movement in the wind tunnel requires passage of the shock wave from top to bottom of the cascade. Therefore, the shotgun system was mounted on the roof of the test section as shown in the schematics of Figures 22 and 23. Figures 24 and 25 are photographs of the tunnel-mounted shotgun system, Fig. 24 being an overall view and Fig. 25 a close-up of the shooting block and shock-shaper. Comparison of Figures 22 and 17 illustrates the similarity between the tunnel-mounted system and that of the experimental test stand. The shooting block is somewhat smaller in the tunnel-mounted system in order to reduce the weight supported by the shock-shaper. The shock-shaper shown in Figures 22-25, incidentally, is the same design as that shown previously in Fig. 12.

The shock wave produced by the tunnel-mounted shotgun system entered the wind tunnel through the test section roof and passed downward just upstream of the cascade. Referring to Fig. 23, the blades of interest were numbers 4 and 5, both of which were instrumented with high-speed pressure transducers as described in the next section. Therefore, the shock wave traveled over 6 complete 3.81 cm blade spacings, for a total of 22.86 cm, before coming into contact with the instrumented blades. No effort was made to control the propagation of the shock wave inside the wind tunnel since the relatively low-speed cascade inlet flow ($M \approx 0.2$) was not expected to substantially affect the propagation. Shadowgraph photos of the shock propagation over the blade row are included in the results chapter of this thesis.

4.5 High-Speed Instrumentation

In order to **quantitatively** analyze the unsteady shock wave effects on the cascade blade row, pressure instrumentation was utilized. Since the passage of the shock wave and its associated pressure fluctuation were very transient in nature, pressure transducers with extremely fast response characteristics were needed. As mentioned previously, the ultimate goal of the study was to establish the capability of assessing unsteady shock effects on blade lift and loss. The obvious method for experimental lift analysis involves knowledge of the unsteady blade surface pressures. Therefore, it was desired to instrument the suction and pressure surfaces of the test blades with pressure transducers. To facilitate mounting directly into the blade surfaces, these transducers had to be very small in size. Therefore, Kulite model XCQ-062 strain gage transducers were chosen for the study. These ultraminiature transducers were a mere 1.59 mm in diameter and 5.08

mm in length. The transducers were rated for 345 kPa maximum absolute pressure and were temperature compensated from –1 to 54 degrees Celsius.

Although the natural frequency of the transducer diaphragm was approximately 600 kHz, the protective screen necessary for wind tunnel application reduced the overall transducer natural frequency to approximately 52 kHz. According to technical representatives from Kulite, the actual useful frequency range is limited to pressure fluctuations below approximately 25 kHz. Unfortunately, prior to testing in the wind tunnel, very little was known concerning the transient nature of the shock-induced pressure fluctuations. Therefore, establishing requirements for transducer performance was virtually impossible. In any case, the Kulite XCQ-062 transducer provides an excellent combination of frequency range and small size and is among the best currently available.

Preliminary testing of the transducers was conducted using the shock velocity measuring system as described in section 4.3. The Kulite transducers were mounted in four locations along the flat plate as shown in Fig. 20. Figure 26 provides a sample pressure trace obtained during the tests. This particular plot was obtained in conjunction with an Ektron instrumentation amplifier (to be described later) at a sampling rate of 200 kHz. The block of data containing the shock pulse is shown, and it clearly illustrates the shock wave pressure pulse.

Four Kulite transducers were flush-mounted in the surfaces of blades 4 and 5 (refer to Fig. 23 for the blade positions). Special care was taken in flush-mounting the transducers to avoid disruption of the normal flowfield. Holes were drilled directly into the blade surfaces for insertion of the transducers, and the transducer wires were routed through shallow channels along the span of the blades. The channels were subsequently filled

with plaster of Paris and carefully sanded smooth. (Small strips of metal were actually placed between the wires and plaster to facilitate removal of the wires at a later time.)

The actual transducer locations on the blades are indicated in Fig. 27. Transducer #1 was located on the suction surface near the leading edge of blade #5. Transducer #2 was located in the pressure surface of blade #5, and transducers 3 and 4 were mounted on the suction surface of blade #4. Each of the transducers was alternately staggered slightly off of the blade spanwise centerline to avoid possible flowfield disturbances produced by the other transducers. Due to the decreasing blade thickness toward the trailing edge, no transducers could be mounted downstream of #4.

Although the surface transducers could provide a reasonable indication of blade lift, measurements of loss had to be obtained downstream of the cascade. For this purpose, an additional Kulite XCQ-062 transducer, identical to the blade surface models, was mounted in a total pressure probe. This probe could be moved vertically downstream of the cascade in any horizontal location. Figure 28 is a photograph of the probe — the transducer was mounted on the end of the small tube shown at the far left. A detailed drawing of the probe (without the Kulite transducer) can be found in Bertsch [31]. The probe transducer will be referred to as Kulite #5 in the remainder of this thesis. Further discussion of the use of Kulite #5 is included later.

4.6 Data Acquisition System

Due to the extremely high speeds of the shock wave propagation across the blade row, careful selection of data acquisition system components was necessary. The overall system is comprised of differential instrument amplifiers, data acquisition hardware,

digital oscilloscope software, and a computer. The following sections describe each of these components further.

4.6.1 Data Acquisition Hardware

Although prediction of the actual shock pressure pulse rise time was virtually impossible without knowledge of the exact shock structure, an estimate of ten microseconds was used. Therefore, in order to obtain at least two data samples during the pressure rise, a sampling rate of 200 kHz would be necessary. Fortunately, an excellent stand-alone data acquisition system was available for use in this experiment. This LeCroy Model 6810 Waveform Recorder is a transient recorder which samples an analog signal at a prescribed sampling frequency, digitizes the samples, then writes the data to digital memory. It can accept up to 4 input channels and may be programmed for 1-channel sampling up to 5 megasample/sec., 2-channel sampling up to 2 megasample/sec., or 4-channel sampling up to 1 megasample/sec. Obviously, this machine easily met the sampling frequency requirements of the experiment.

A major consideration in choosing a data acquisition system was the need to synchronize and compare the data from the various transducers. Since the propagation rate was so high, slight time inconsistency between transducers would wreak havoc on data comparison and correlation with the shadowgraph photos. The LeCroy 6810 utilizes a multiplexing system, but not to the detriment of the data sampling. This is accomplished by Hybrid Instrumentation Amplifiers for each data channel which are **simultaneously** sampled by a unity gain Track and Hold. An analog multiplexer services the Track and Hold and sends the data to the 12-bit ADC on a separate board. Therefore, although the data channels are multiplexed, they are first sampled simultaneously, allowing precise synchronization and comparison of data from the separate transducers.

4.6.2 Computer

An IBM AT equivalent computer was used for data storage and operation of the digital oscilloscope software. It is a 286 machine with 12 MHz clock speed. The computer contains an 80287-10 math coprocessor, an 8 Megabyte hard drive, 2 floppy drives, and a GPIB interface card.

4.6.3 Digital Oscilloscope Software

Digitized data output from the LeCroy 6810 Recorder was retrieved using LeCroy Waveform-Catalyst Multichannel Digital Oscilloscope software. This software package was developed specifically to control, display, store, and process data from LeCroy Modular Waveform Digitizers. The package can be used to display 1 to 4 channels of data simultaneously on a monitor. Traces can be easily expanded or zoomed in voltage and time, and dual cursors are available for rapid comparisons. More complete information involving Waveform Catalyst features can be found in the user's manual.

4.6.4 Differential Amplifiers

Voltage output levels from the Kulite transducers were of relatively low values (0 to 100 mVolts). In order to better fill the input range of the LeCroy ADC (for better resolution), it was necessary to amplify the voltage input to the ADC. This was accomplished using Ektron Model 562 differential DC amplifiers for each transducer. One of the important considerations in selecting an amplifier was to ensure that it could respond quickly enough to avoid distortion of the shock pulse. Tests were conducted on several differential amplifiers to determine which most accurately reproduced the unamplified signal from the transducer. These tests, performed using the shock velocity measuring system, indicated a shock pulse rise time of approximately 30 microseconds with no

signal amplification. The signal produced using the Ektron amplifier with a gain up to 5 corresponded almost identically (except in magnitude, of course). Amplifiers by Tektronix and Gould showed somewhat slower response, with rise times between 60 and 80 microseconds. Therefore, the Ektron amplifiers were the clear choice for this application. A separate 5V DC power supply was used to provide excitation to the Kulites.

4.6.5 Filtering

Prior to the actual wind tunnel testing of the unsteady shock effects, very little was known concerning what to expect from the unsteady pressure trace behavior. It was virtually impossible to predict the frequency composition of the shock-induced pressure fluctuations. Therefore, no pre-filtering was utilized in any of the data presented in this thesis. Data recorded during the wind tunnel tests do indicate some pressure fluctuations which may not represent actual flow behavior. Therefore, future work with this data acquisition system will most definitely utilize some form of pre-filtering.

4.7 Wind Tunnel Test Methods

With the shock generation system completed and mounted in the wind tunnel, and all preliminary instrumentation testing concluded, actual wind tunnel testing could begin. As mentioned previously, still shadowgraphs and unsteady pressure data would be the analysis tools for studying the effects of shock passage. The remainder of this section provides specifics regarding various elements of the wind tunnel tests.

During preliminary tests, shadowgraph photos were taken using a foil-trip triggering system to activate the Nanopulser light source. The arrangement of the shooting block in

the preliminary tests allowed the foil strip to be placed directly across the shooting block exit hole. In the case of the wind tunnel tests, it would be inconvenient, at best, to install the foil strip in the shotgun system. Therefore, the time-delay circuit was modified, as shown in Figure A2 of Appendix A, to allow for an electrically-activated trigger. Specifically, the output from Kulite #1 (refer to Fig. 27 for location) was supplied to the time-delay circuit. Triggering of the light source occurred when the voltage output from the transducer exceeded a user-specified value. Thus, the sudden shock-induced voltage spike was utilized to trigger the light source through the variable time-delay circuit. This method worked extremely well but did not allow shadowgraph photos to be taken of the propagation until the shock wave reached Kulite #1. In fact, inherent delay in the time-delay circuit prevented triggering of the Nanopulser until the shock wave had traveled into the passage between the instrumented blades. Fortunately, the tunnel viewing window was large enough to photograph an adequate portion of the shock propagation across the cascade. A sequence of shadowgraph pictures taken with this arrangement is presented in Chapter 5.

No attempt was made to synchronize the beginning of data acquisition with any particular shock location. The data acquisition system was simply triggered using the manually-operated electric switch which also fired the shotgun. At the 200 kHz sampling rate used in the tunnel tests, the LeCroy's 2 megasample memory allowed recording of data on four channels for up to 2.5 seconds. This was certainly enough time to capture the complete extent of unsteady shock effects.

Originally, pressure data **and** shadowgraph photos were recorded in each run. However, the large power surge associated with firing of the Nanopulser light source adversely affected the data recording, causing large apparent discontinuities in the data. Therefore, subsequent data recording was performed with no shadowgraph photos.

All tests were run at approximately the cascade near-design Mach number of 1.16. Since the LeCroy system allowed for only four input channels, four transducer signals were recorded during each run. Unfortunately, problems with the data acquired from Kulite #3 rendered it virtually useless. Therefore, no data from Kulite #3 is presented in Chapter 5.

All data for Kulites 1, 2, and 4, as presented in Chapter 5, corresponds to the transducer locations as specified in Fig. 27. Kulite #5 was located 6.35 mm in the axial direction downstream of the cascade trailing edge. Data was recorded for Kulite #5 in ten vertical positions over one complete blade spacing. Plots of Kulite #5 pressure data for the various vertical positions are also included in Chapter 5.

5.0 Experimental Results

This chapter contains the presentation and discussion of all experimental data and shadowgraph photos. Data includes unsteady blade surface pressure at three locations, approximate unsteady blade lift, downstream unsteady total pressure, unsteady wake pressure profiles, and estimated unsteady profile loss. Comparisons are made with other related studies wherever applicable. It should be kept in mind that this data is an introductory step into the experimental analysis of shock effects on transonic turbine blade lift and loss. The rough estimates presented for unsteady "lift" and "loss" are not intended to uncover the full picture of blade lift and profile loss. However, they do provide extremely useful insight into the capabilities of analyzing these parameters in a transonic cascade facility with relatively simple shock generation equipment.

5.1 Zero Time Base

To facilitate comparison of all forms of data and shadowgraphs, a "zero time base" was established. As a matter of convenience, time-zero was chosen to be the time when the shotgun-generated shock wave first contacted Kulite #1. This time could easily be identified on the pressure data for all transducers since Kulite #1 data was recorded for

every run and all data channels were sampled simultaneously by the LeCroy (as discussed in section 4.6.1). Furthermore, since the shadowgraph light source was triggered by Kulite #1, accurate calibration of the time-delay circuit allowed for establishment of a corresponding time-zero in all photos. Therefore, all time values appearing in the shadowgraphs and plots of Chapter 5 are based on the identical time-zero, permitting direct comparison of the entire set of results.

5.2 Shadowgraph Photos

Shadowgraph photos of the shotgun-generated shock wave passage through the cascade were taken using methods described previously in sections 4.1.1, 4.2.4, and 4.7. Figure 29 shows a preliminary shadowgraph photo of the cascade test section with no flow or shock generation, and without use of the optical interference filter. Obviously, the barrel flash has rendered the picture useless. Figure 30 is a repeat of Fig. 29 except that the filter was utilized in this shadowgraph. The barrel flash is no longer a problem, but the picture now suffers from a lack of brightness and contrast. Fortunately, use of the optical filter was discovered to be unnecessary for shadowgraphs of the cascade during tunnel blowdown — the flow through the cascade somehow prevented the barrel flash from expanding down into the test section. This was an extremely fortuitous circumstance, for it allowed shadowgraphs of the shock propagation during tunnel flow to be obtained without use of the filter.

Figure 31 is a sequence of fifteen shadowgraphs which capture the unsteady shock propagation through the cascade. The cascade isentropic exit Mach number was

approximately 1.16 in all of these photos. In all cases, the two blades pictured fully are the instrumental blades (#4 and #5 as shown in Fig. 23). Figure 31a shows the cascade under steady flow with no shock generation. The pair of trailing edge shock waves from each blade are clearly evident. Furthermore, the pair of thick dark lines positioned vertically behind the cascade are shadows of the wall static pressure taps and tubing (refer to Fig. 3 for location of these taps). It should be noted that the thin dark line positioned nearly vertically and passing through each of the passages is unfortunately a scratch in the plexiglass cascade endwall. (Be careful not to confuse this scratch with any of the shock waves shown in the Fig. 31 pictures.) Finally, a discontinuity in the suction surface of blade #5 at approximately $X/C_{ax} = 0.5$ produces a Mach wave which appears in all of the shadowgraphs. Please avoid confusion of this wave with the unsteady shotgun-generated shock wave.

In order to facilitate discussion of the unsteady shock propagation, the illustration of Fig. 32 is included. Adapted directly from the shadowgraphs of Fig. 31, Fig. 32 provides a clearer representation of the shock propagation. It is especially helpful considering the complexity of the propagation patterns. In all of the Fig. 32 sketches, the blades shown are the instrumented blades #4 and #5. Only one blade passage is shown in Figure 32 to avoid confusion. However, it should be kept in mind while studying Fig. 32 that shock activity does occur simultaneously above and below these blades, as shown in Figure 31. In fact, due to excellent periodicity between passages, information from passages E and F (refer to Fig. 23) is actually incorporated into Fig. 32. Therefore, frames l-q of Fig. 32 are actually "extrapolated" from the shock patterns of the upper passage shown in earlier frames. The small arrows included in Fig. 32 illustrate the direction of shock movement within each frame.

Figure 32a shows the earliest position in the propagation sequence which could be captured by the shadowgraph system. The primary shock wave, labeled *a*, is positioned within the passage, and a small reflection *b* is formed at the pressure surface impingement point. The shock which branches from the primary shock at the left of Fig. 32a, labeled *d* is a reflected wave and will be discussed below. In Fig. 32b, the primary shock *a* has now moved down into contact with the suction surface crown of the lower blade. As indicated, a reflected wave *d* is formed which begins to move in the direction opposite to the primary shock. At this point, the primary shock has been divided, with segment *a* moving along the suction surface toward the leading edge and segment *e* toward the trailing edge.

Figure 32c shows the shock positions 25 microseconds later. The primary wave *a* is now positioned at the blade leading edge with the reflected wave *d* having moved back fully into the passage. The second segment *e* of the primary shock has now propagated to nearly the end of the passage, with its pressure surface reflection *b* seemingly larger at this time. At time = 108 microseconds, Figure 32d shows the primary shock *a* to have moved around the leading edge of the lower blade. A shock bifurcation *f*, as discussed thoroughly by Johnson et al. [4 and 5], is clearly evident. This bifurcation developed as the angle of the reflected shock *d* with the blade suction surface grew dramatically near the leading edge. Also in Fig. 32d, the reflected wave *d* has moved completely across the passage and is now in contact with the pressure surface of the upper blade at *g*. A second reflection *h* occurs at the pressure surface and is shown to move back in the direction of the lower blade. Segment *e* of the primary shock wave has moved out of the passage and is shown at the rear suction surface of the lower blade, approaching the trailing edge.
Figure 32d also indicates the development of a small region of interest, labeled *i*, on the pressure surface near the upper blade leading edge. This region is consistent with the

"vortical bubble" formation as discussed fully by Johnson et al. [5]. As described by Johnson, the shock wave bifurcation at the leading edge produces a vortex sheet which rolls up and attaches to the blade leading edge. Depending on the leading edge blade geometry and other factors, this vortical region is convected back along either the pressure or suction surface. Johnson proposed the vortical bubble idea as an explanation of the large heat transfer spikes found in References 1-4. The powerful vortex contained within the vortical region acts to pull hot gases from the free-stream flow into the boundary layer. This argument was in contrast to earlier explanations by Doorly and Oldfield [1] which described the region as a "separation bubble".

Figure 32e, at time = 121 microseconds, shows the primary shock *a* approximately one complete blade spacing below its location in Fig. 32a. The reflected shock *d* which began at the crown of the suction surface in 32b has moved almost completely out of the passage, with its second reflection *h* shown almost in contact with the suction surface once more. Figure 32e also indicates the first unsteady shock effects on the steady-state trailing edge shock waves. It appears that the steady shock *j* which impinges on the suction surface of the lower blade has begun to bend out toward the rear of the passage. This trend continues in the succeeding frames.

It may have become evident to the reader that the vortical region *i* shown in Fig. 32e does not appear in the corresponding shadowgraph of Fig. 31f. In fact, the vortical region does not reappear in the shadowgraphs until Fig. 31i. However, a set of shadowgraphs taken with the optical interference filter indicates presence of the region clearly throughout this time. Although these shadowgraphs were not of high enough quality to permit inclusion in this thesis, they did provide the information necessary to illustrate the vortical region location in Figures 32e-32g.

Subsequent shock reflections and re-reflections are apparent in the blade passage until a time of approximately 353 microseconds (Fig. 32m). A description of this shock activity is not included in lieu of the detailed illustrations of Fig. 32. However, several characteristics of the shock behavior which are particularly notable include:

1. the movement of the vortical region away from the pressure surface and into the blade passage as shown in Figures 32i-32l;

2. the repeated reflection of shock waves across the blade passage with continually decreasing shock strength;

3. the continuing movement of the lower steady-state trailing edge shock *j* toward the rear of the cascade. This shock becomes almost vertical, as shown in Fig. 32m, and finally recovers back to its original position at time = 510 microseconds. Furthermore, as shown in Fig. 32i, the reflected steady-state shock *k* actually divides, with segment *l* soon disappearing from view.

Overall, the results presented in Figures 31 and 32 agree quite well with the findings of Johnson et al. [4]. Figure 33 is an illustration from Reference 4, included for comparative purposes. It should be kept in mind that the results from Oxford University were obtained using the rotating bar shock generator which produces two separate shock waves from each bar. The shotgun method employed in the VPI study generates only a single shock wave. Several differences do exist between results of the present study and those from Reference 4. As shown in Fig. 33.2, the reflection labeled *c* forms a "lambda"-type shock as discussed more fully by Johnson et al. [5]. Although a reflection *b* is evident in Figures 32a-32c, it appears to be a regular reflection rather than a lambda shock. However, no "zoomed" shadowgraphs of this pressure surface region were obtained in the present study as they were in Reference 4 — it is quite possible that the lambda

reflection may actually be present and could be apparent in a higher-resolution shadowgraph. These reflections behave otherwise similarly between the two studies.

Other discrepancies occur due to the differences in leading edge geometry of the two studies. Comparing Figures 32c and 33.2, the reflections *d* lie in approximately similar positions, whereas the location of the primary shock *a* relative to the blade leading edge is obviously different. Furthermore, comparison of the reflected waves *h* in Fig. 32 and *l* in Fig. 33 reveals slight differences in their propagation patterns. Finally, Johnson et al. [5] identify presence of the "vortical bubble", as mentioned previously, but give no indication that it moves off of the pressure surface and into the passage freestream flow. Results of the VPI study clearly indicate separation of the vortical region from the pressure surface, as illustrated in Figures 32i-32l. It is quite possible that the difference in leading edge geometry may again be responsible for the apparent variation.

Another notable discrepancy between the results of the two studies concerns the unsteady effects on the behavior of the steady-state trailing edge shock wave. Johnson et al. [4,5] make no Reference to any fluctuation in the trailing edge shock waves during the unsteady shock passage. As noted previously, results of the present VPI study indicate strong effect on the trailing edge shock wave *j* in Fig. 32. However, discussion included in References 4 and 5 is limited to a shorter portion of the shock passage cycle than that contained in Figures 31 and 32 of this thesis.

No other experimentally-based illustrations or pictures of the unsteady shock propagation appear in previously published literature. Giles [6], however, presents numerically-generated results based on the unsteady inviscid Euler equations. Figure 34, taken from Reference 6, shows reasonable agreement with the results of this thesis as presented in Figures 31 and 32. Giles' results do show somewhat fewer shock reflections within the

blade passage during the unsteady shock cycle. Furthermore, Giles makes no mention of the vortical region, the lambda shock, or any trailing edge shock fluctuations. Further discussion of Giles' results is contained in sections to follow.

5.3 Unsteady Blade Surface Pressures

5.3.1. Surface Pressure Traces

As explained previously in section 4.7, unsteady blade surface pressure measurements were obtained at the locations as specified in Fig. 27. Data from Kulite #3, however, is not presented due to spurious electrical fluctuations which rendered it useless. Figures 35-37 are plots of the surface pressures from Kulites 1, 2, and 4, respectively. In each of these plots, **absolute** pressure is plotted in kPa and time in milliseconds. As described in section 5.1, time-zero is identical in all plots as well as in the shadowgraphs and illustrations of Figures 31 and 32. Figures 35a, 36a, and 37a each show pressure from time = –0.25 msec to time = 1.75 msec. The traces are continued to time = 3.75 msec in part *b* of each figure. No significant data fluctuations occurred at times greater than 3.75 msec for any of the transducers.

Due to the consistency in time-zero throughout the data, the pressure histories from Figures 35-37 can be correlated with the illustrations of Fig. 32 to aid in identifying the various pressure peaks. Therefore, appropriate illustrations have been included on Figures 35-37, identifying the shock positions responsible for the specific pressure spikes noted. All data presented in Figures 35-37 has been ensemble-averaged over 15 separate runs to reduce signal noise. This averaging procedure was accomplished using a point-by-point averaging code created by the author. Although pressure data for each run was

very similar, the averaging technique certainly altered the absolute pressure peak magnitudes found in individual traces. However, the ensemble-averaged plots of Figures 35-37 perform extremely well in isolating specific shock wave phenomena which appear somewhat less clearly in the individual pressure traces.

As indicated on Fig. 35, data from Kulite #1 reveals three distinct shock-induced pressure fluctuations. The first spike, occurring at time = 0.0 msec, results from the passage of the primary shock *a* directly over the transducer face. Subsequent impingement of the reflected shocks *h* and *d* result in two additional pressure spikes of much smaller magnitude as noted. The various other pressure spikes evident on Fig. 35 may be due to actual flow phenomena, but they could not be directly identified with a particular shock position from Fig. 32. Also evident from Fig. 35 is the relatively long period of the unsteady shock effect on the Kulite #1 pressure. The "steady-state" pressure apparent prior to time-zero in Fig. 35 does not recover until approximately 3.5 msec. (To provide some feel for this time duration, it may be informative to note that a fluid particle passing continuously through the blade passage at the cascade inlet velocity of M = 0.2 would travel through the cascade in approximately 0.5 msec. Therefore, the shock effects continue for roughly seven times this period.) Recalling the illustrations of Figure 32, no shock activity could be identified in the passage after approximately 0.35 msec. Obviously, considerable flow disruption continues well past the last indication of actual shock wave presence in the blade passage.

Figure 36 provides the pressure history recorded by Kulite #2. Again, three distinct pressure spikes can be directly identified with particular shock locations. The first of these, occurring at approximately 0.05 msec, is due to the primary shock *a* as it moves along the pressure surface. A second spike occurs approximately 75 microseconds later when the reflected wave *d* reaches the pressure surface at Kulite #2. The third

distinguishable spike occurs when the reflected wave *m* reaches Kulite #2. As in the case of Kulite #1, the steady-state pressure level does not recover until approximately 3.75 msec. Maximum pressure for Kulite #2 is slightly less than for Kulite #1, as is the minimum pressure level. Overall trends in data are comparable between Kulites 1 and 2.

As expected, the pressure levels for Kulite #4, as shown in Fig. 37, are somewhat lower than either of the other two transducers. Two pressure spikes are apparent — the first due to passage of the primary shock segment *e* over Kulite #4 and the second from reflected shock *n*. It was at first somewhat surprising that no pressure fluctuation could be associated with impingement of reflected wave *h* on Kulite #4 at a time of approximately 0.13 msec. However, upon examination of Figures 32e and 32f, it is apparent that the nearly zero angle between shock *h* and the blade surface at Kulite #4 prevents any shock-induced pressure fluctuation. In contrast to the curves of Figures 35 and 36, Fig. 37 shows Kulite #4 to recover to its steady-state pressure level in only 1.75 msec, nearly twice as quickly as the other two transducers. Furthermore, it is apparent that the pressure drops only slightly below the steady-state value, also in contrast to Kulite #1 and Kulite #2.

Researchers at Oxford University have presented numerous unsteady blade surface pressure traces [1-5]. Each of these plots was based on the shock wave effects as generated by the rotating bar generator. As discussed in section 4.2.1 of this thesis, the rotating bar actually generates a pair of shock waves with an expansion region in between. Therefore, since the shotgun generates a single shock, comparison of the Oxford pressure results with those of the present study is severely limited. Perhaps the only safe comparison between the two is that both do contain shock-induced pressure spikes.

5.3.2 Unsteady Blade Lift

Obviously, a complete picture of the unsteady lift during the shock passage cannot be obtained from only three surface transducer locations. However, budget restrictions precluded full instrumentation of the blade surfaces. Therefore, a rough estimate of the unsteady lift fluctuation was composed from the unsteady pressure difference between Kulites 2 and 4. (It is worth mentioning that, from an incompressible viewpoint, a line through the locations of Kulites 2 and 4 on a single blade approximately parallels the direction of mean blade lift.) Figure 38 is a plot of the unsteady pressure difference between Kulites 2 and 4. Figure 38a includes the pressure difference from time = –0.25 msec to 1.75 msec with a continuation on Fig. 38b to time = 3.75 msec. The trace of Fig. 38 is actually the difference between the plots of Figures 36 and 37 and therefore also represents an ensemble-average. Additionally, the appropriate 80 microsecond time offset was applied to the data of Kulite #4 to compensate for the fact that Kulites 2 and 4 were mounted on different blades. Evident from Fig. 38 is the approximately 120 percent peak-peak variation in "lift". Furthermore, abrupt changes in lift occur at several times during the shock passage.

Although no other experimental data concerning unsteady lift has been previously published, Giles [6] presents a curve of unsteady rotor lift based on his numerically-generated inviscid code results. Giles notes a 40 percent peak-peak variation in lift with several abrupt changes also present. He proposes that an additional loss mechanism may be directly attributable to the unsteady blade lift. As described by Giles, an unsteady vortex sheet would be associated with the variation in lift. The kinetic energy contained in this unsteady vortex is eventually dissipated downstream of the blade row, leading to additional losses. Giles proposes that this loss is proportional to the square of the unsteady lift, and thus may be a substantial contributor to overall unsteady profile loss.

Although the experimental unsteady lift presented in Fig. 38 is certainly a rough approximation to the actual blade lift, it nevertheless conclusively indicates that strong variations in lift do exist. It is also evident in Fig. 38 that the lift does not recover to its steady-state value until approximately time = 2.25 msec. As Giles [6] adds, the possible structural excitation which may be induced by the cyclically varying lift could also become detrimental to turbine performance.

5.4 Downstream Pressure Measurements

5.4.1 Traversing Probe Pressure Traces

The other form of pressure data recorded in the wind tunnel during unsteady shock passage was the downstream total pressure from Kulite #5. As described in sections 4.5 and 4.7, the Kulite #5 probe could be traversed vertically downstream of the cascade and was therefore used to record data in ten vertical locations over one complete blade spacing. Figure 39 is a plot of raw absolute pressure data from Kulite #5 in the position as noted on the insert. Again, time-zero corresponds exactly to that of all previous data and shadowgraphs. Obviously, signal noise is relatively high in the data of Fig. 39. Therefore, a code was written by the author to boxcar-average the Kulite #5 data. A running ten-point average, as shown in Fig. 40, proved to be the best compromise between high noise and loss of meaningful pressure behavior. Admittedly, the data as presented in Fig. 40 may not represent a totally accurate picture of the downstream total pressure — pre-filtering would certainly be a better alternative for future work. However, it is felt that the ten point average has preserved the major trends in pressure fluctuation and serves well the purposes of this introductory study.

At this point, it should be mentioned that interpretation of the Kulite #5 data should be subject to additional scrutiny. Since the probe was positioned in supersonic flow, a bow shock existed at the transducer face. No correction for the pressure drop associated with this bow shock has been made for the Kulite #5 data. Furthermore, Merritt and Aronson [39] have shown that the behavior of a blast wave / bow wave interaction is indeed quite complicated. Therefore, the interaction between the unsteady shock wave and the probe bow shock may have influenced the pressure readings somewhat. Although the extent of influence was impossible to predict from the information obtained in this experiment, it is safe to say that rarefaction waves were most likely generated by the blast wave reflection. These rarefaction waves would have resulted in pressure drops not ordinarily present in the flowfield. An extensive analysis of this blast wave / bow wave interaction was not in the scope of this project, but it should be considered if future work involves this method of pressure measurement.

Evident from Fig. 40, the downstream total pressure undergoes severe variations during the unsteady shock passage. As indicated on the Fig. 40 insert, for this data the probe was positioned just above the wake of blade #4. Small fluctuations in the total pressure are still evident after 7 msec, considerably longer than the effects seen on the blade surfaces in Figures 35-37. The data shown in Fig. 41 was obtained with the probe situated exactly one blade spacing above that of Fig. 40. The reasonable periodicity between the two is clearly evident. Included in Appendix B is the full series of plots showing the probe at ten locations within the blade spacing. The equally-spaced probe positions are numbered 0 to 9 from bottom to top. Similar trends can be found in all of these curves.

Wake plots were generated by "time-slicing" the unsteady total pressure traces at the ten vertical locations, again numbered 0 to 9 from bottom to top. This procedure consisted of

extracting the data point corresponding to a specific time from each of the ten pressure curves to construct a single trace for that specific time. Figure 42 presents the wake plots corresponding to three distinct times: time = –0.03 msec, 0.22 msec, and 1.47 msec. The first of these represents the steady-state wake profile, whereas the other two show the overall maximum and minimum variations, respectively. The steady-state profile (time = –0.03 msec) indicates trends as expected — the minimum pressure appears at position #7, directly in the blade wake. However, at other times shown, the trend of the steady-state profile has obviously disappeared. In fact, the minimum pressures at 0.22 msec and 1.45 msec occur near the center of the blade passage. Included in Appendix C is a more complete set of wake plots from time = –0.03 msec to 6.97 msec. These curves indicate the continuing variation in wake profile throughout this time period.

5.4.2 Unsteady Cascade Loss

In order to approximate the unsteady blade profile loss, estimates were made for the cascade pressure loss coefficient as defined by $(P_{t,inlet} - P_{t,\ exit})/P_{t,inlet}$. Although actual unsteady inlet total pressure was not recorded during the tests, an approximation was made using the unsteady, ensemble-averaged Kulite #1 data as plotted in Fig. 35. This was considered to be a reasonable estimate since Kulite #1 was located very close to the blade leading edge stagnation point. Data from the Kulite #5 probe was utilized as an approximation to $P_{t,exit}$. As mentioned previously, no correction was made for the Kulite #5 bow shock pressure loss. Therefore, cascade pressure loss estimates based on Kulite #5 data would be generally higher than expected. However, since it was the unsteady loss **variation** that was most desired, these estimates were considered to be quite appropriate.

Figure 43 includes plots of pressure loss coefficient (as a percentage) versus Kulite #5 probe position. Three loss profiles are shown, corresponding to the steady-state curve (-0.03 msec), maximum positive variation (0.22 msec), and maximum negative variation (0.72 msec). Comparison with the wake plots of Fig. 42 shows that the maximum and minimum profiles for downstream pressure and loss coefficient occur at identical times. As indicated on Fig. 43, the pressure loss distribution across the passage certainly varies with time. Furthermore, variations in pressure loss coefficient of as much as 40 percent peak-peak appear between times 0.22 msec and 0.72 msec. It is also worth mentioning that the widest time-dependent variation in loss seems to occur near the center of the blade passage rather than in the wake regions. A more complete set of pressure loss coefficient curves is included in Appendix D. This appendix includes plots from time = –0.03 msec to 3.97 msec. Plots of later times are not included, as Kulite #1 data was not reduced beyond time = 4.25 msec. However, variation in loss beyond 3.97 msec is expected to parallel the variation in wake profiles as shown in Appendix C.

The pressure and loss data presented in Figures 35-43 have certainly confirmed the suspicions of strong unsteady shock-induced fluctuations on the transonic flowfield. These results are not intended to be viewed as extremely accurate representations of absolute lift and loss values. However, they do clearly indicate that, from an introductory perspective, unsteady shock wave interaction does have a significant impact on blade performance. Visual evidence of shock-induced blade passage unsteadiness has also been presented in Figures 31 and 32. It is hoped that these advances in the quantitative and qualitative understanding of unsteady shock effects has provided the impetus for more detailed investigations in the near future.

6.0 Conclusions and Recommendations

This project has successfully met the objectives set forth to provide capability for assessment of unsteady shock wave effects in the VPI Wind Tunnel Facility. A shock-generating system has been developed which is fully compatible with the existing transonic cascade test sections. Specialized optical systems and high-performance pressure instrumentation were developed and utilized to obtain qualitative and quantitative evidence of shock effects. Results indicate that significant variations in blade performance occur during the unsteady shock wave passage over the cascade. Specifically, a 120 percent peak-peak variation in estimated blade lift was found. Furthermore, an approximated loss coefficient was determined to fluctuate as much as 40 percent near the blade passage center. Visual evidence of unsteady shock effects was obtained in the form of shadowgraph photos. A previously unseen trailing edge shock wave distortion was also identified in the shadowgraphs.

Continuation of this project is strongly encouraged based on these introductory results. Possible extensions of this work could involve the analysis of shock-passing frequency on blade performance. Multiple shocks would be necessary for this study, and they could possibly be generated using multiple shotguns, branched passages in the shotgun system, or advanced rotating systems. Furthermore, an investigation of variable shock strength effects could be a valuable study for turbine design. In any case, it is strongly

encouraged that additional pressure instrumentation be utilized to better analyze the unsteady blade lift behavior. Future experiments should also concentrate on pre- and post-filtering of the data to ensure that signal noise is identified and reduced.

Experimental information such as that presented in this thesis will hopefully be of great benefit to the turbine blade designer. Previous industry assessment of turbine performance as based on steady-flow assumptions certainly does not represent important phenomena which actually exist during transonic operation. The growing movement toward unsteady, viscous numerical codes will certainly demand further experimental results to verify predictions. It is hoped that this study has served as a springboard for further, more detailed investigations of unsteady shock wave effects at Virginia Tech.

7.0 References

1. Doorly, D.J. and Oldfield, M.L.G., "Simulation of the Effects of Shock Wave Passing on a Turbine Rotor Blade," ASME J. Eng. for Gas Turbines and Power, Vol. 107, pp. 998-1006, 1985. (85-GT-112)

2. Ashworth, D.A., Lagraff, J.E., Schultz, D.L., and Grindrod, K.J., "Unsteady Aerodynamic and Heat Transfer Processes in a Transonic Turbine Stage," ASME J. Eng. for Power, Vol. 107, pp. 1022-1030, 1985.

3. Johnson, A.B., Rigby, M.J., Oldfield M.L.G., Ainsworth, R.W., and Oliver, M.J., "Surface Heat Transfer Fluctuations on a Turbine Rotor Blade Due to Upstream Shock Wave Passing," ASME J. Turbomachinery, Vol. 111, pp. 105-115, 1989. (88-GT-172)

4. Johnson, A.B., Rigby, M.J., and Olfield, M.L.G., "Unsteady Aerodynamic Phenomena in a Simulated Wake and Shock Wave Passing Experiment," AGARD-CP-468, 1989.

5. Johnson, A.B., Oldfield, M.L.G, Rigby, M.J., and Giles M.B., "Nozzle Guide Vane Shock Wave Propagation and Bifurcation in a Transonic Turbine Rotor," ASME Paper No. 90-GT-310.

6. Giles, M.B., "Stator/Rotor Interaction in a Transonic Turbine," AIAA J. Propulsion, Vol.6, No. 5, Sept.-Oct., pp. 621-627, 1990. (AIAA 88-3093)

7. Doorly, D.J., and Oldfield, M.L.G., "Simulation of Wake Passing in a Stationary Turbine Rotor Cascade," AIAA J. of Propulsion, Vol.1, No.4, pp. 316-318, 1985.

8. Doorly, D.J., "Modelling the Unsteady Flow in a Turbine Rotor Passage," ASME J. Eng. for Power, 1988. (87-GT-197)

9. Kemp, N.H., and Sears, W.R.,"Aerodynamic Interference Between Moving Blade Rows," J. Aero. Sci., Vol.20, No.9, Sept., pp. 585-597, 1953.

10. Parker, R., and Watson, J.F., "Interaction Effects Between Blade Rows in Turbomachines," Proc. I. Mech. Eng., Vol.186, No.21, 1972.

11. Mitchell, N.A., "A Time-Marching Method for Unsteady Two-Dimensional Flow in a Blade Passage," Int. J. Heat and Fluid Flow, Vol.2, No.4, 1980.

12. Dunn, M.G., "Turbine Heat Flux Measurements: Influence of Slot Injection on Vane Trailing Edge Heat Transfer and Influence of Rotor on Vane Heat

Transfer," ASME J. Eng. Gas Turbines and Power, Vol.107, No.1, pp. 76-83, 1985.

13. Dunn, M.G., George W.K., Rae, W.J., Woodward, S.H., Moller, J.C., and Seymour, P.J., "Heat-Flux Measurements for the Rotor of a Full-Stage Turbine: Part 2 – Description of Analysis Technique and Typical Time-Resolved Measurements," J. of Turbomachinery, Vol.108, July 1986.

14. Hodson, H.P., "Measurements of Wake-Generated Unsteadiness in Rotor Passages of Axial Flow Turbines," J. Eng. for Gas Turbines and Power, Vol.107, p.467, April 1985. (84-GT-189)

15. Joslyn, H.P., Dring R.P., and Sharma, O.P.,"Unsteady Three-Dimensional Turbine Aerodynamics," J. Eng. for Power, Vol. 105, p.322, April 1983. (82-GT-161)

16. Korakianitis, T.P., "On the Prediction of Unsteady Forces on Gas Turbine Blades, Part 1: Typical Results and Potential Flow Interaction Effects," ASME Paper 88-GT-89.

17. Nishiyama, T. and Sasaki, M., "Unsteady Forces Induced by Potential Interaction Between the Nozzle and Turbine Rotor Cascade Rows," Trans. Jpn. Soc. Mech. Eng., (in Japanese), Vol. 50, No.460, p.2888, 1984.

18. Hodson, H.P., "Measurements of Wake-Generated Unsteadiness in the Rotor Passages of Axial Flow Turbines," ASME J. of Eng. for Gas Turbines and Power, Vol.107, pp.467-476, April 1985. (84-GT-189)

19. Sharma, O.P., Pickett, G.F. and Ni, R.H., "Assessment of Unsteady Flows in Turbines," ASME Paper 90-GT-150.

20. Dullenkopf, K., Scultz, A. and Wittig, S., "The Effect of Incident Wake Conditions on the Mean Heat Transfer of an Airfoil," ASME Paper 90-GT-121.

21. Pfeil, H., Herbst, R., and Schroder, T., "Investigation of the Laminar-Turbulent Transition of Boundary Layers Disturbed by Wakes," ASME Paper 82-GT-124.

22. Liu, X., and Rodi, W., "Measurements of Unsteady Flow Over and Heat Transfer from a Flat Plate," ASME Paper 89-GT-2.

23. Paxson, D.E. and Mayle, R.E., "Laminar Boundary Layer Interaction with an Unsteady Passing Wake," ASME Paper 90-GT-120.

24. Kerrebrock, J.L. and Mikolajczak, A.A., "Intra-Stator Transport of Rotor Wakes and its Effect on Compressor Performance," ASME J. of Eng. for Power, pp.359-368, Oct., 1970.

25. Adachi, T. and Murakami, Y., "The Dimensional Velocity Distribution Between Stator Blades and Unsteady Force due to Passing Wakes," JSME, Vol.22, No.170, pp.1074-1082, Aug., 1979.

26. Weyer, H. and Dunker, R., "Flow Measurements in Stator Rows Behind a Transonic Axial Compressor," AGARD-CP-351, Copenhagen, June 1983.

27. Rigby, M.J., Johnson, A.B., and Oldfield, M.L.G., "Gas Turbine Rotor Blade Film Cooling With and Without Simulated NGV Shock Waves and Wakes," ASME Paper 90-GT-78.

28. Jones, T.V., Schultz, D.L., Oldfield, M.L.G., and Daniels, L.C., "A New Transient Facility for the Measurement of Heat Transfer Rates,"*High Temperature Problems in Gas Turbine Engines*, AGARD-CP-229, pp.31-1 to 31-27, 1979.

29. Schultz, D.L., Jones T.V., Oldfield, M.L.G., and Daniels, L.C., "Measurement of the Heat Transfer Rate to Turbine Blades and N.G.V.'s in a Transient Cascade," Paper EC-12 presented at 6th International Heat Transfer Conference, Toronto, Canada, 1978.

30. Doorly, D.J., "The Effects of Wake-Passing on Turbine Blades," Ph.D. Thesis, Oxford University, Oxford, England, 1983.

31. Bertsch, R., "An Experimental Examination of the Influence of Trailing Edge Injection on Blade Losses in Transonic Turbine Cascades," VPI Thesis, 1990.

32. Doughty, R.L., "The Effect of Blade Solidity on the Aerodynamic Loss of a Transonic Turbine Cascade," VPI Thesis, 1991.

33. Collie, J.C., Moses, H.L., and Kiss, T., "The Effect of Blunt Trailing Edge on Turbine Blade Performance," AIAA Paper No. 91-2130.

34. Moses, H.L., Kiss, T., Bertsch, R., and Gregory, B.A., "Aerodynamic Losses Due to Pressure Side Coolant Ejection in a Transonic Turbine Cascade," AIAA Paper No. 91-2032.

35. Moses, H.L., Schetz, J.A., and Gregory, B.A., "Cooled, Transonic Turbine Cascade Testing," to be published in the Proceedings of the ISABE Conference, Nottingham, England, September, 1991.

36. Doughty, R.L., Moses, H.L., and Gregory, B.A., "The Effect of Blade Solidity on the Aerodynamic Loss of a Transonic Turbine Cascade," AIAA Paper No. 92-0393, to be presented at the 30th Aerospace Sciences Meeting, Reno, NV, Jan. 6-9, 1992.

37. Priddy, W.J., and Bayley, F.J., "Effects of Free Stream Turbulence on the Distribution of Heat Transfer Around Turbine Blade Sections," Int. J. Heat and Fluid Flow, Vol.6, No.3, pp.181-191, Sept., 1985.

38. Priddy, W.J., and Bayley, F.J., "Turbulence Measurements in Turbine Blade Passages and Implications for Heat Transfer," ASME Paper No. 87-GT-195.

39. Merritt, D.L. and Aronson, P.M., "Wind Tunnel Simulation of Head-On Bow Wave — Blast Wave Interactions," Report No. 67-123, United States Naval Ordnance Laboratory, White Oak, Maryland, August 9, 1967.

40. Zucker, R.D., Fundamentals of Gas Dynamics, Champaign, IL, Matrix Publishers, pp.393-401, 1977.

8.0 Figures

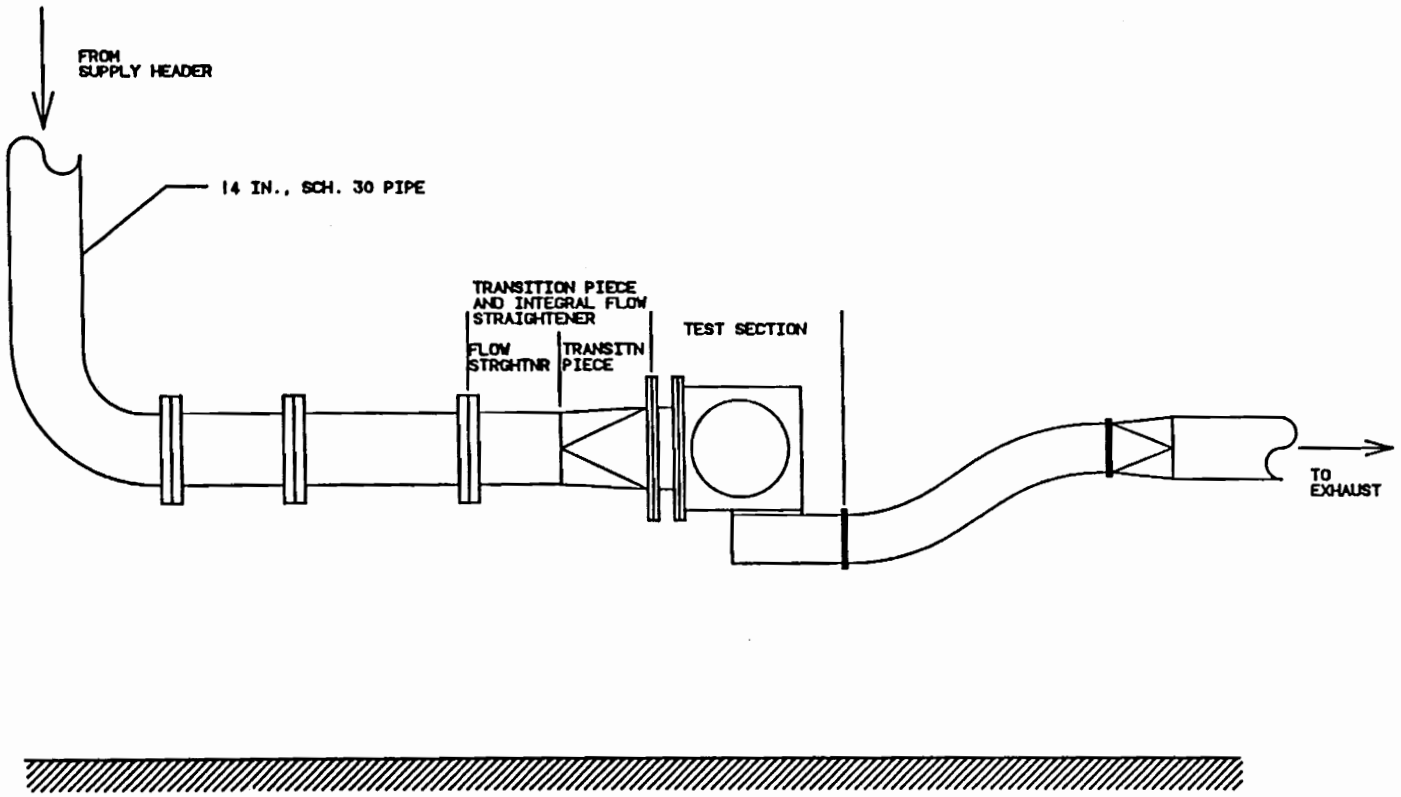

Figure 1: Schematic: VPI & SU transonic cascade wind tunnel.

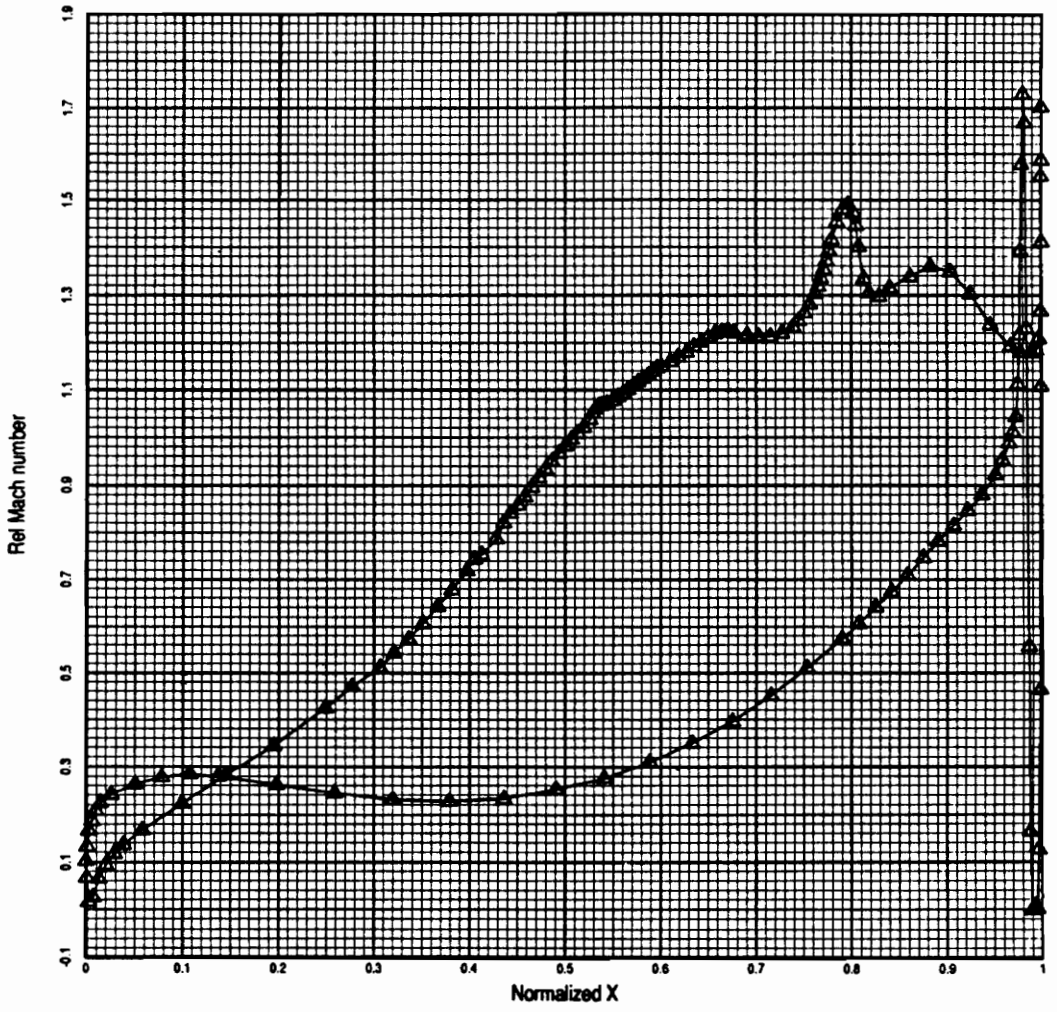

Figure 2: Numerically-predicted blade surface Mach number vs normalized axial distance.

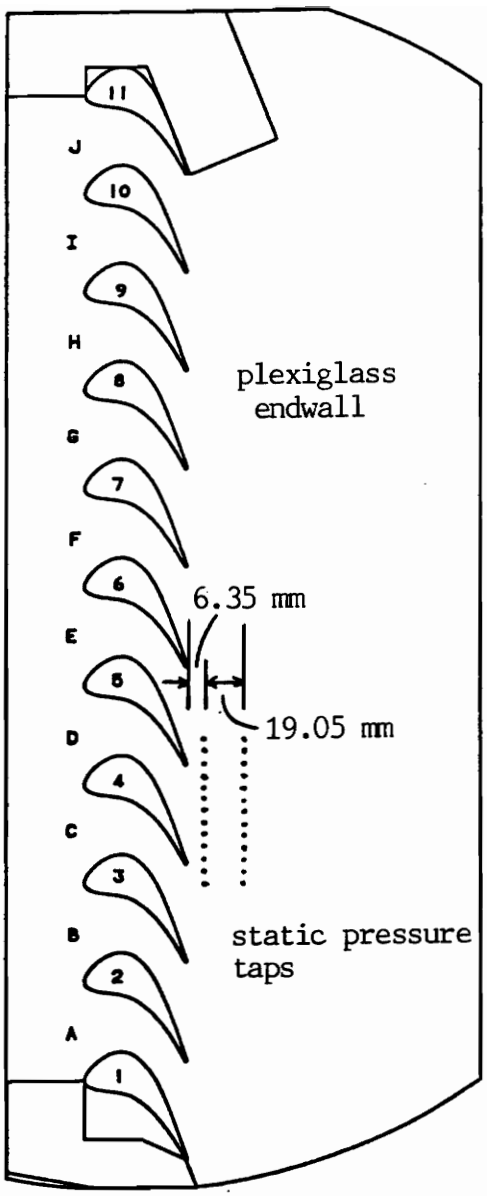

Figure 3: Schematic: cascade test section.

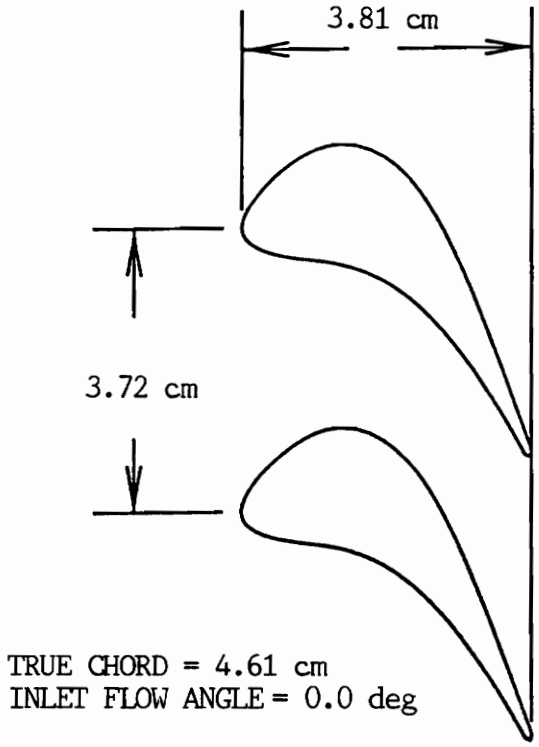

Figure 4: Schematic: blade geometry.

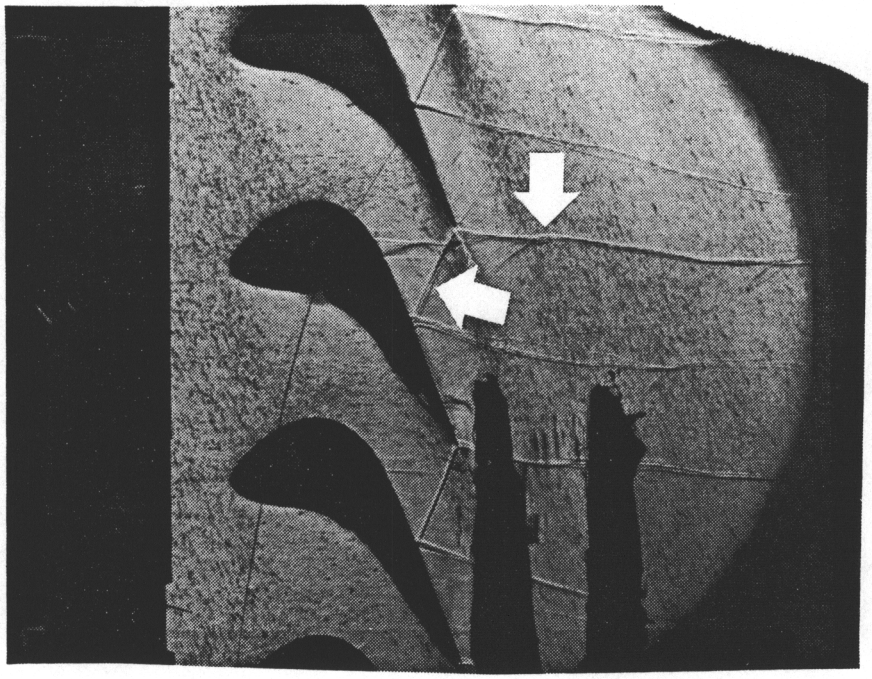

Figure 5: Shadowgraph: cascade under steady-flow conditions at M=1.16. Arrows indicate trailing edge shocks.

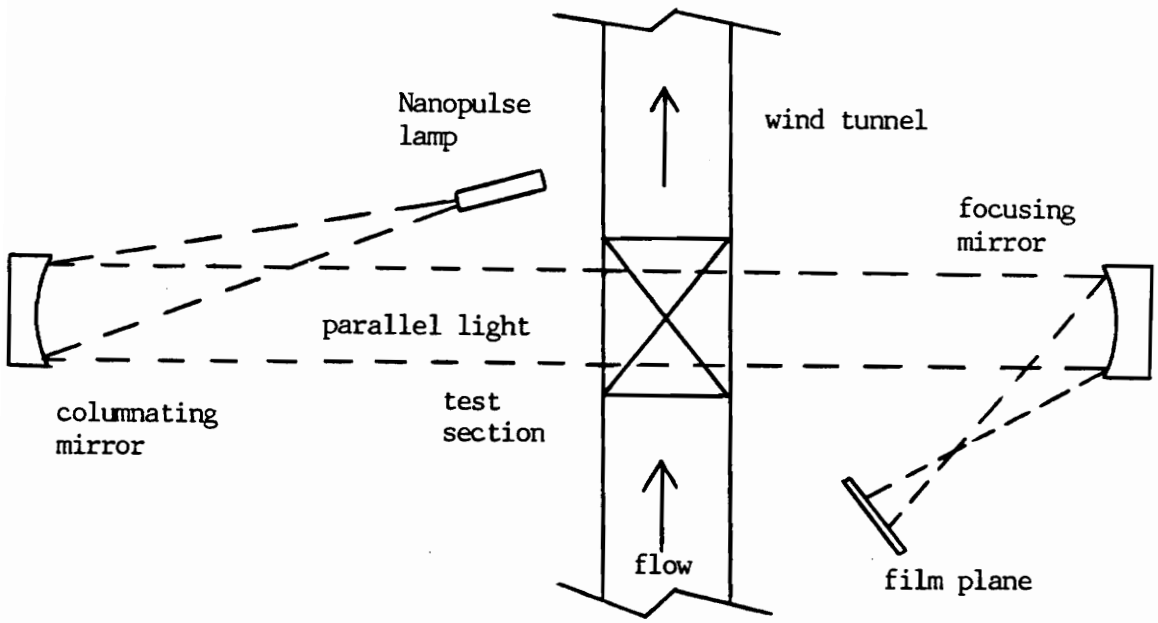

Figure 6: Schematic: still-shadowgraph system.

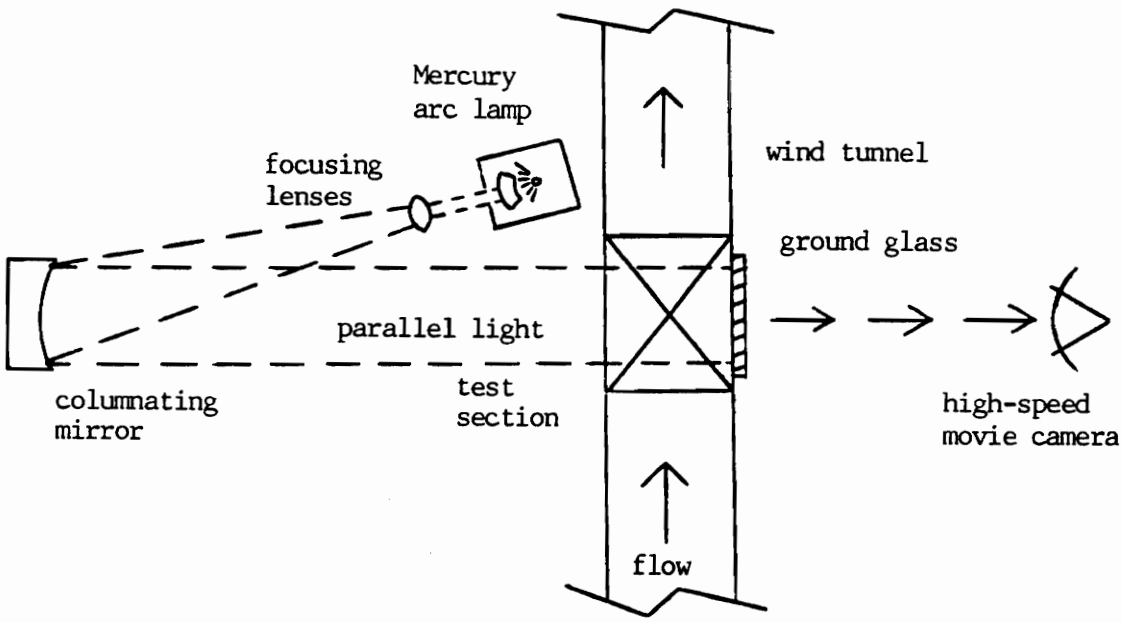

Figure 7: Schematic: shadowgraph movie system.

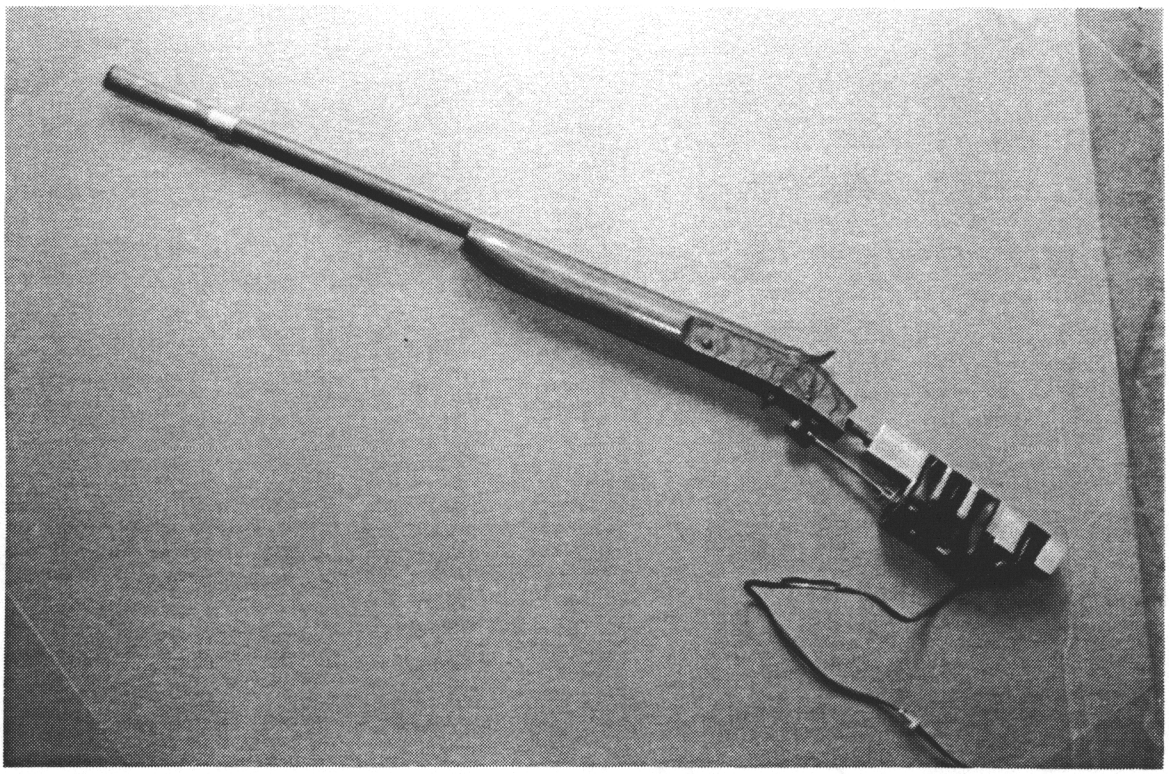

Figure 8: Shotgun as used for shock wave generation.

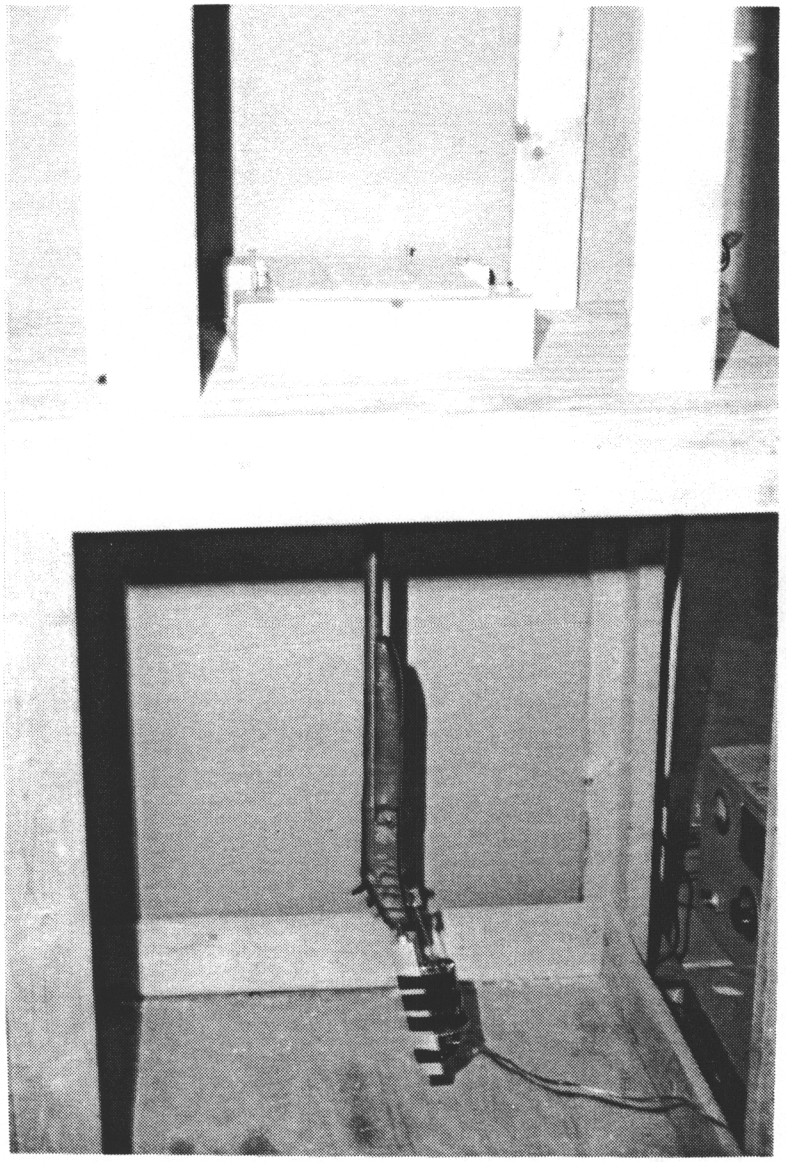

Figure 9: Experimental test-stand in original configuration.

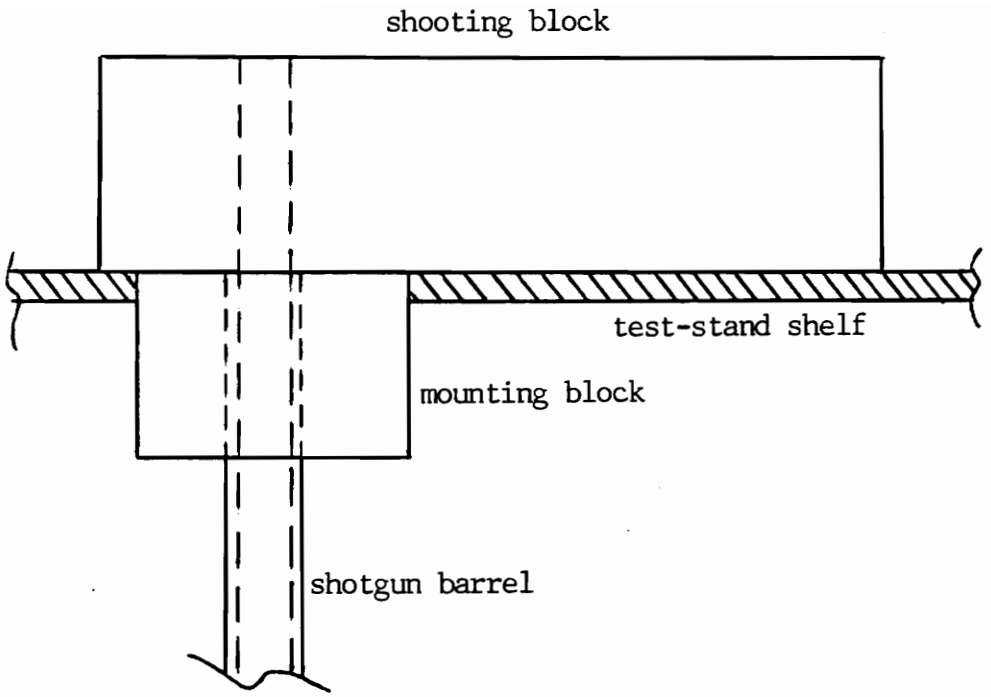

Figure 10: Schematic: shooting and mounting blocks in original configuration.

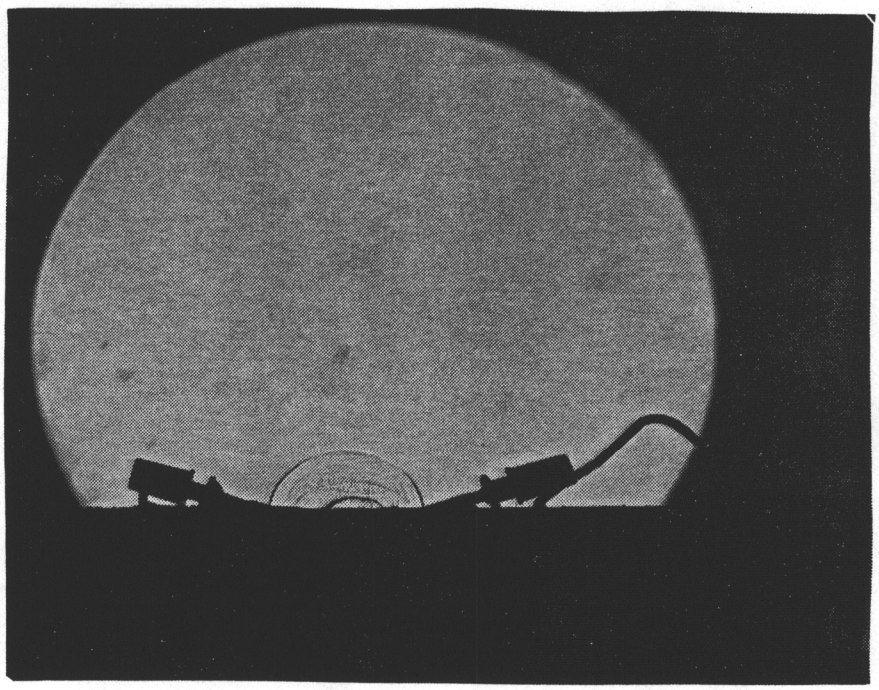

Figure 11a: Shadowgraph: shock wave propagation from circular shooting block hole — frame 1.

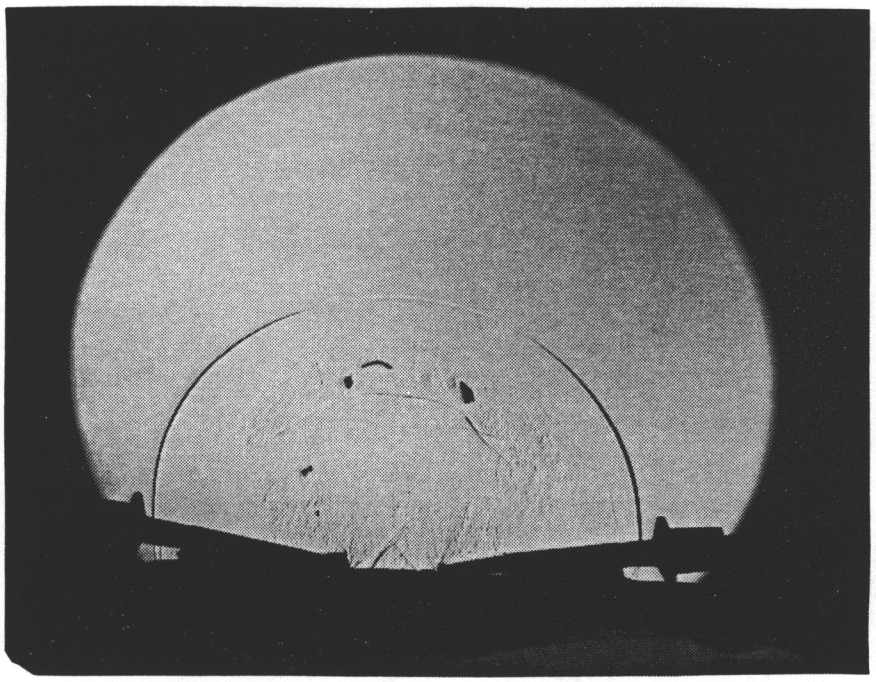

Figure 11b: Shadowgraph: shock wave propagation from circular shooting block hole — frame 2.

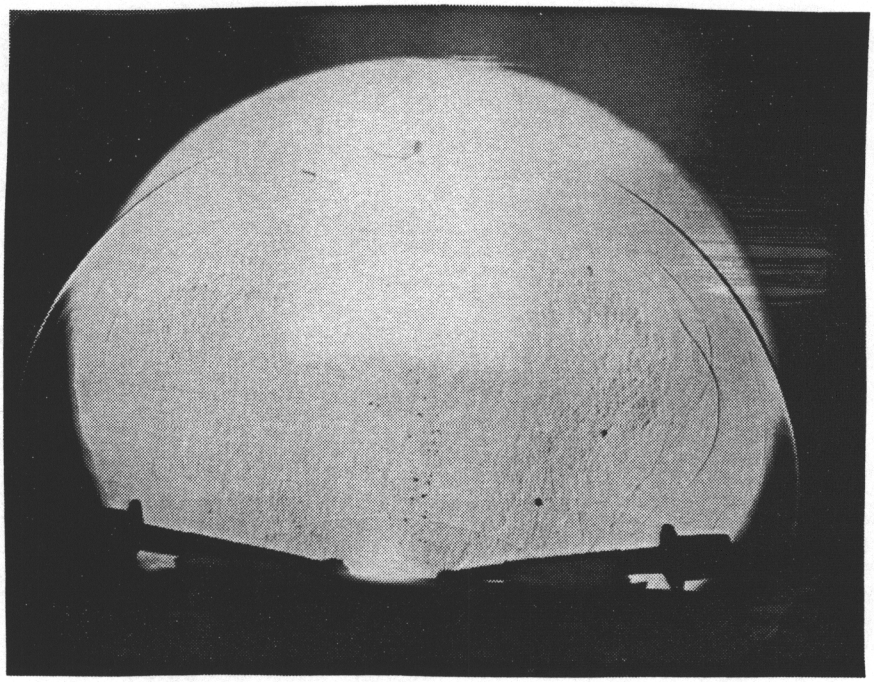

Figure 11c: Shadowgraph: shock wave propagation from circular shooting block hole — frame 3.

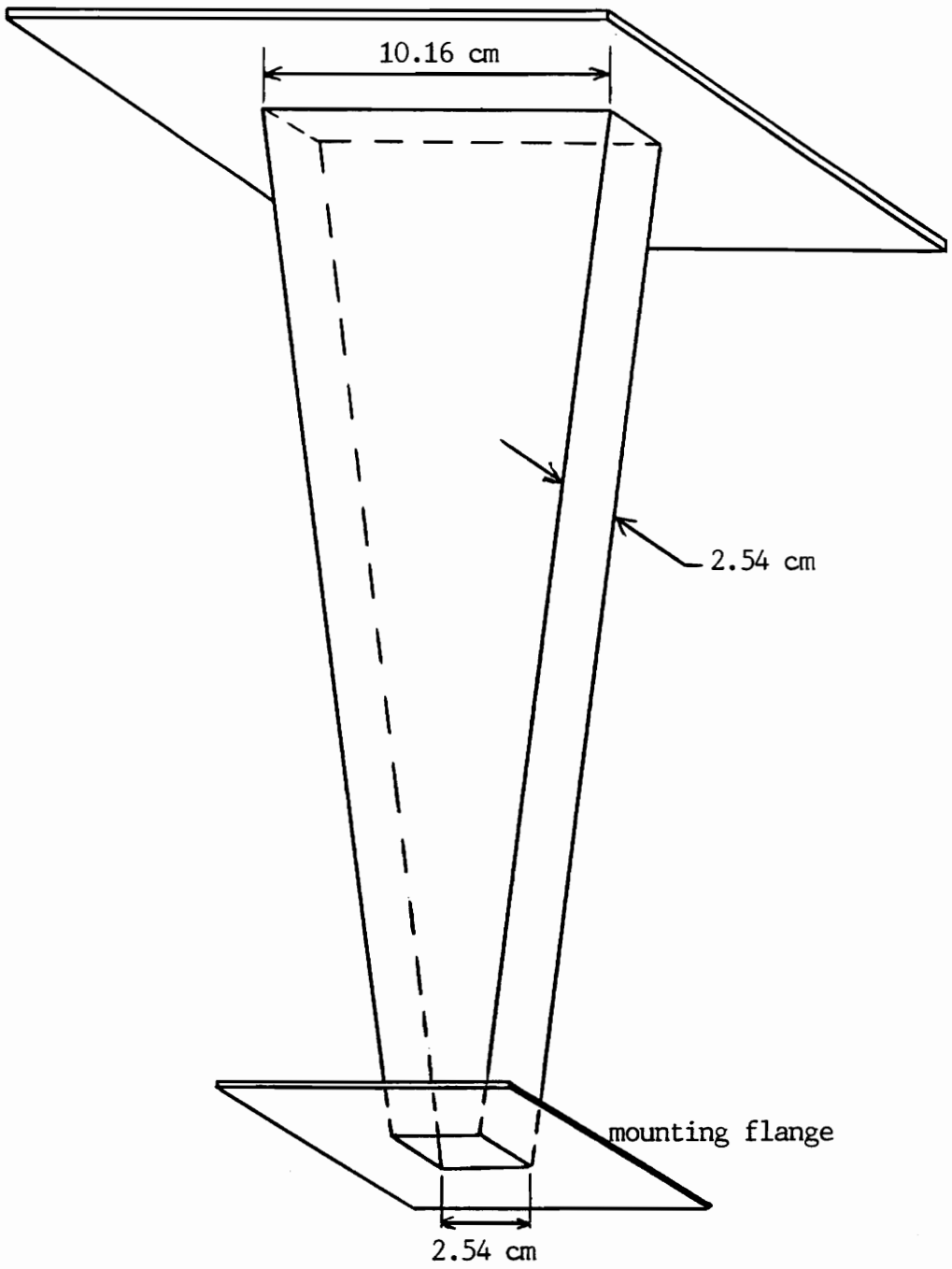

Figure 12: Schematic: shock-shaper.

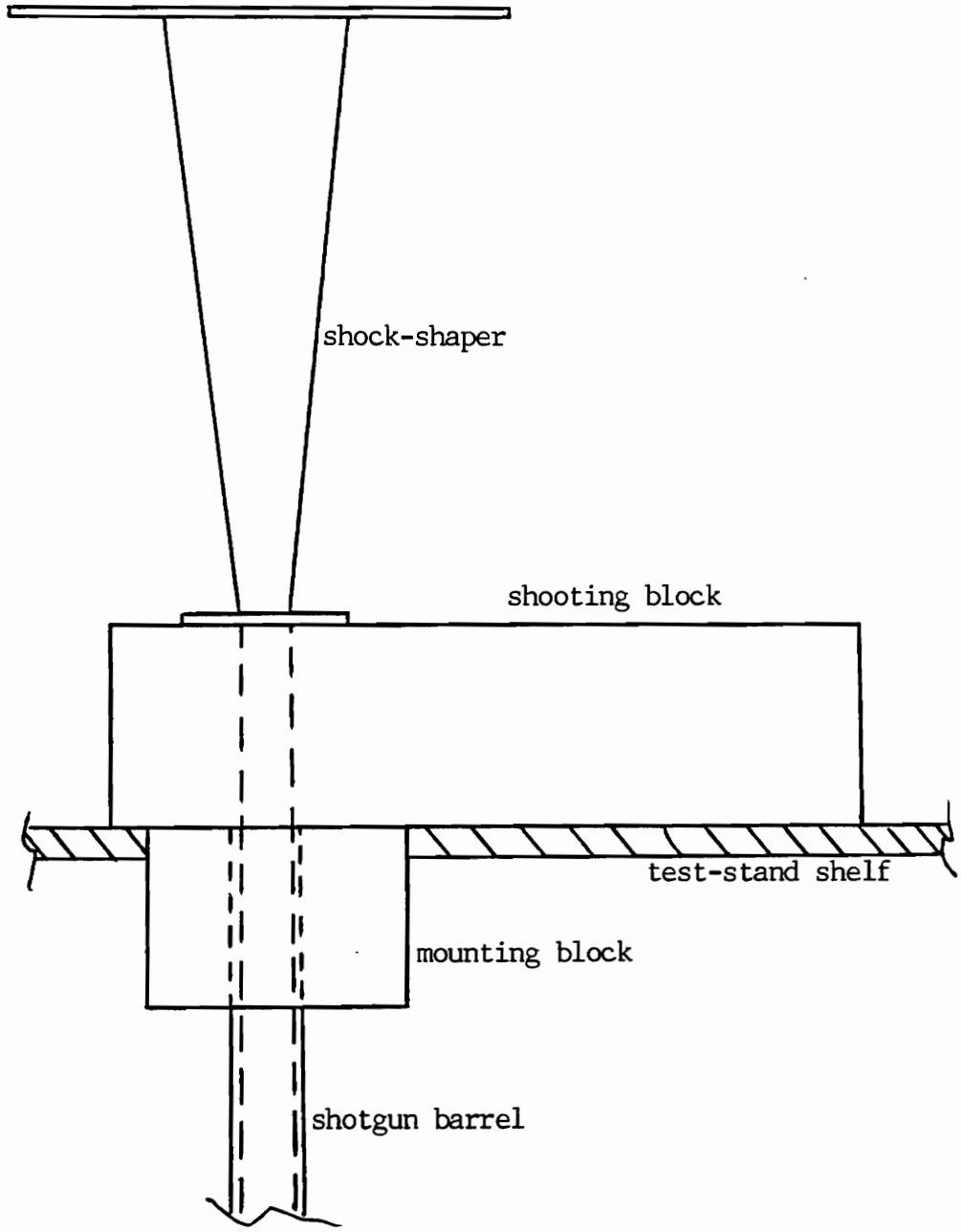

Figure 13: Schematic: shock-shaper mounting on test stand.

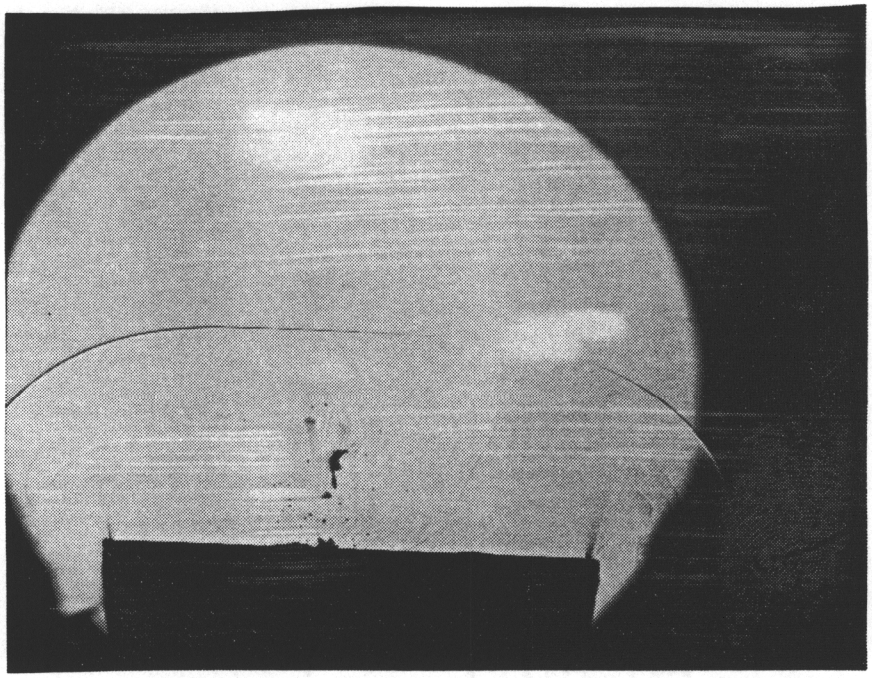

Figure 14a: Shadowgraph: shock wave propagation from shock-shaper — frame 1.

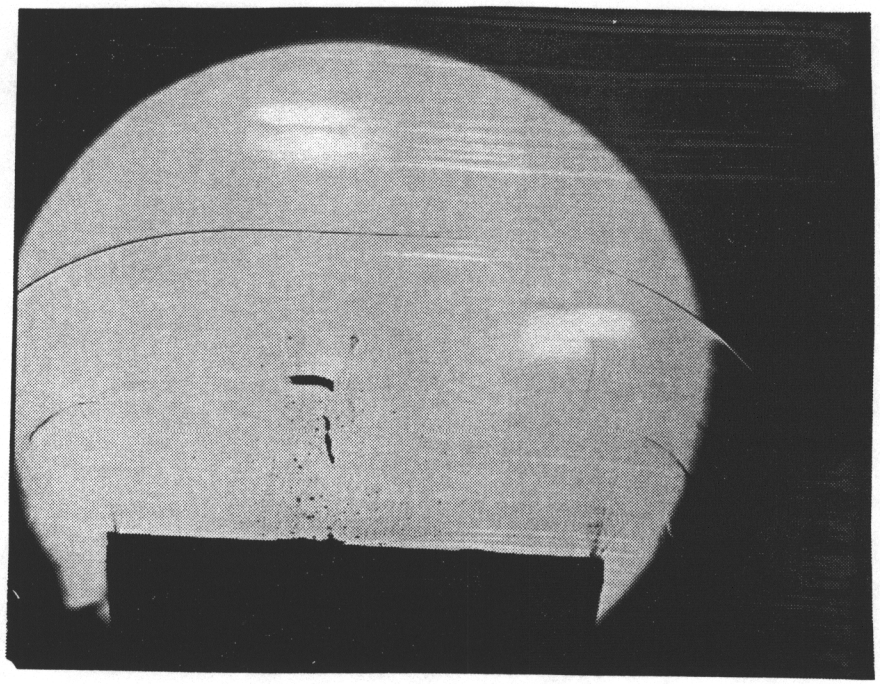

Figure 14b: Shadowgraph: shock wave propagation from shock-shaper — frame 2.

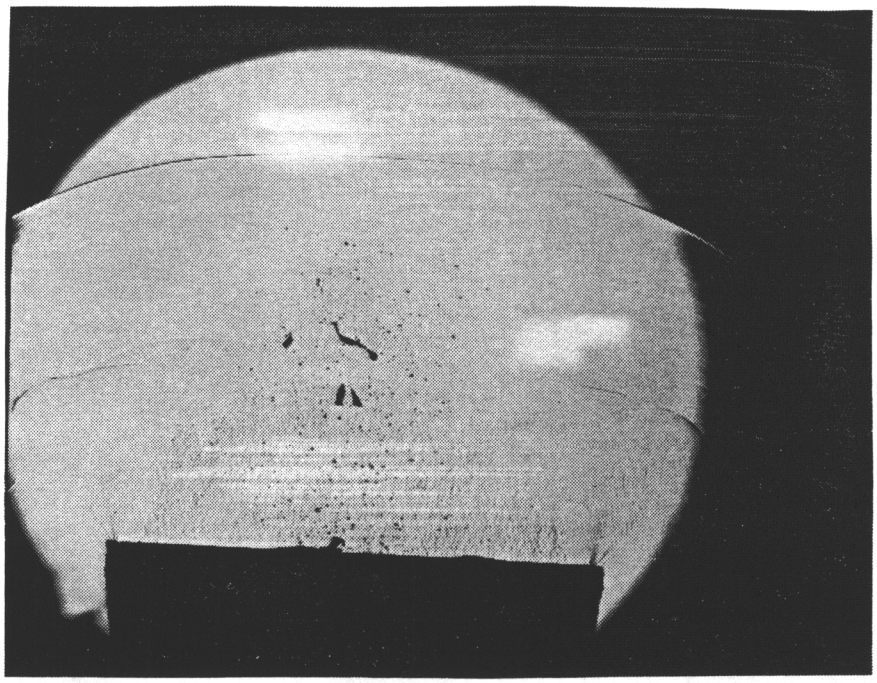

Figure 14c: Shadowgraph: shock wave propagation from shock-shaper — frame 3.

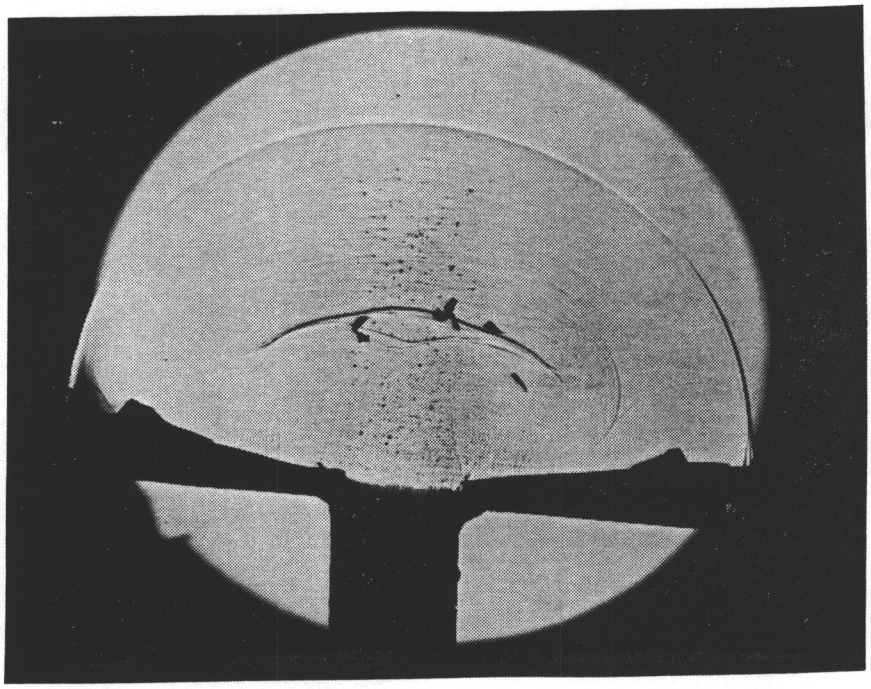

Figure 15a: Shadowgraph: Popper-Load shock wave showing repeatability — run #1 of 5.

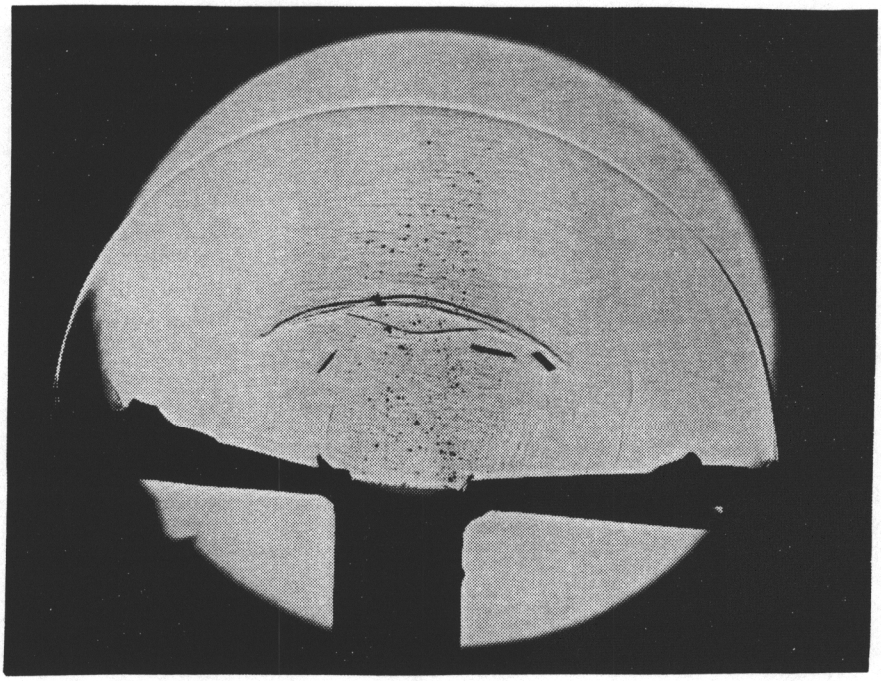

Figure 15b: Shadowgraph: Popper-Load shock wave showing repeatability — run #2 of 5.

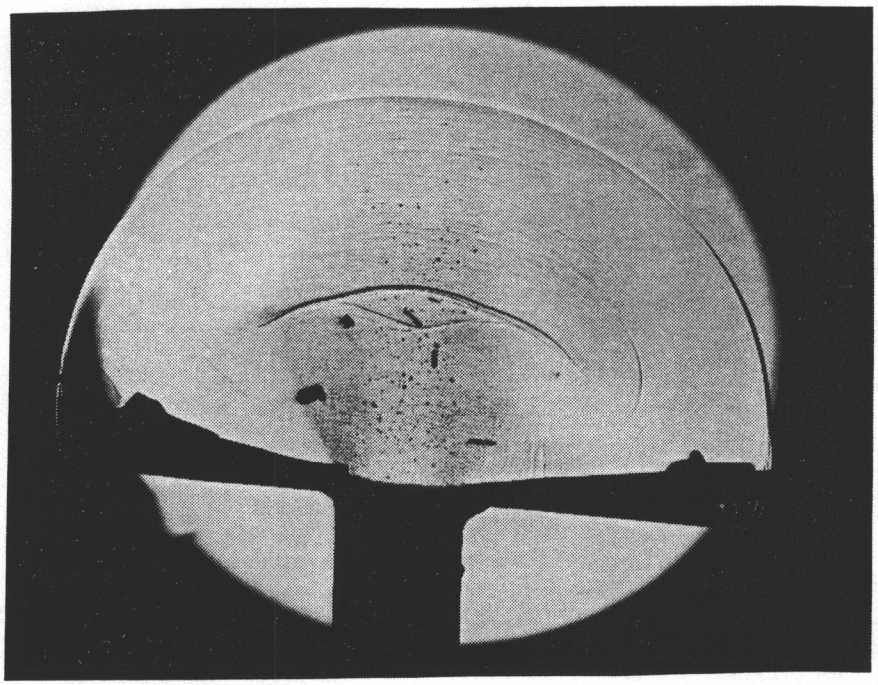

Figure 15c: Shadowgraph: Popper-Load shock wave showing repeatability — run #3 of 5.

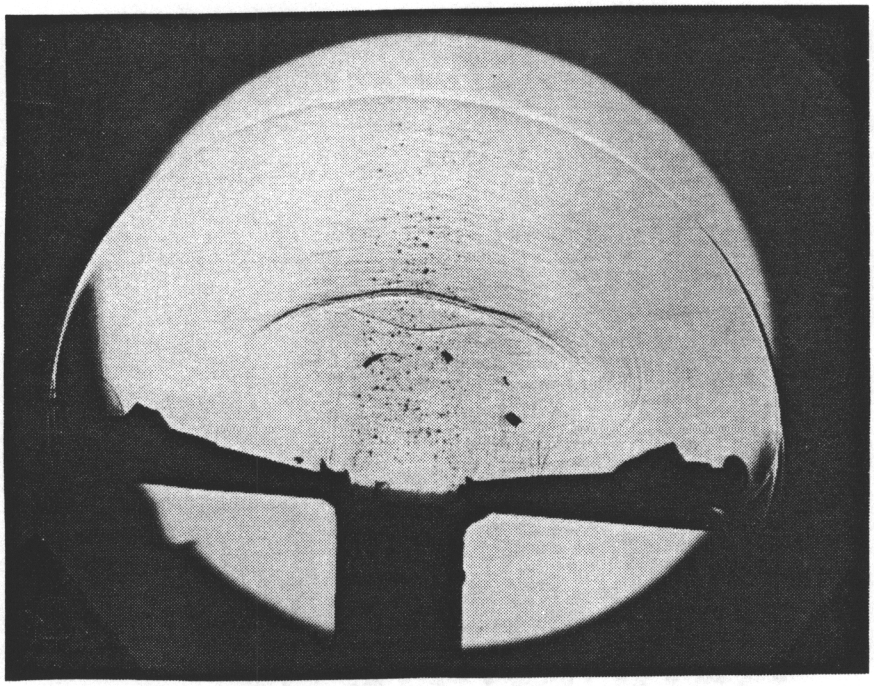

Figure 15d: Shadowgraph: Popper-Load shock wave showing repeatability — run #4 of 5.

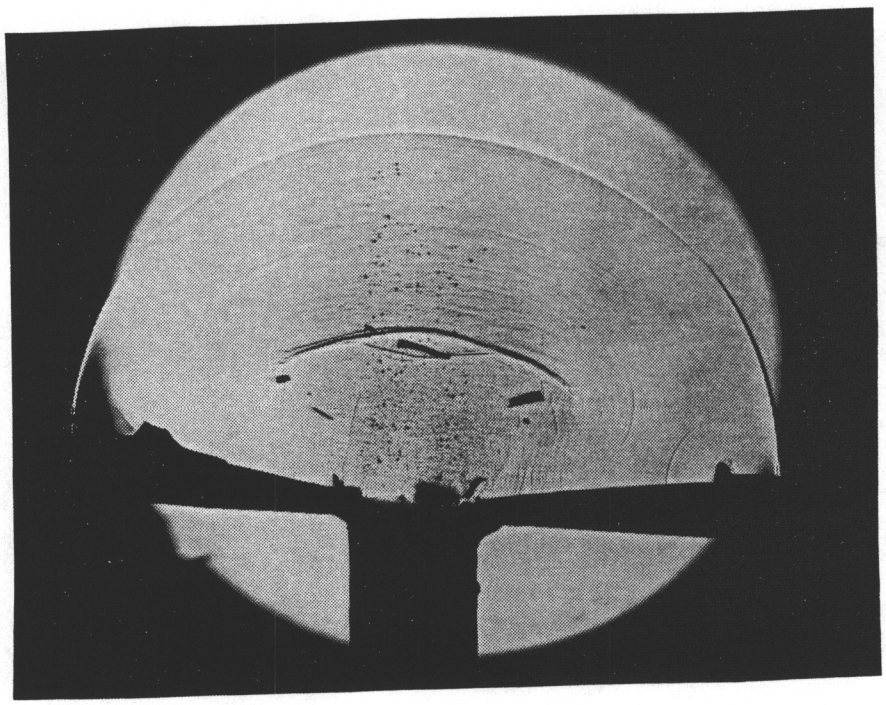

Figure 15e: Shadowgraph: Popper-Load shock wave showing repeatability — run #5 of 5.

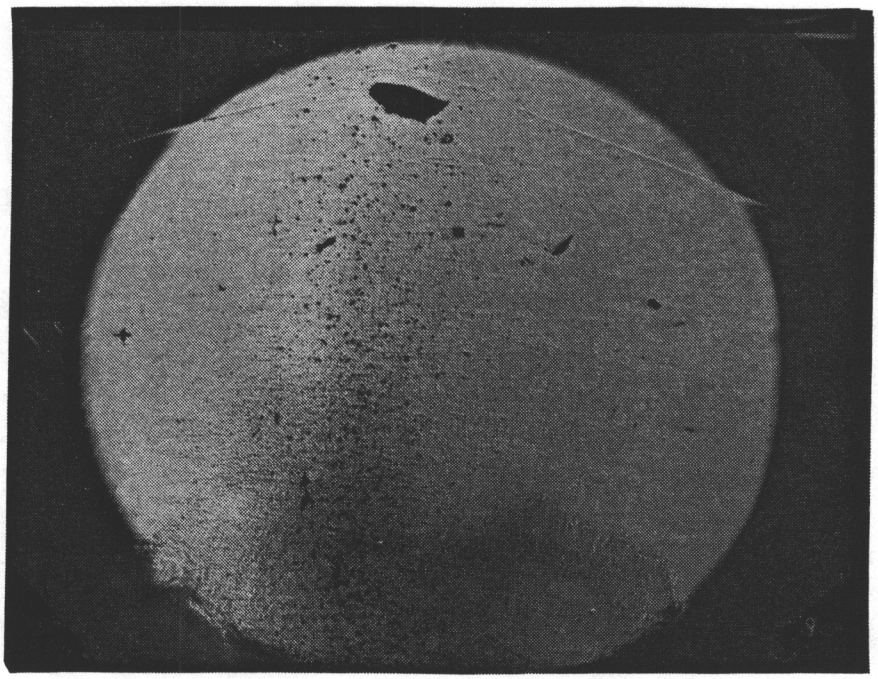

Figure 16: Shadowgraph: shock wave distortion caused by shell packing residue.

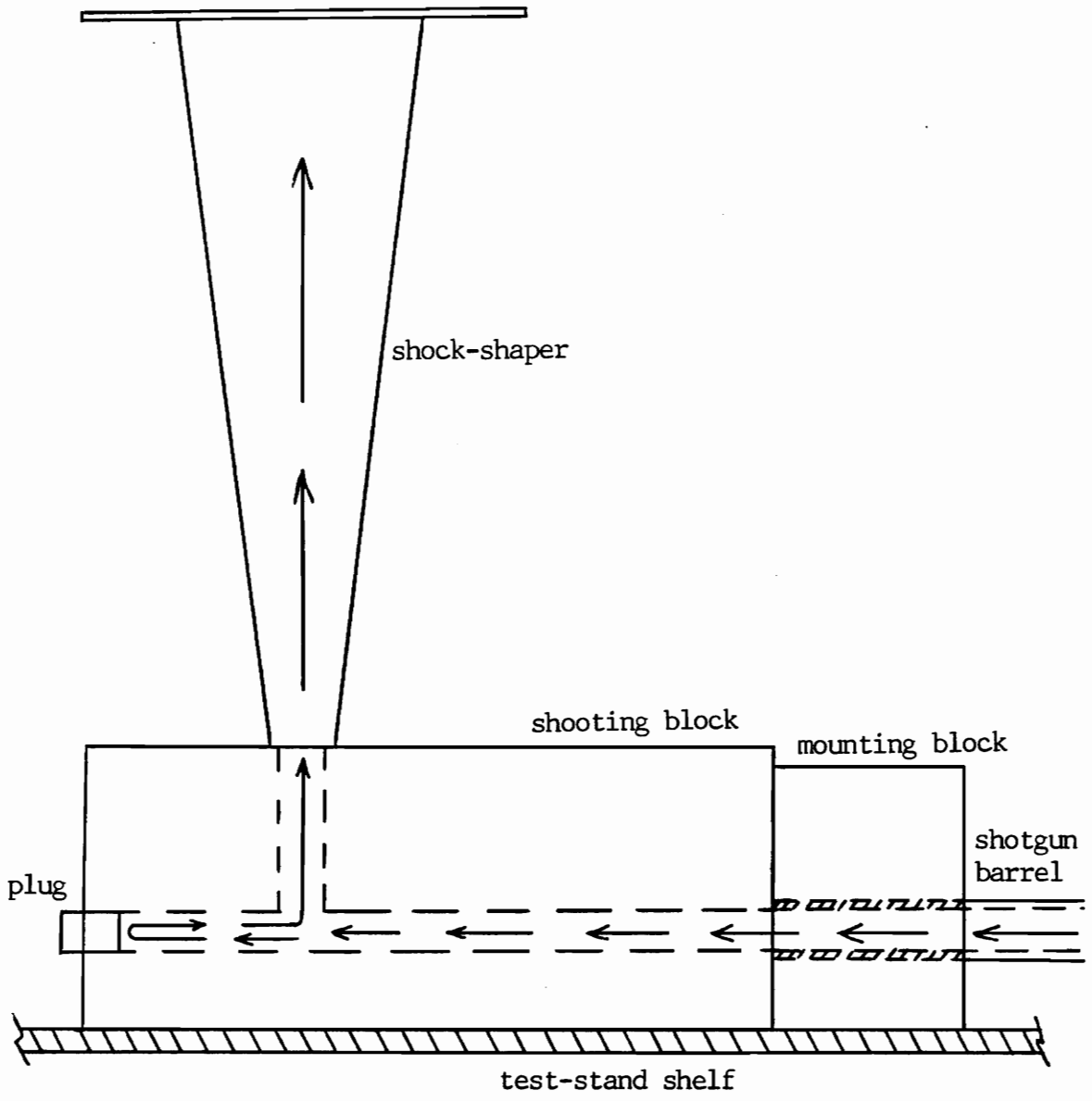

Figure 17: Schematic: improved shooting block showing direction of shock propagation.

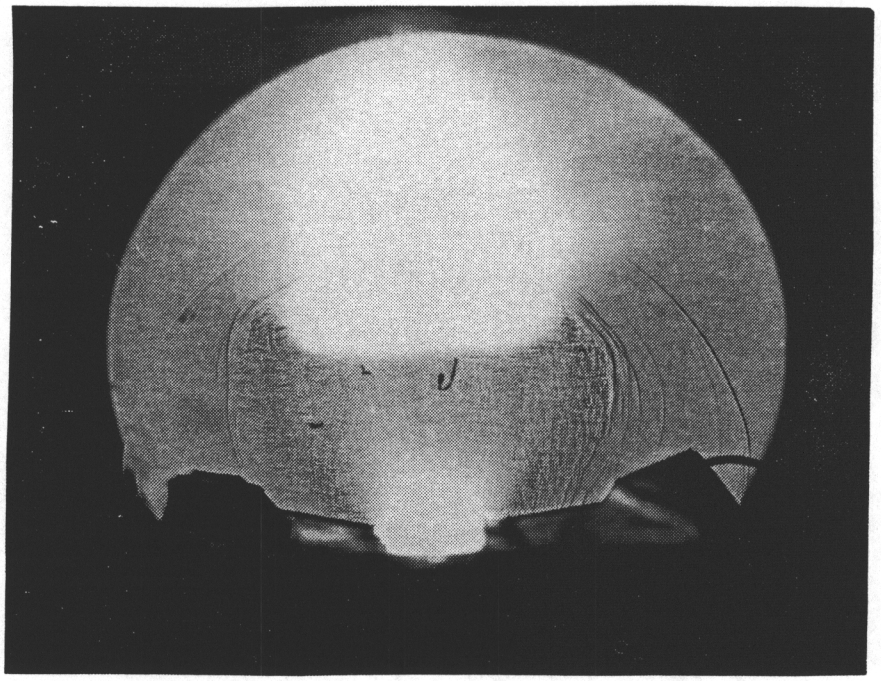

Figure 18: Shadowgraph: shock wave exiting from improved shooting block (no filter).

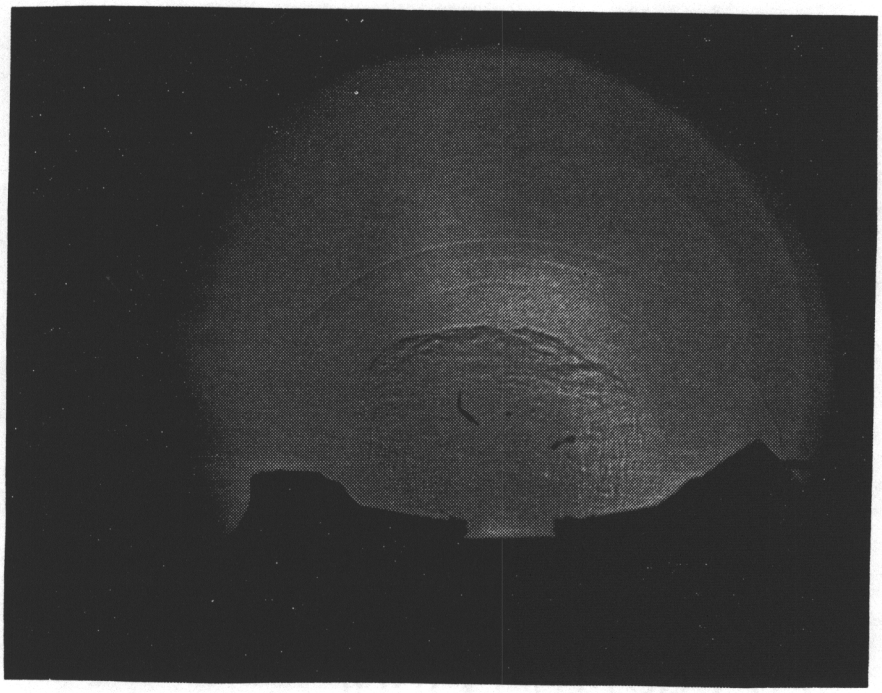

Figure 19: Shadowgraph: shock wave exiting from improved shooting block (with filter).

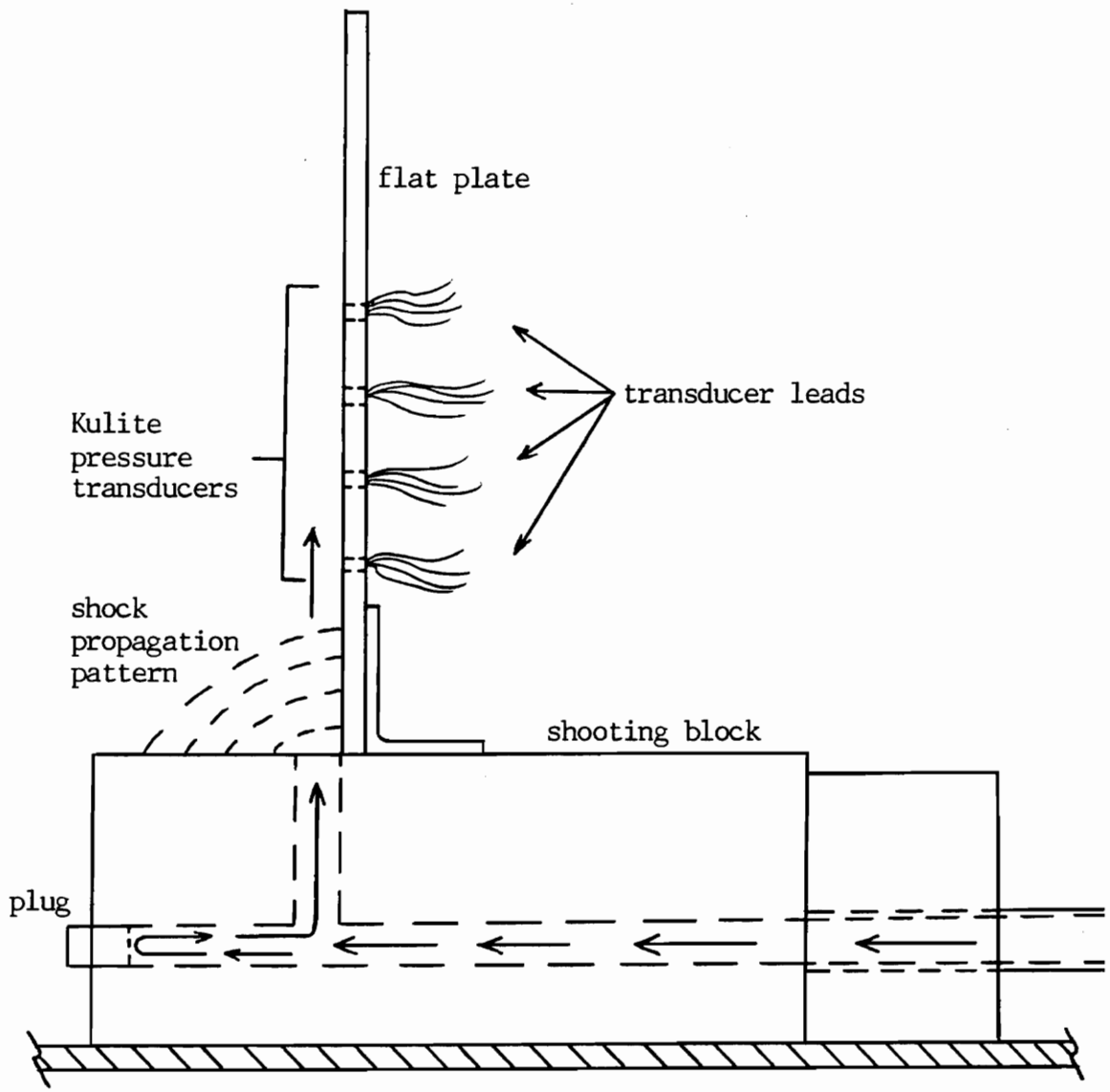

Figure 20: Schematic: flat plate velocity measurement apparatus.

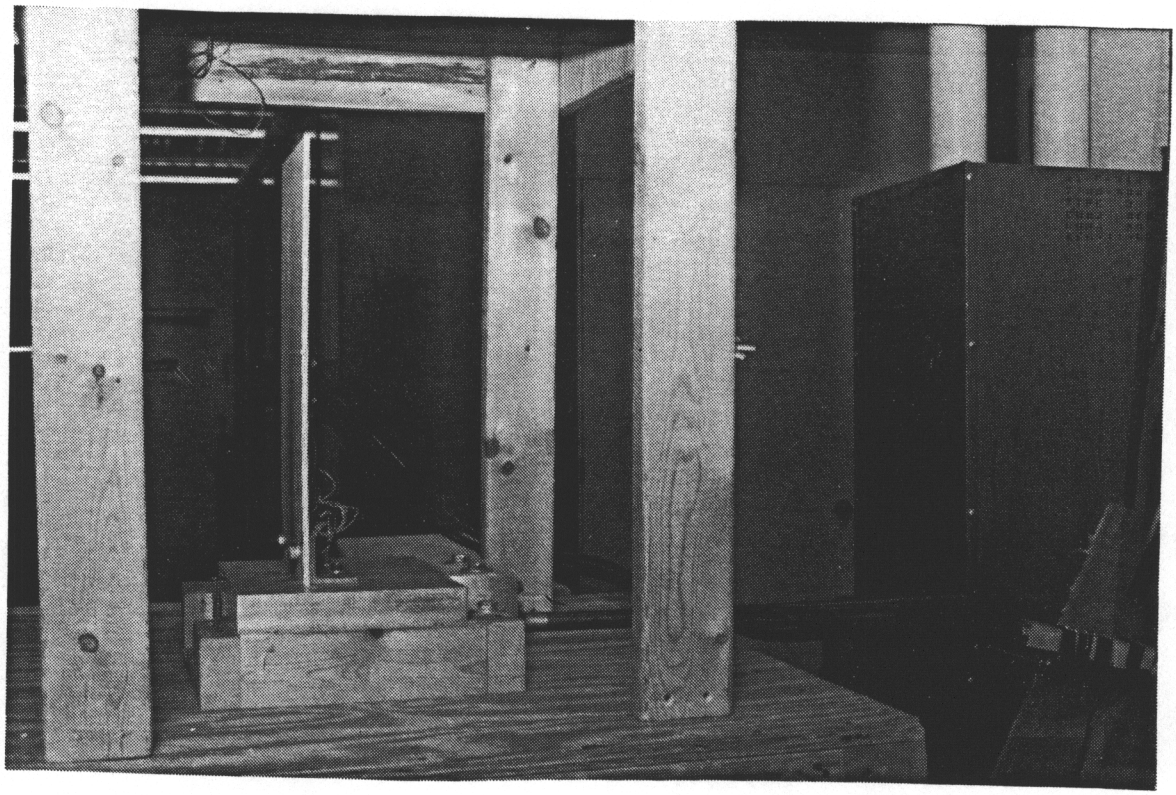

Figure 21: Shock velocity measurement apparatus.

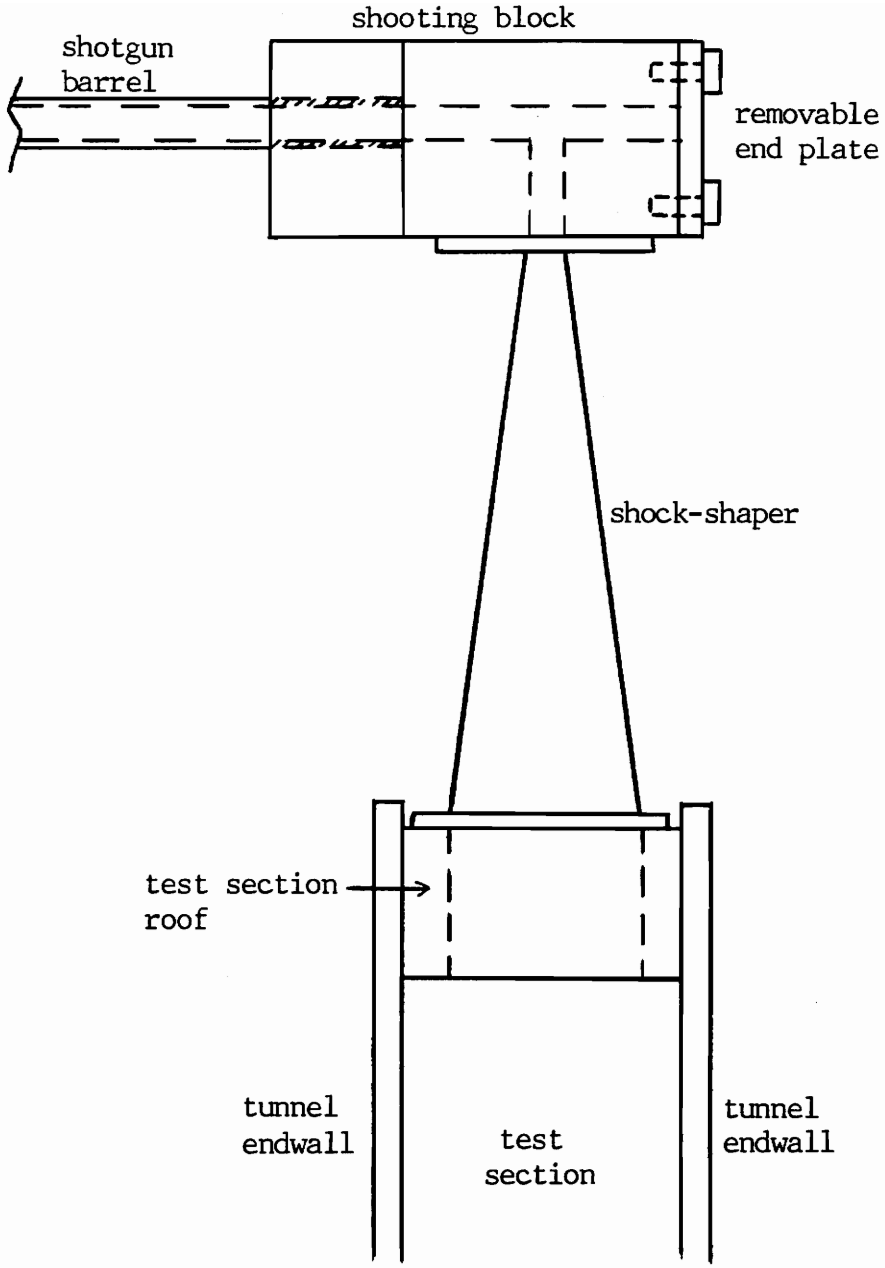

Figure 22: Schematic: tunnel-mounted shock generation system as viewed along flow direction.

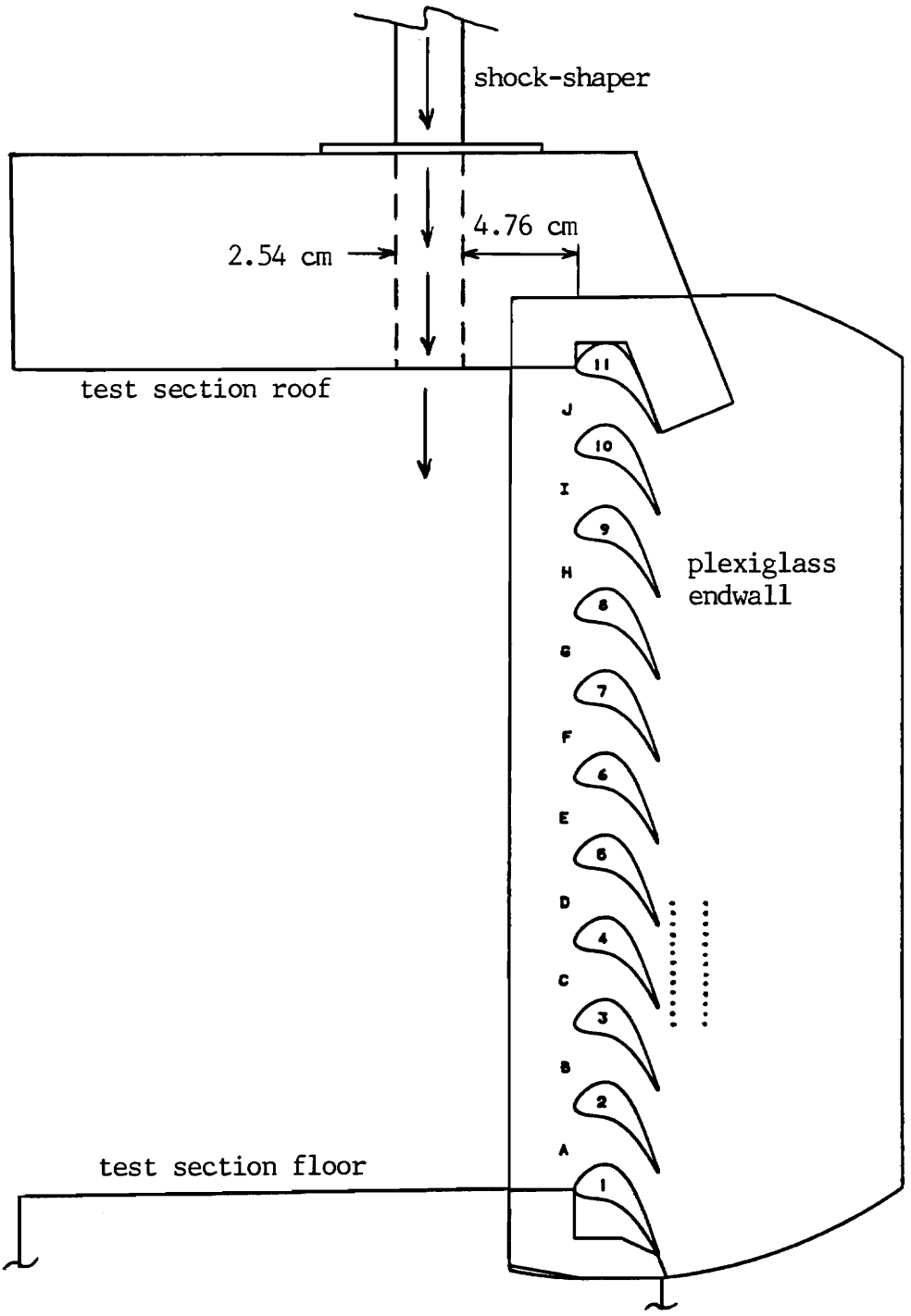

Figure 23: Schematic: tunnel-mounted shock generation system as viewed normal to flow direction.

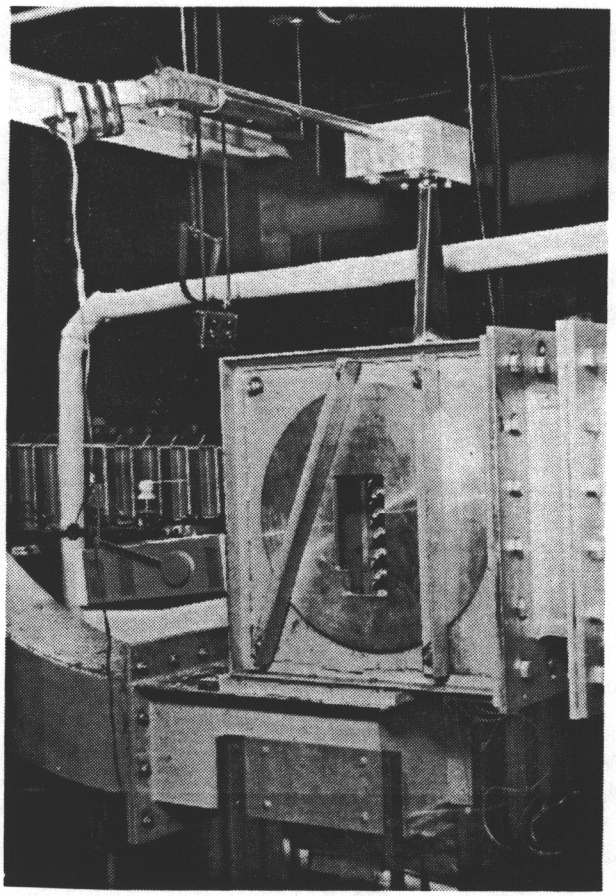

Figure 24: Tunnel-mounted shock generation system.

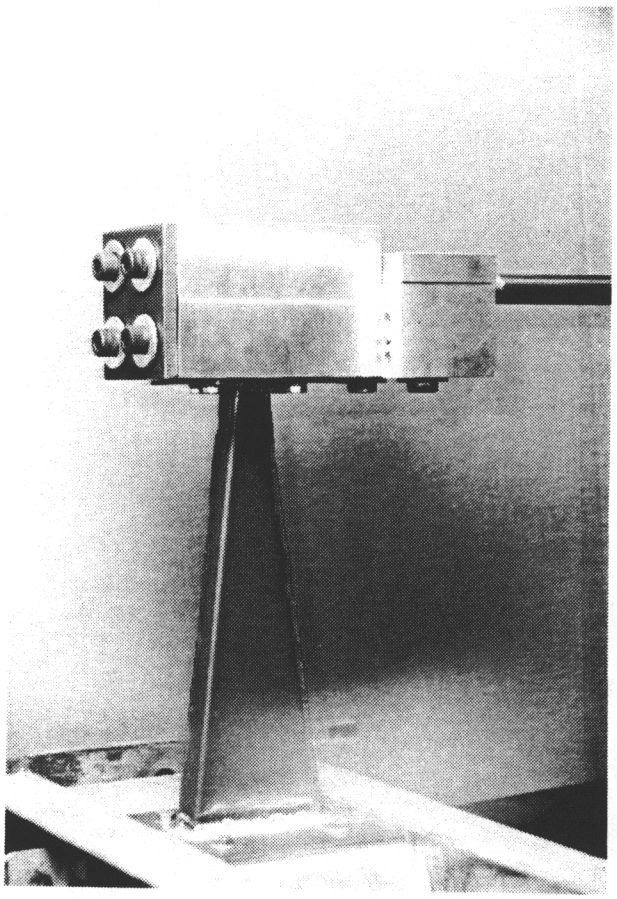

Figure 25: Close-up view of tunnel-mounted shooting block and shock-shaper.

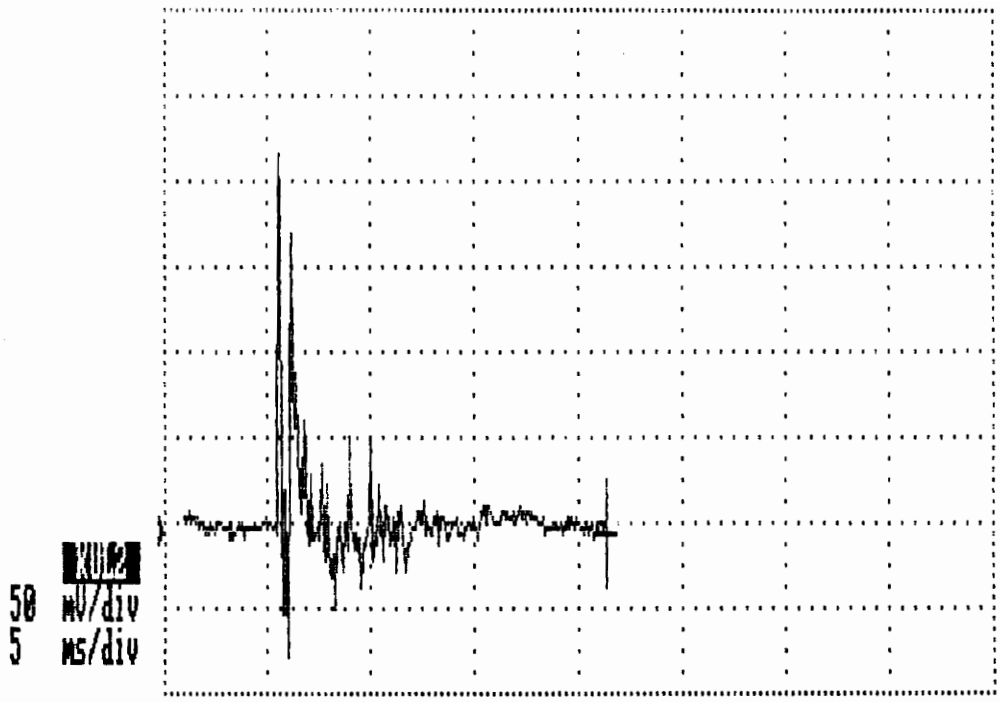

Figure 26: Sample unsteady pressure trace from experimental test rig indicating general shock-induced behavior.

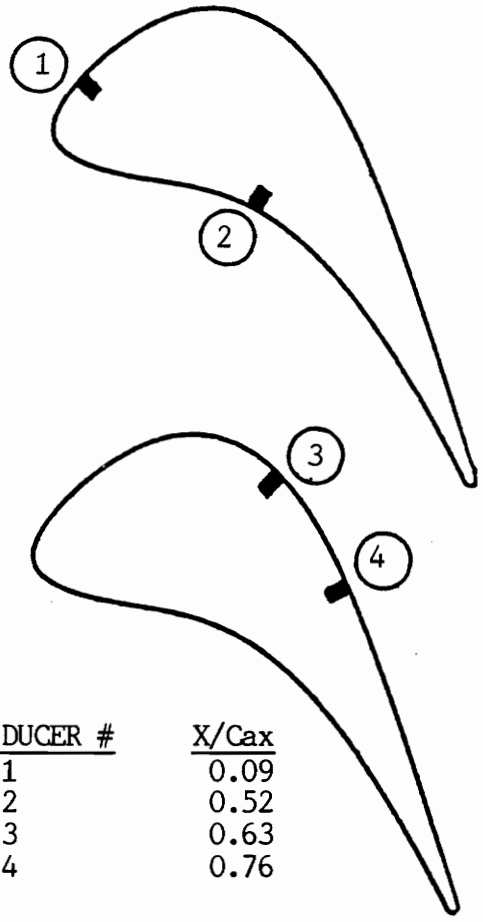

TRANSDUCER #	X/Cax
1	0.09
2	0.52
3	0.63
4	0.76

Figure 27: Schematic: pressure transducer locations.

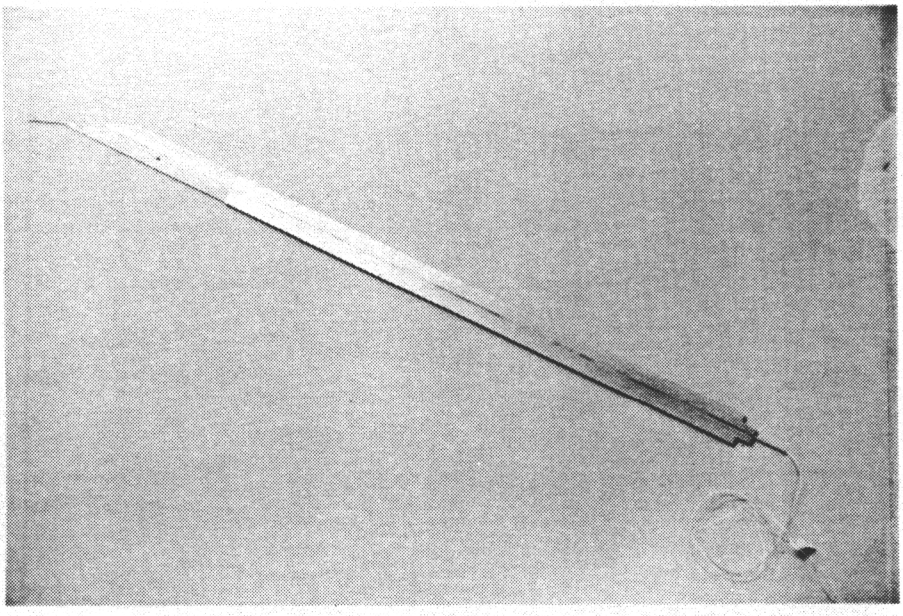

Figure 28: Total pressure probe containing Kulite #5.

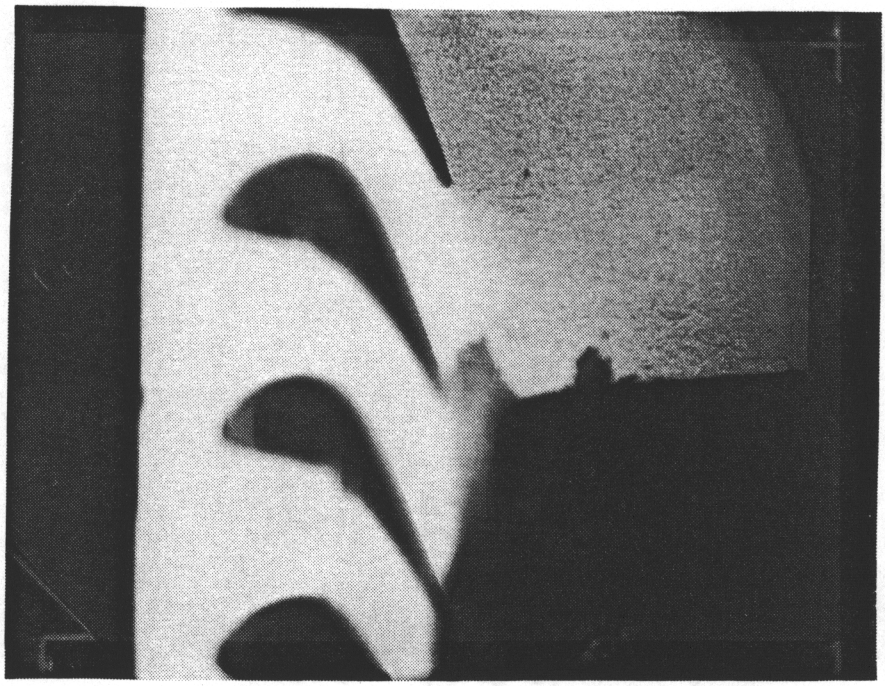

Figure 29: Shadowgraph: cascade test section with no flow, no shock generation, and no filter.

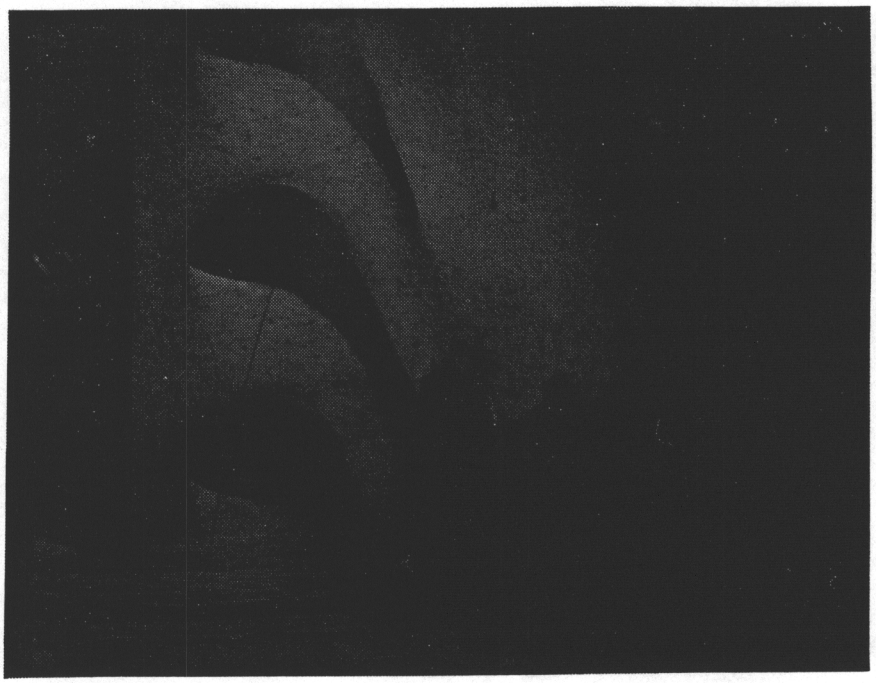

Figure 30: Shadowgraph: repeat of Figure 29 using optical filter to eliminate flash.

Figure 31a: Shadowgraph: cascade under steady tunnel flow — no shock generation.

Figure 31b: Shadowgraph: cascade unsteady shock passage — time = 0.052 msec.

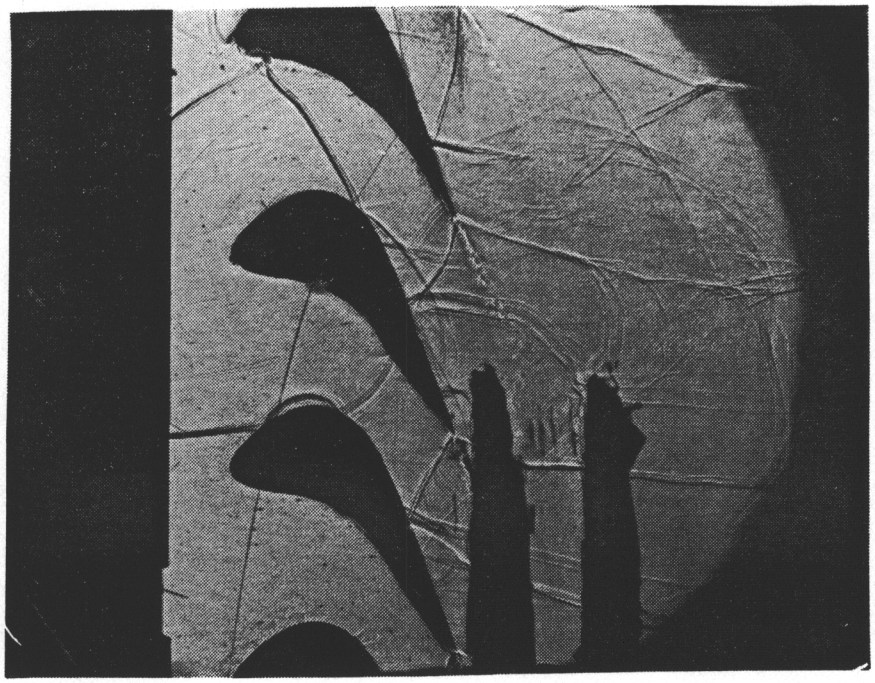

Figure 31c: Shadowgraph: cascade unsteady shock passage — time = 0.055 msec.

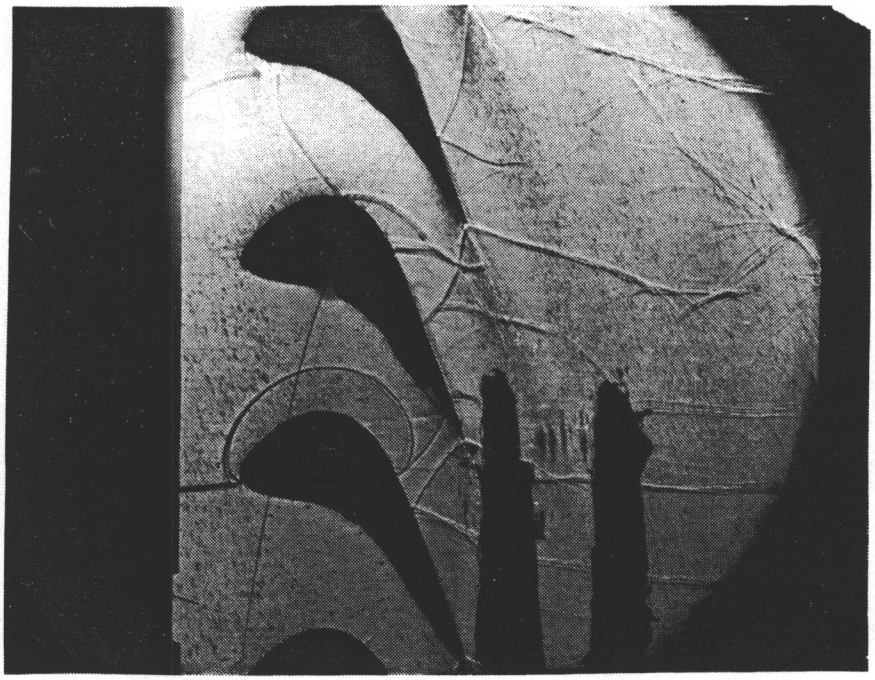

Figure 31d: Shadowgraph: cascade unsteady shock passage — time = 0.080 msec.

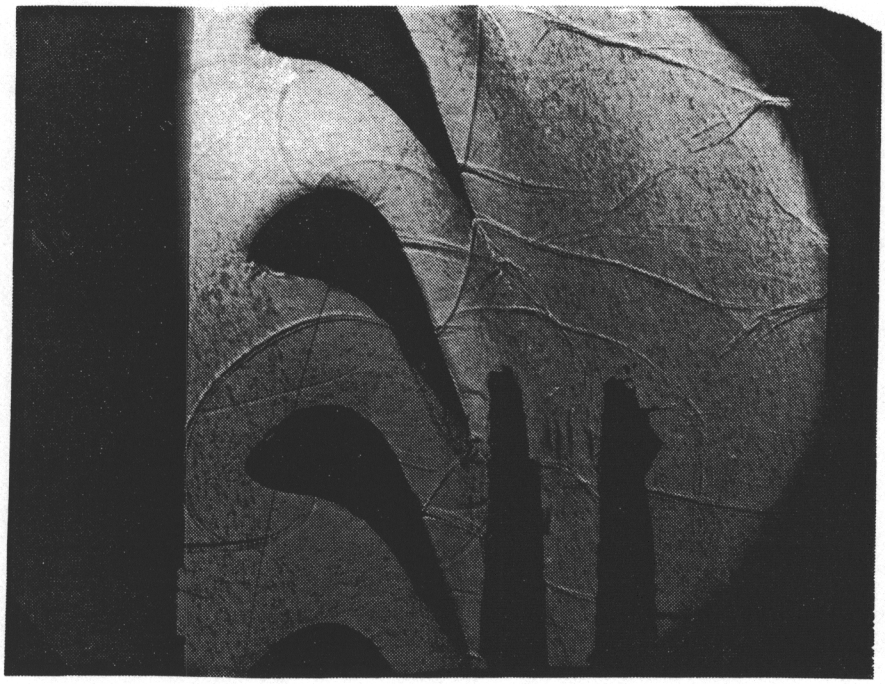

Figure 31e: Shadowgraph: cascade unsteady shock passage — time = 0.108 msec.

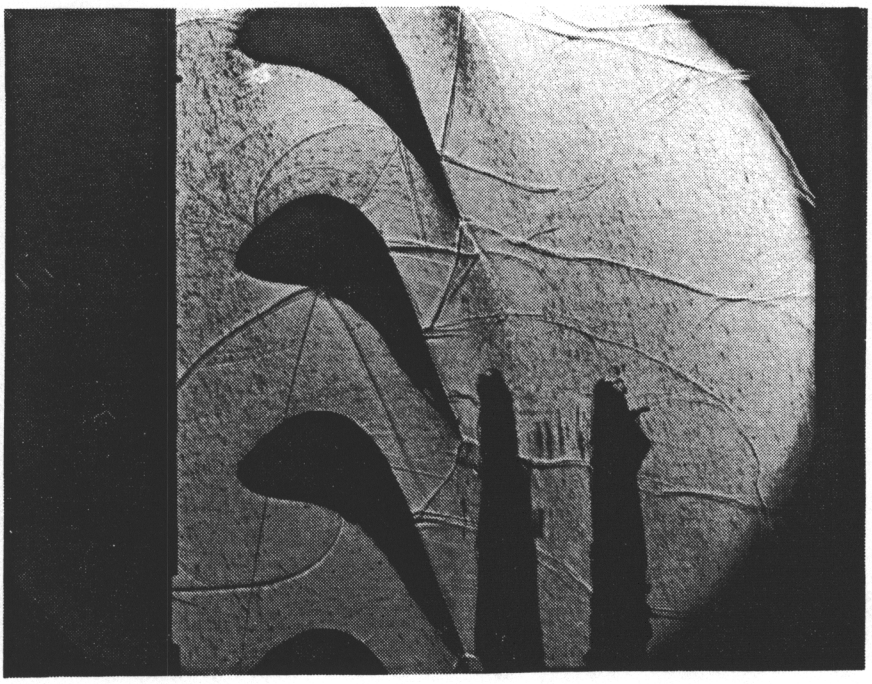

Figure 31f: Shadowgraph: cascade unsteady shock passage — time = 0.121 msec.

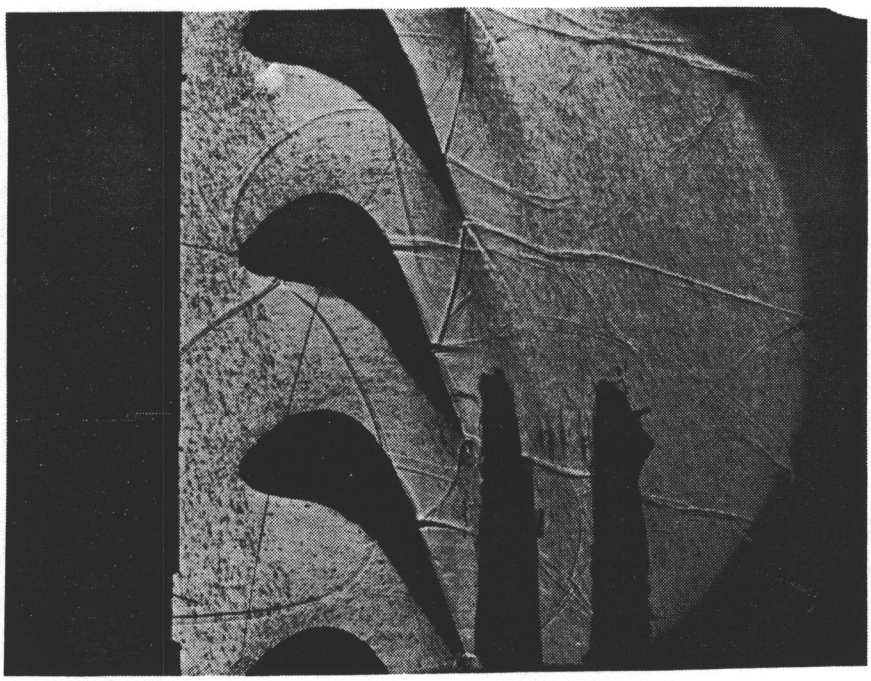

Figure 31g: Shadowgraph: cascade unsteady shock passage — time = 0.133 msec.

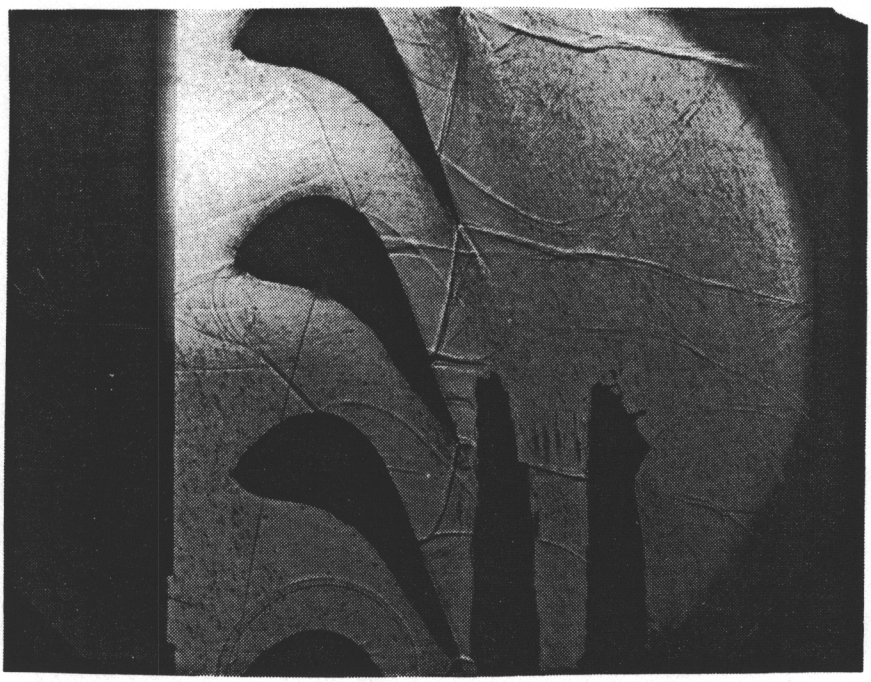

Figure 31h: Shadowgraph: cascade unsteady shock passage — time = 0.160 msec.

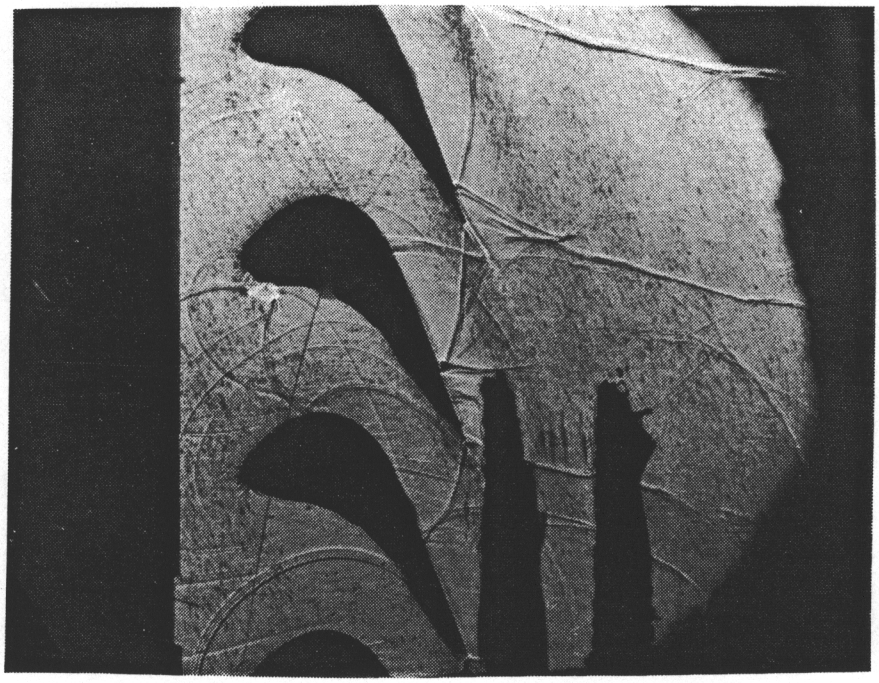

Figure 31i: Shadowgraph: cascade unsteady shock passage — time = 0.185 msec.

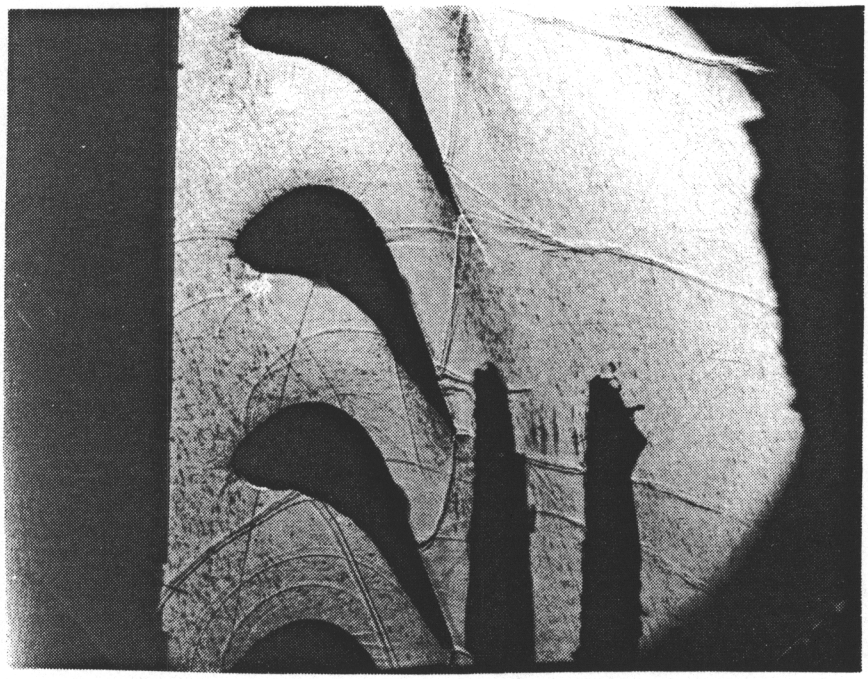

Figure 31j: Shadowgraph: cascade unsteady shock passage — time = 0.214 msec.

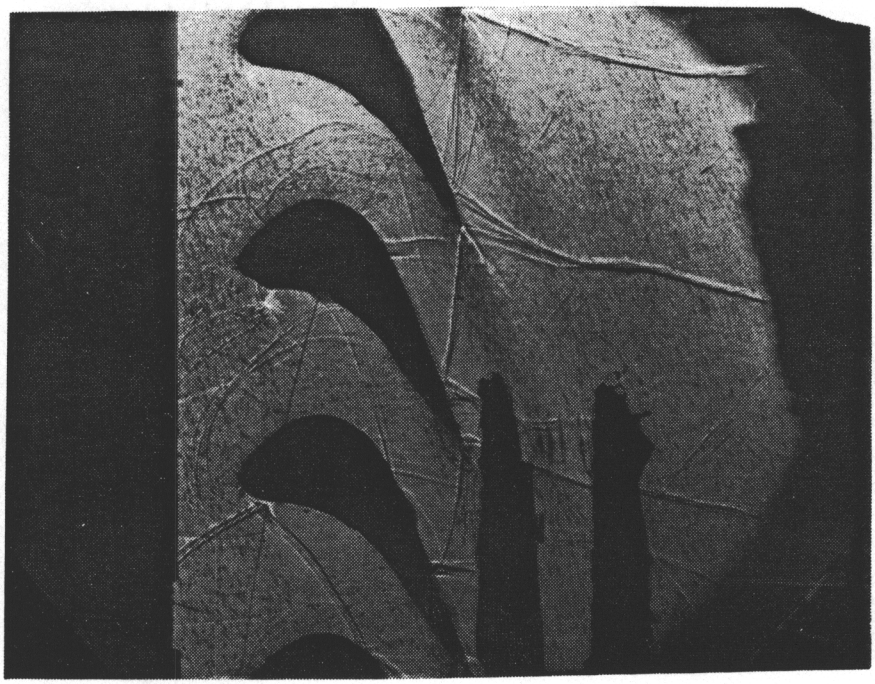

Figure 31k: Shadowgraph: cascade unsteady shock passage — time = 0.243 msec.

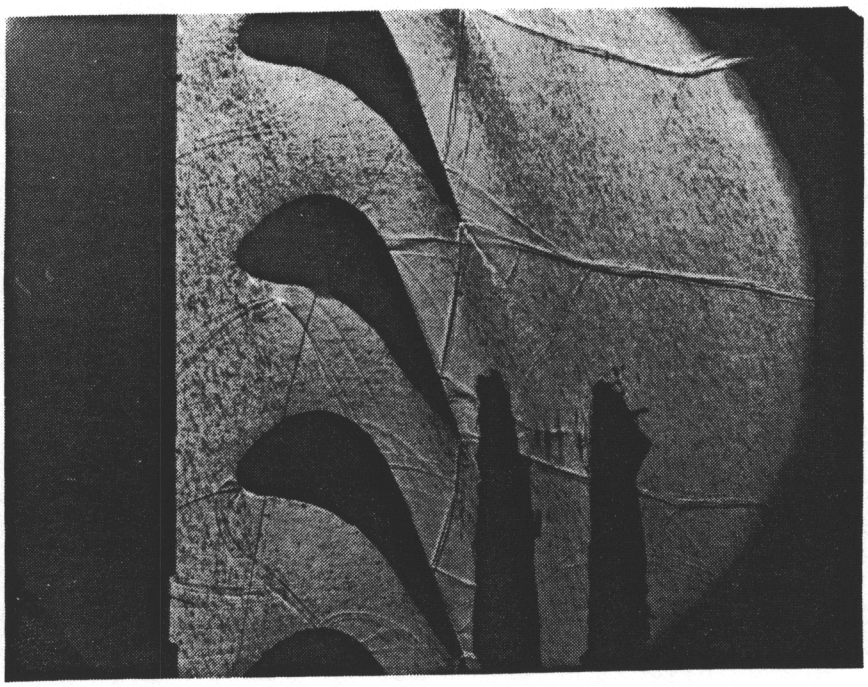

Figure 31l: Shadowgraph: cascade unsteady shock passage — time = 0.270 msec.

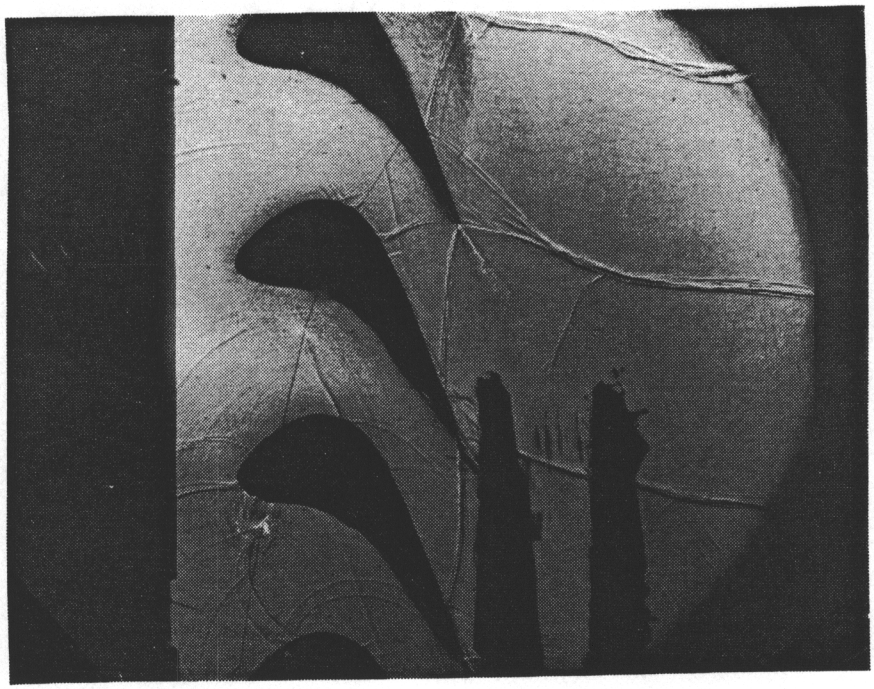

Figure 31m: Shadowgraph: cascade unsteady shock passage — time = 0.295 msec.

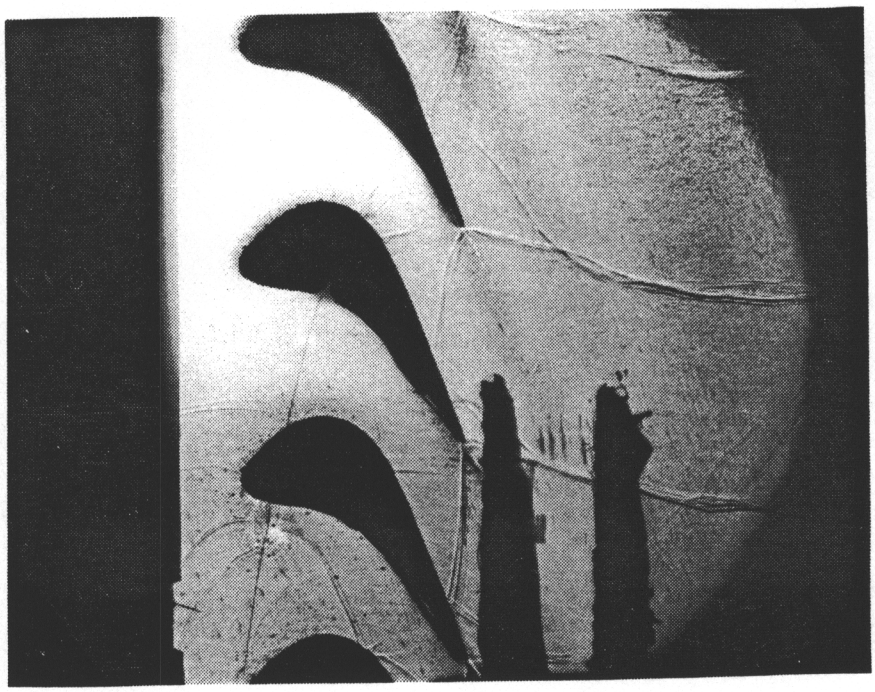

Figure 31n: Shadowgraph: cascade unsteady shock passage — time = 0.353 msec.

Figure 31o: Shadowgraph: cascade unsteady shock passage — time = 0.380 msec.

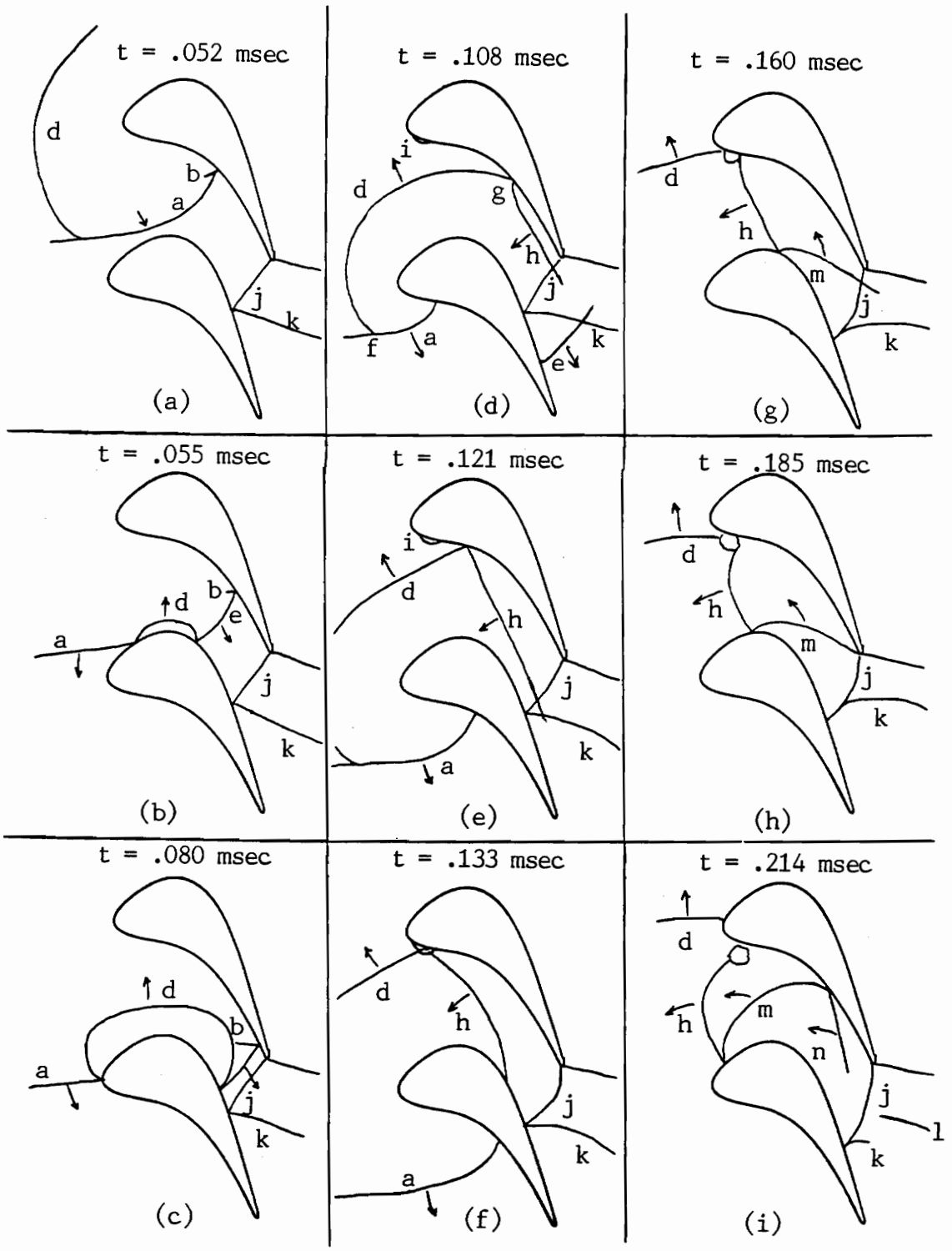

Figure 32: Shock wave propagation through blade passage.

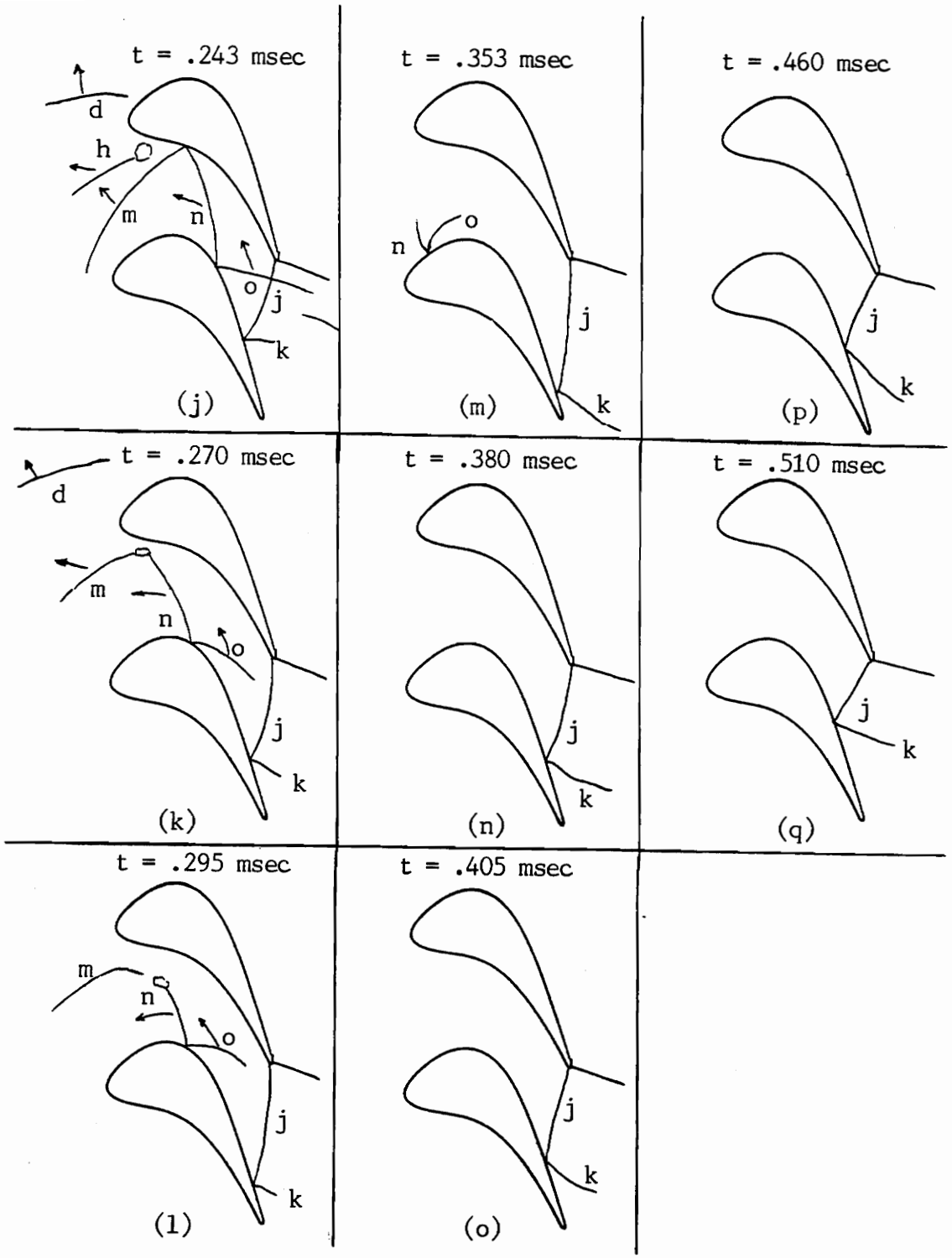

Figure 32: (continued).

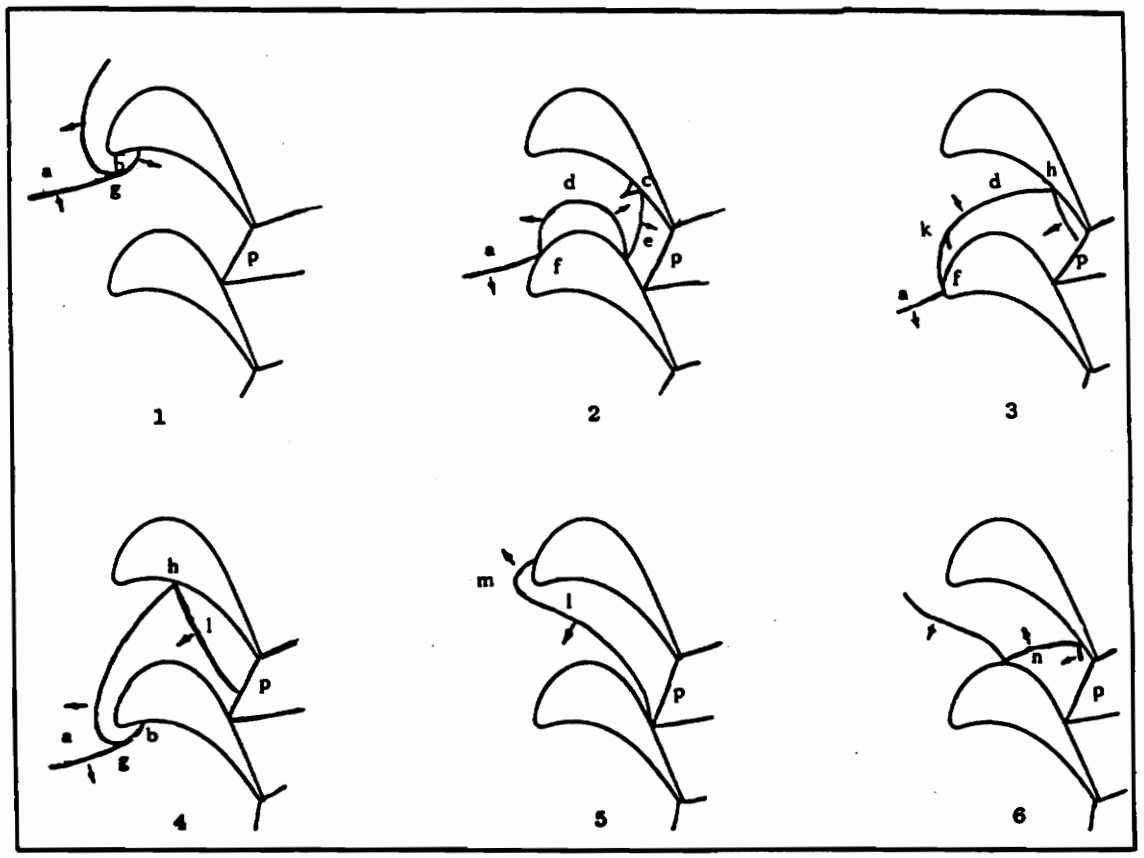

Figure 33: Propagation of a single shock wave through the rotor passage (from [4]).

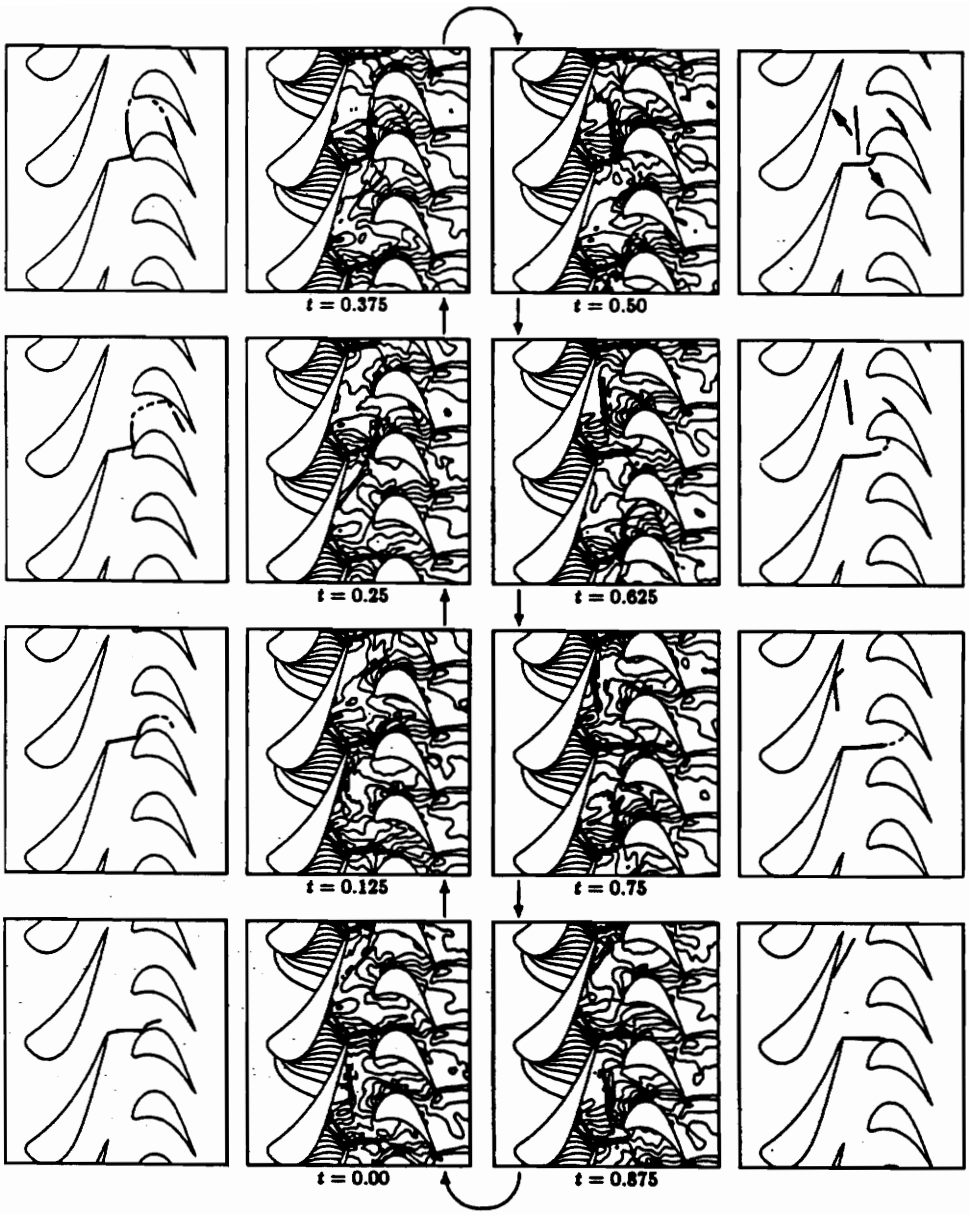

Figure 34: Pressure contours in unsteady stator/rotor interaction (from [6]).

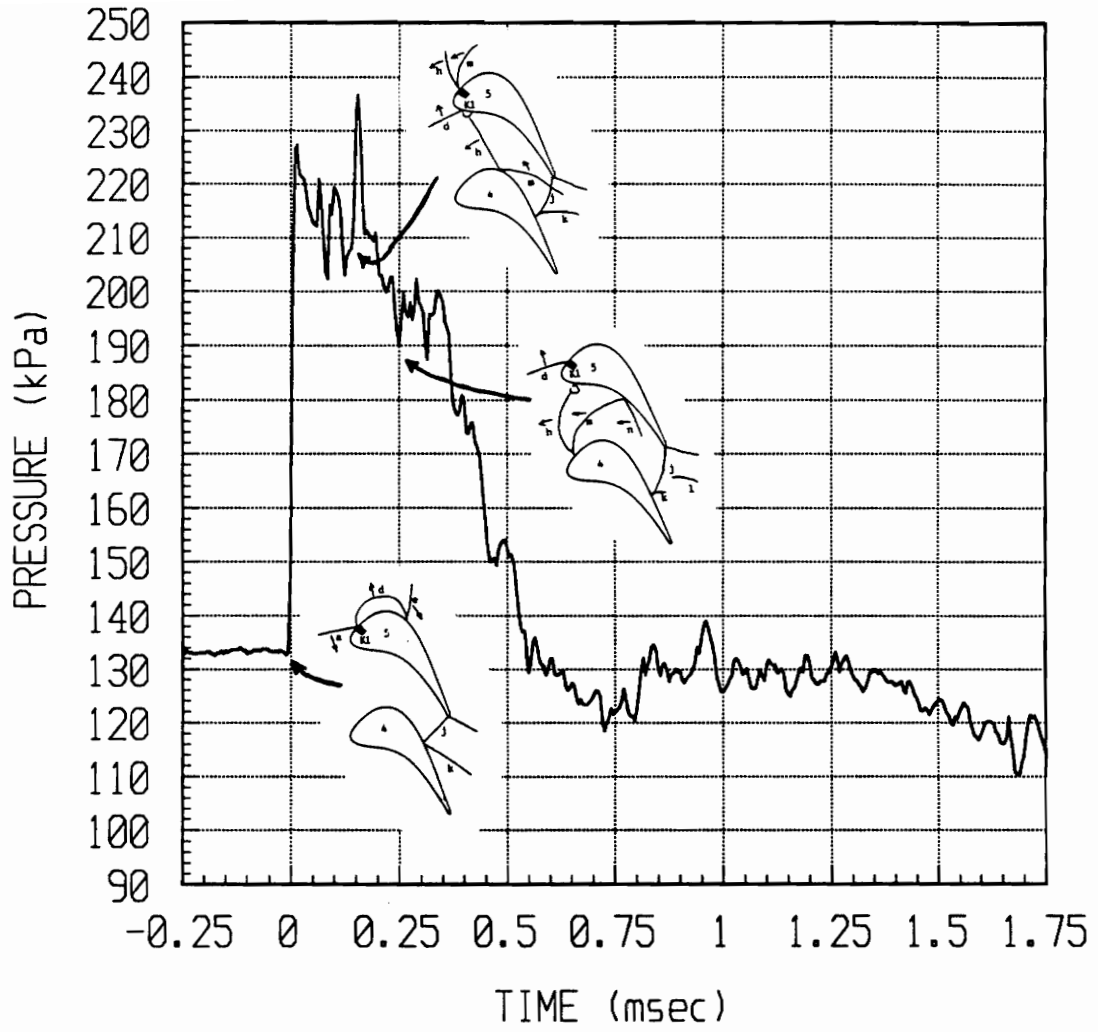

Figure 35a: Absolute pressure vs time for Kulite #1. Time = –0.25 to 1.75 msec.

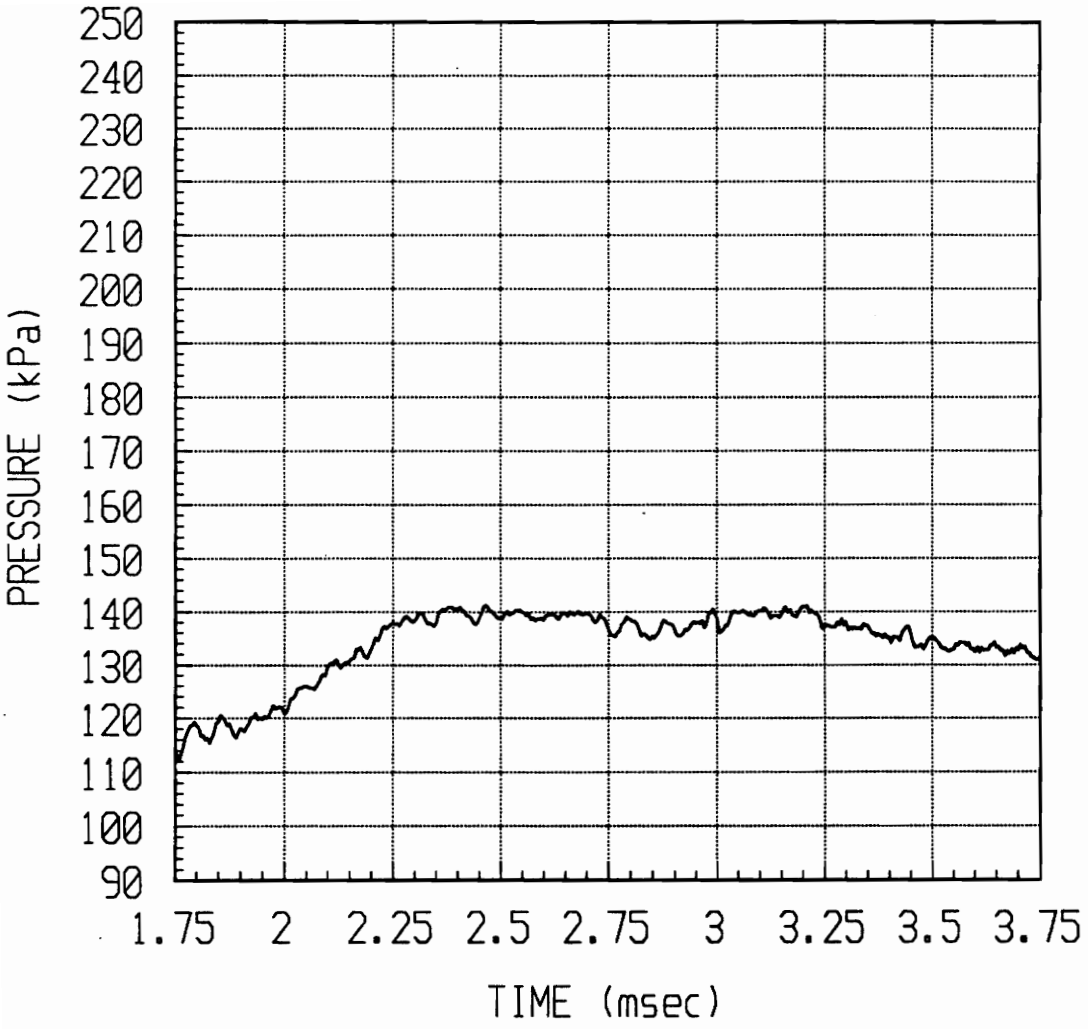

Figure 35b: Absolute pressure vs time for Kulite #1. Time = 1.75 to 3.75 msec.

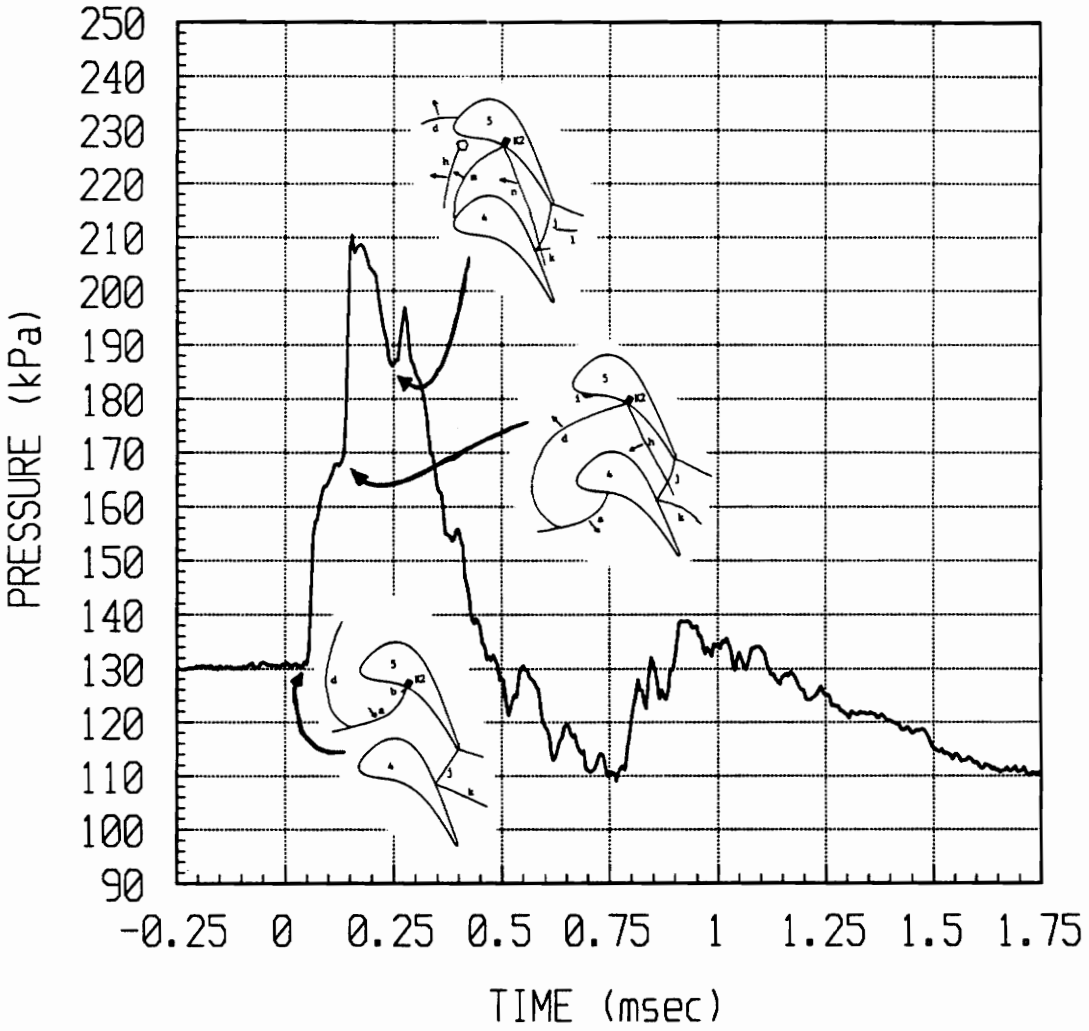

Figure 36a: Absolute pressure vs time for Kulite #2. Time = –0.25 to 1.75 msec.

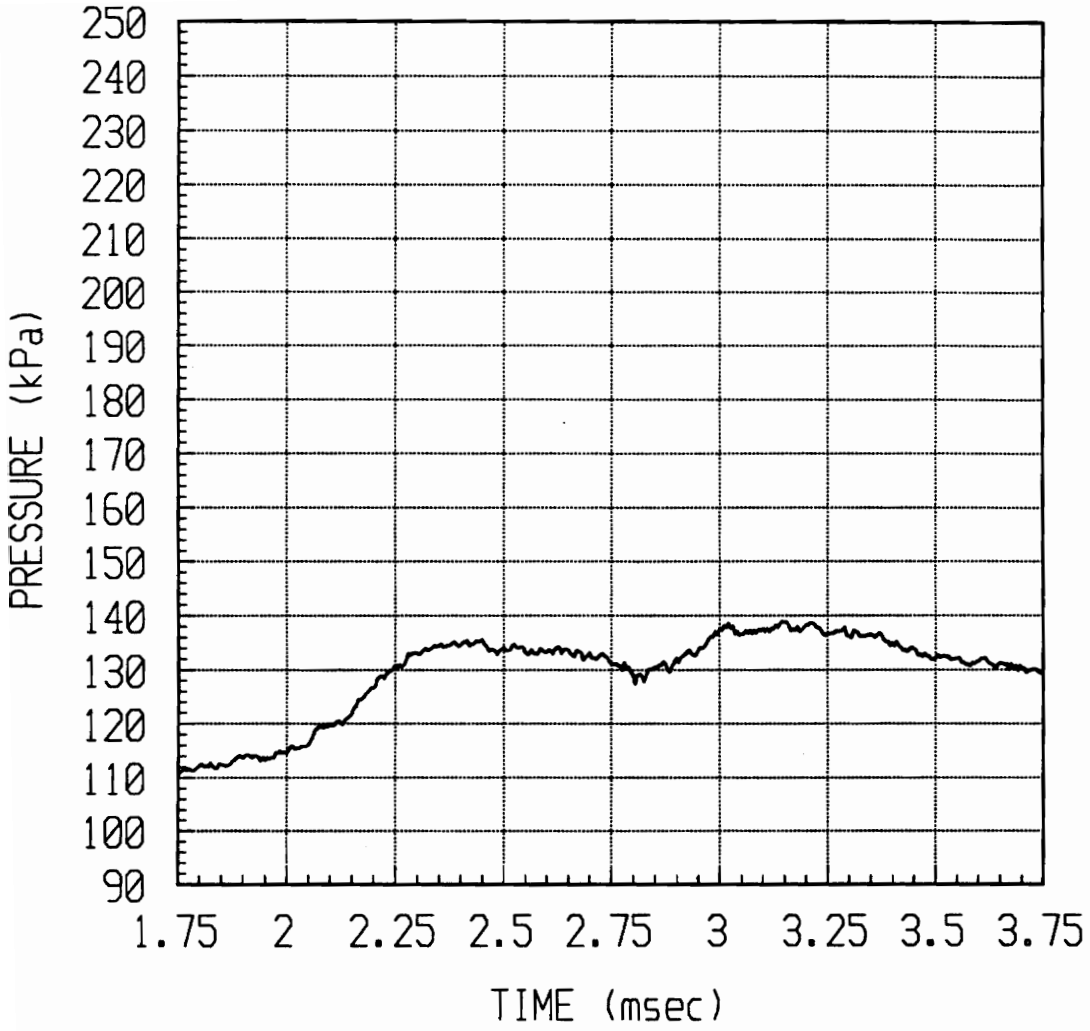

Figure 36b: Absolute pressure vs time for Kulite #2. Time = 1.75 to 3.75 msec.

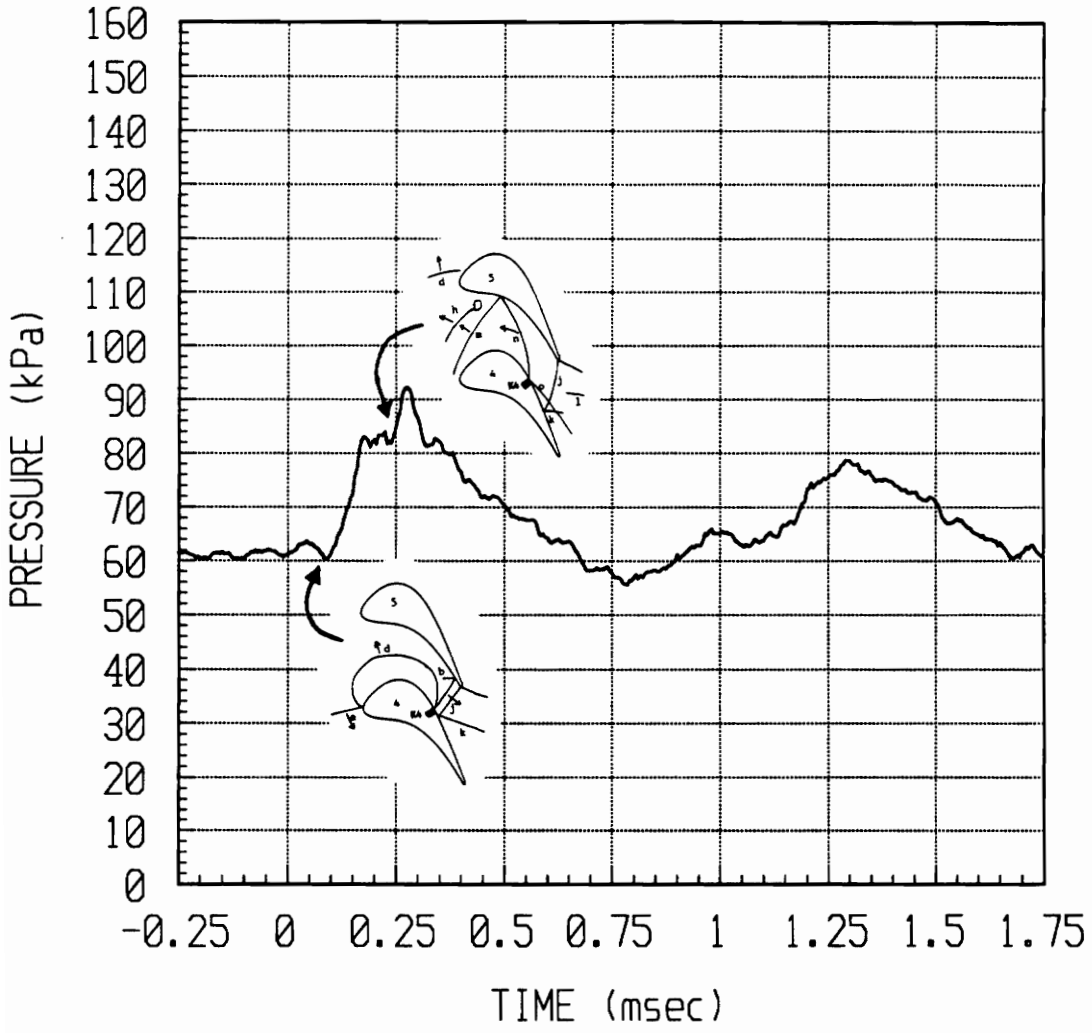

Figure 37a: Absolute pressure vs time for Kulite #4. Time = –0.25 to 1.75 msec.

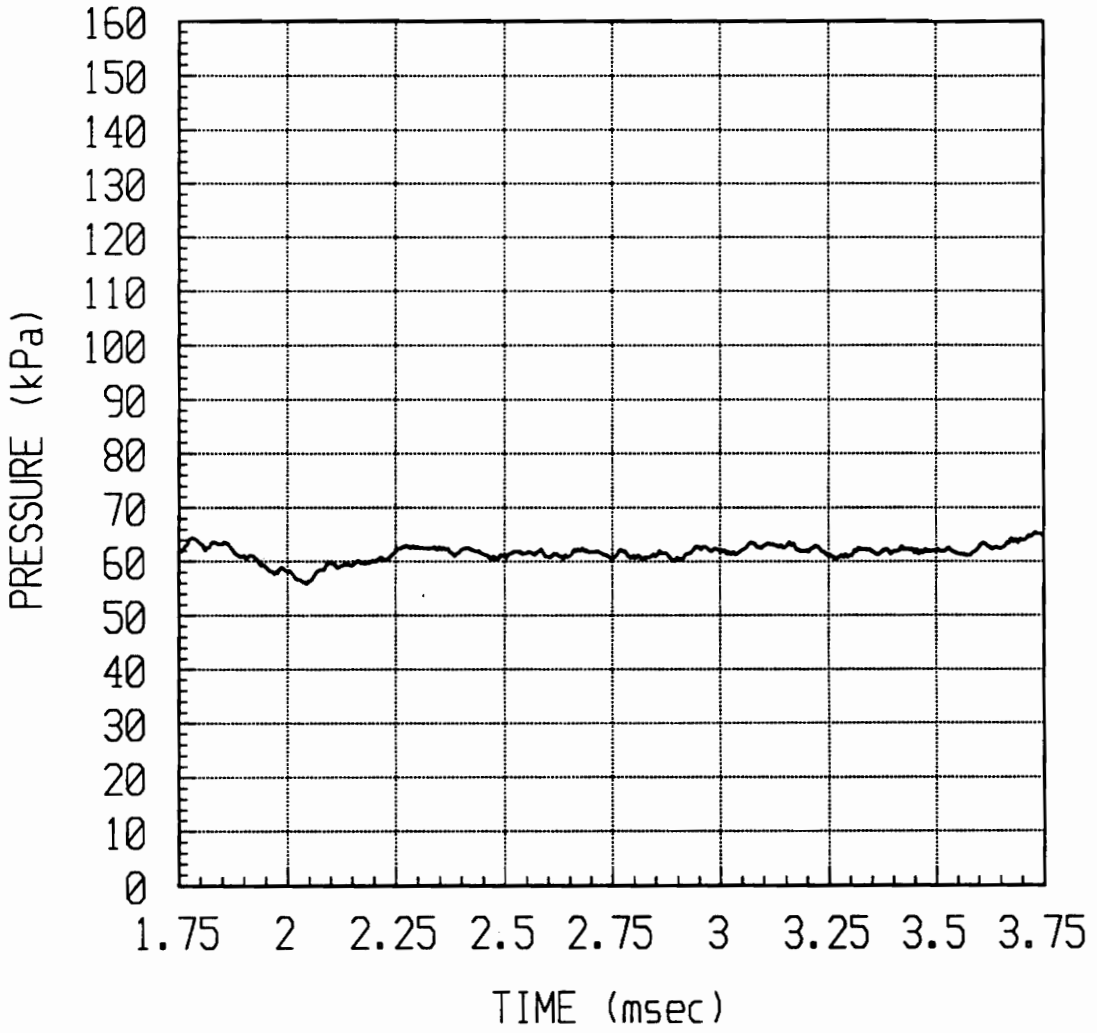

Figure 37b: Absolute pressure vs time for Kulite #4. Time = 1.75 to 3.75 msec.

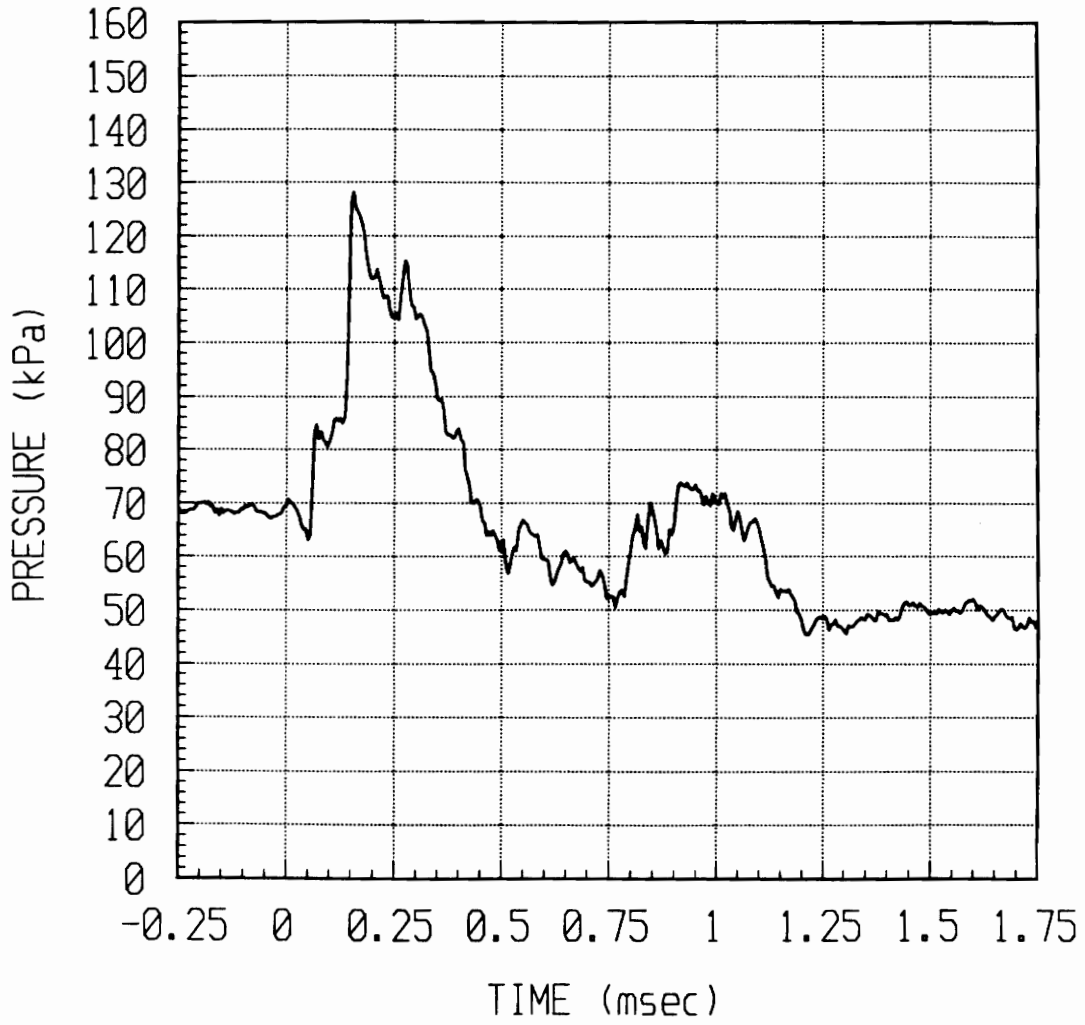

Figure 38a: Estimated lift vs time. Time = –0.25 to 1.75 msec.

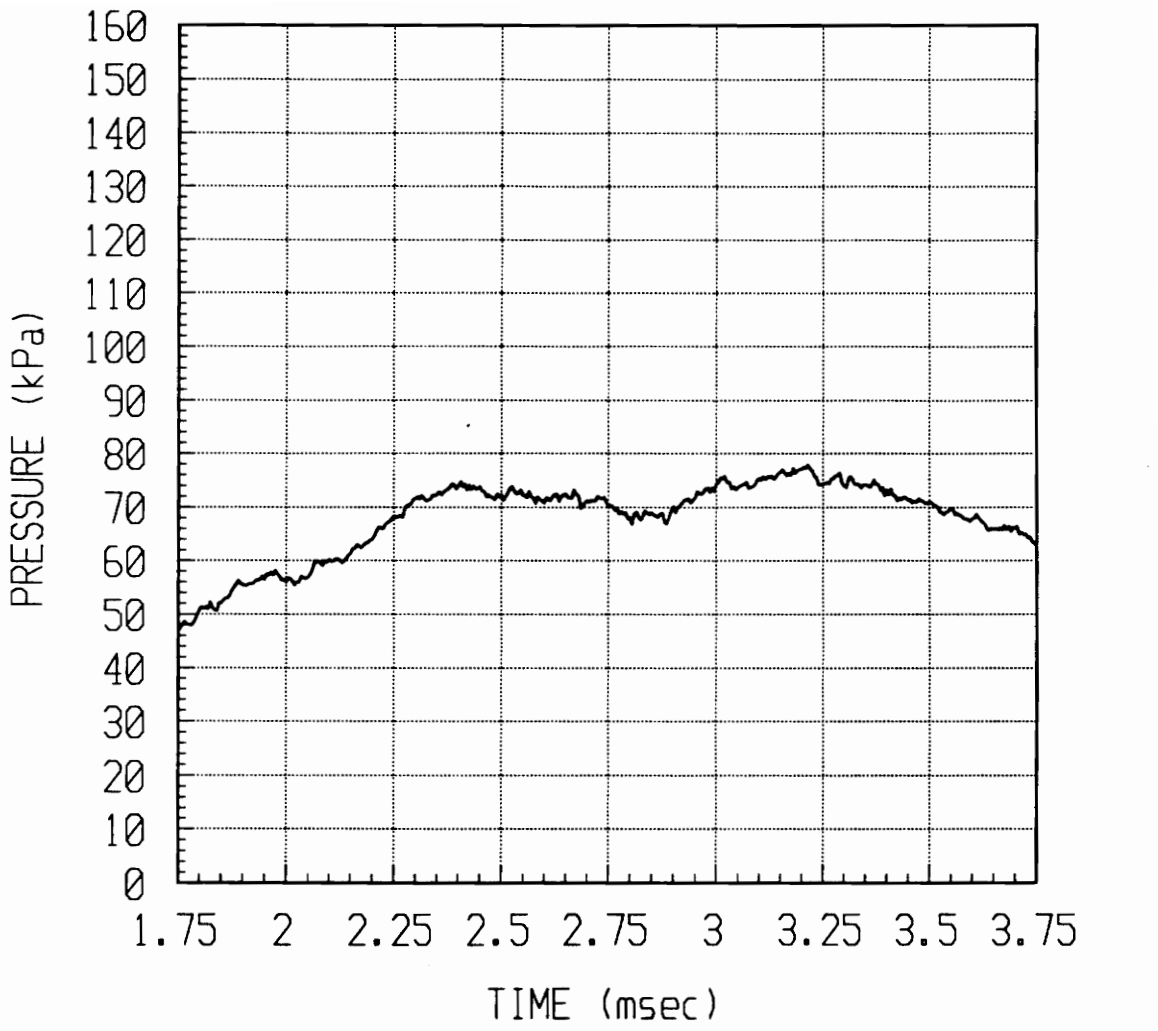

Figure 38b: Estimated lift vs time. Time = 1.75 to 3.75 msec.

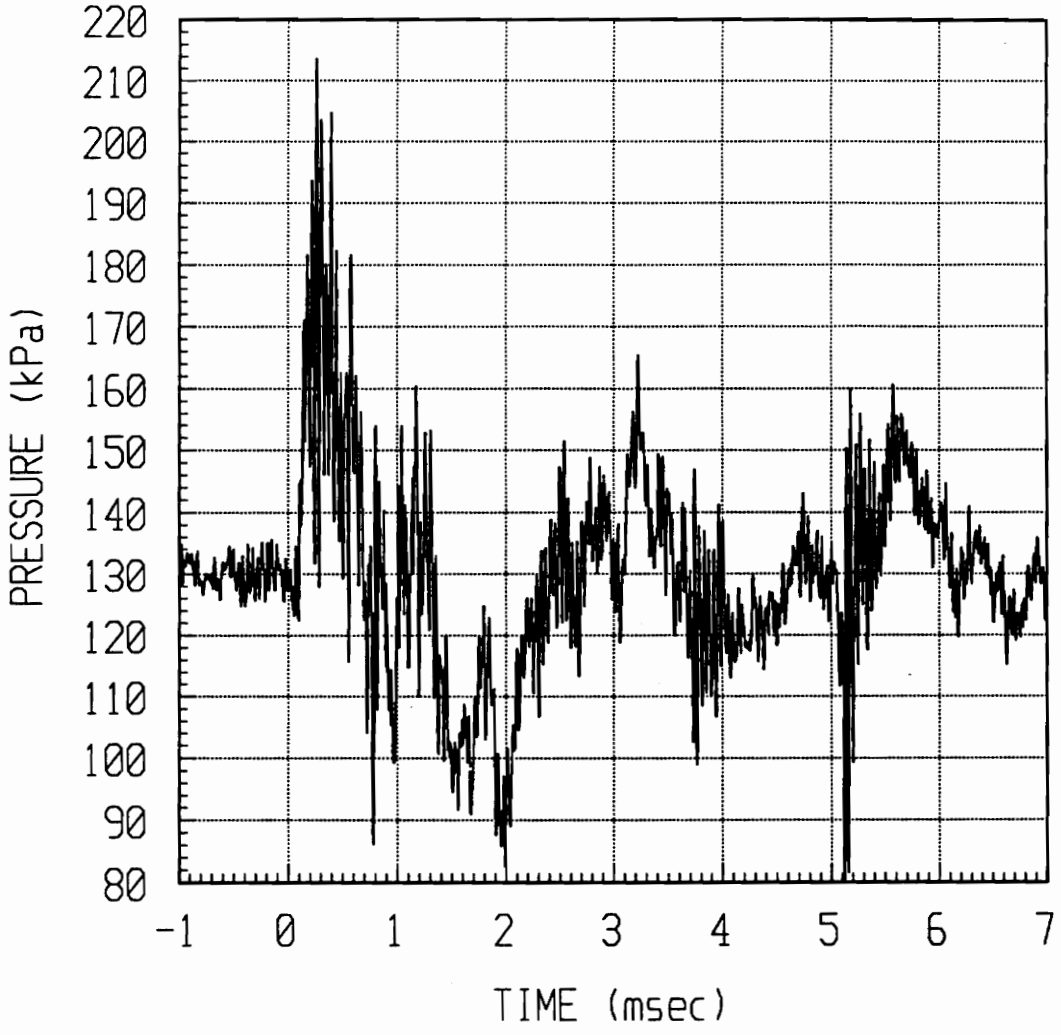

Figure 39: Raw absolute pressure vs time for Kulite #5, position 0.

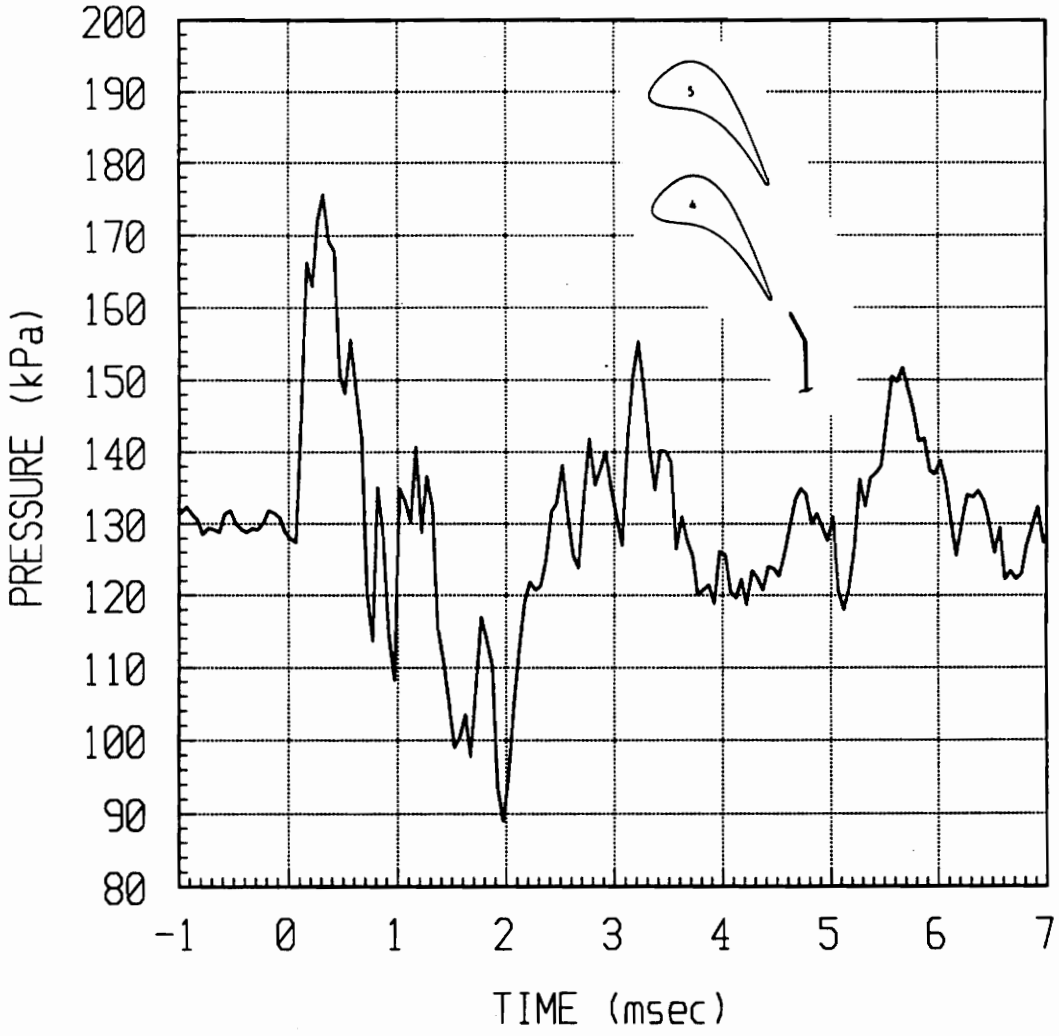

Figure 40: Boxcar-averaged absolute pressure vs time for Kulite #5 , position 0.

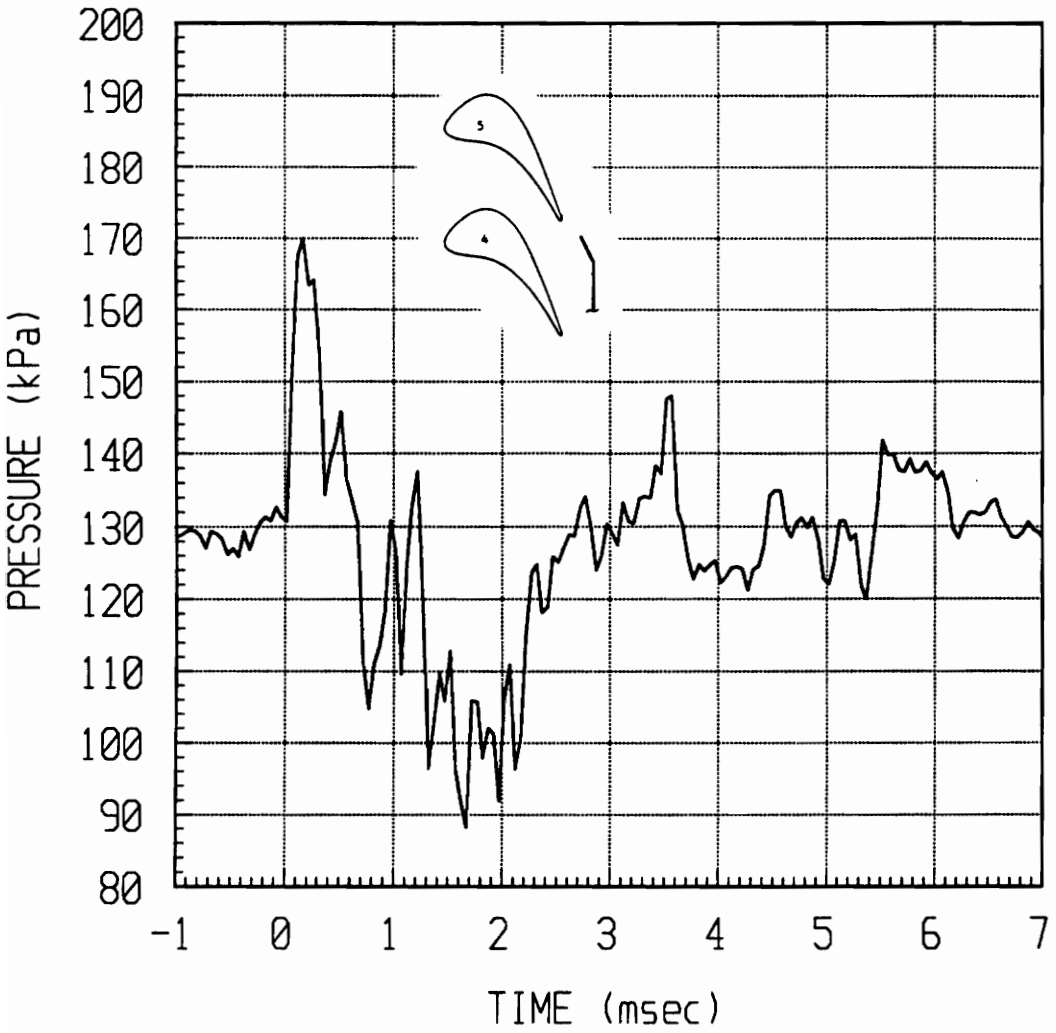

Figure 41: Boxcar-averaged absolute pressure vs time for Kulite #5, position 9.

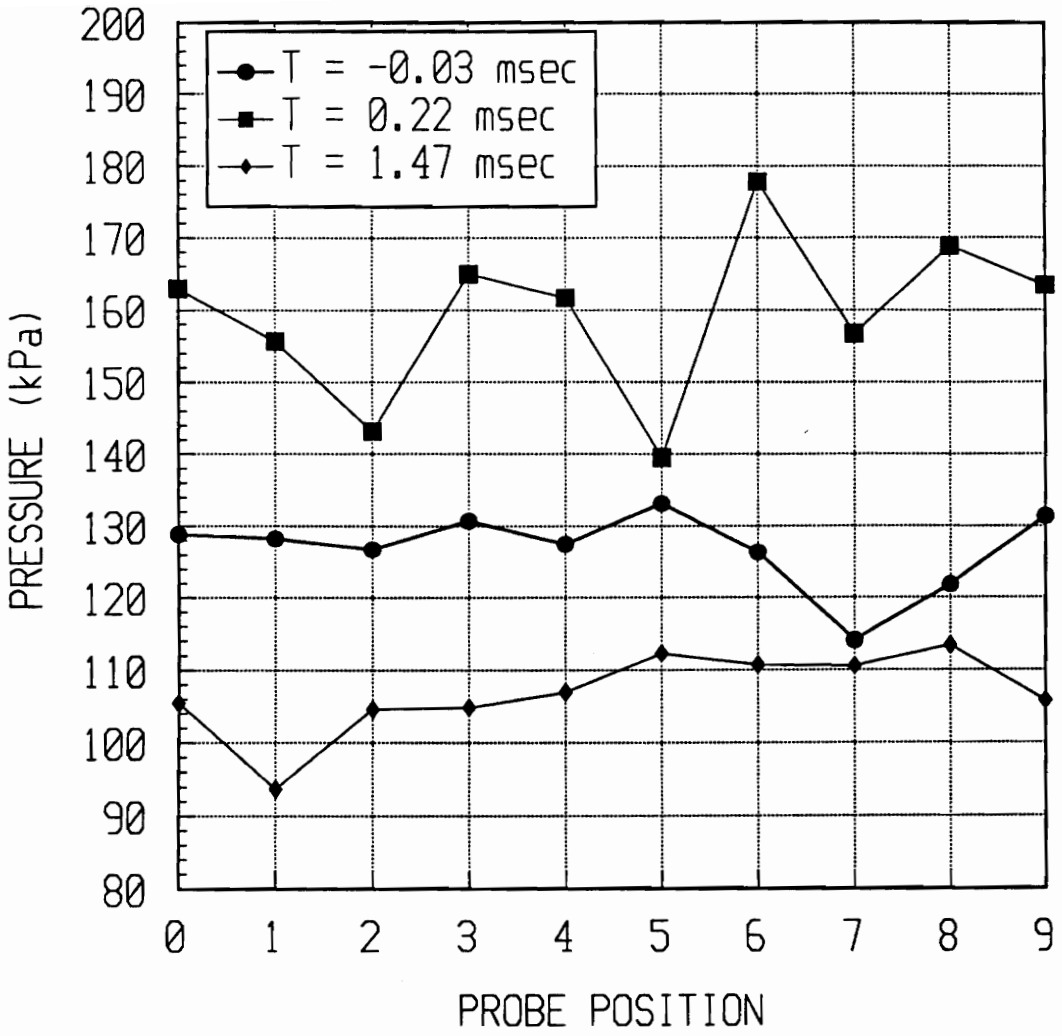

Figure 42: Wake absolute pressure profiles: steady-state, maximum, and minimum.

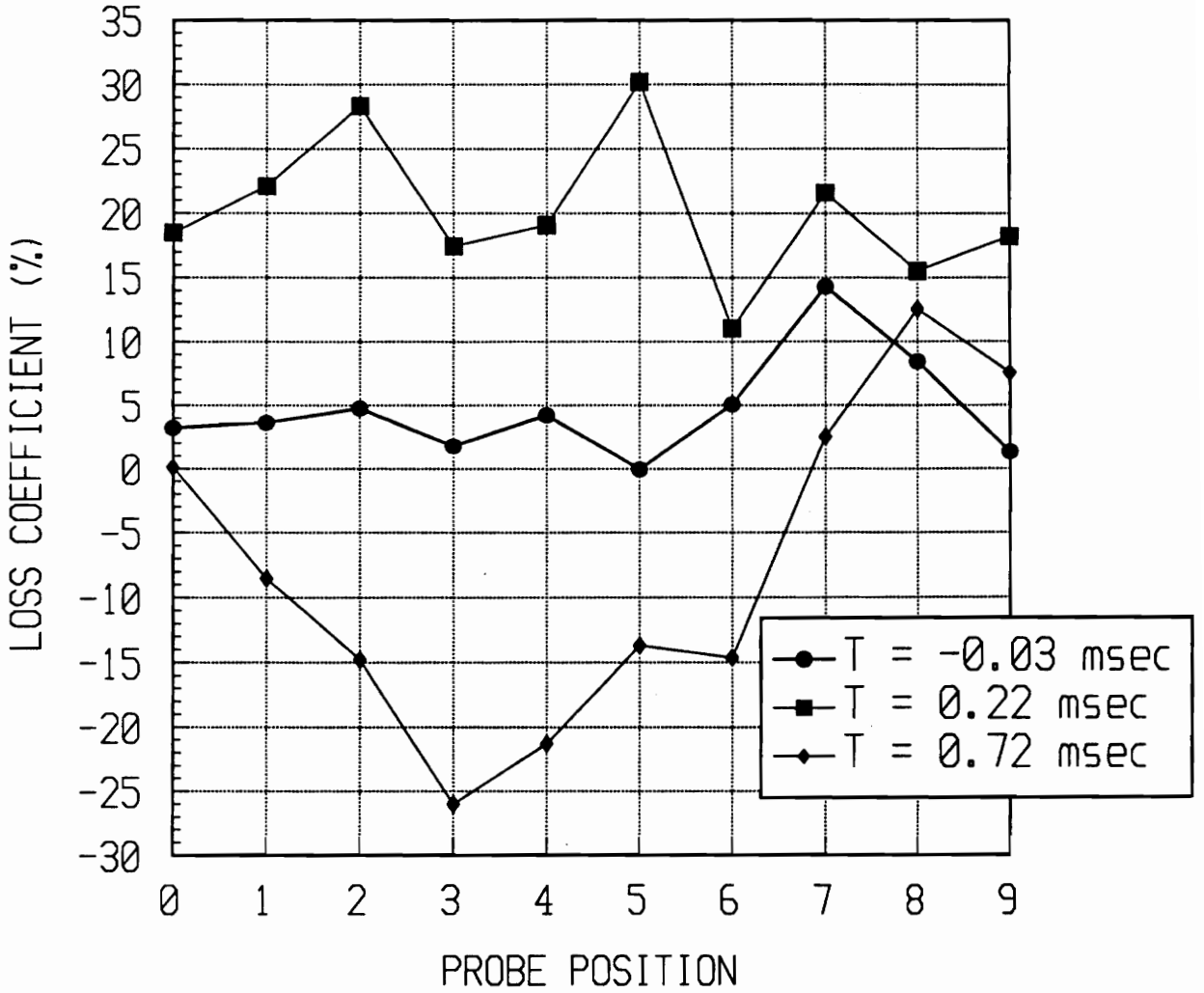

Figure 43: Pressure loss profiles: steady-state, maximum and minimum.

9.0 Appendix A

Time-Delay Circuit Diagrams

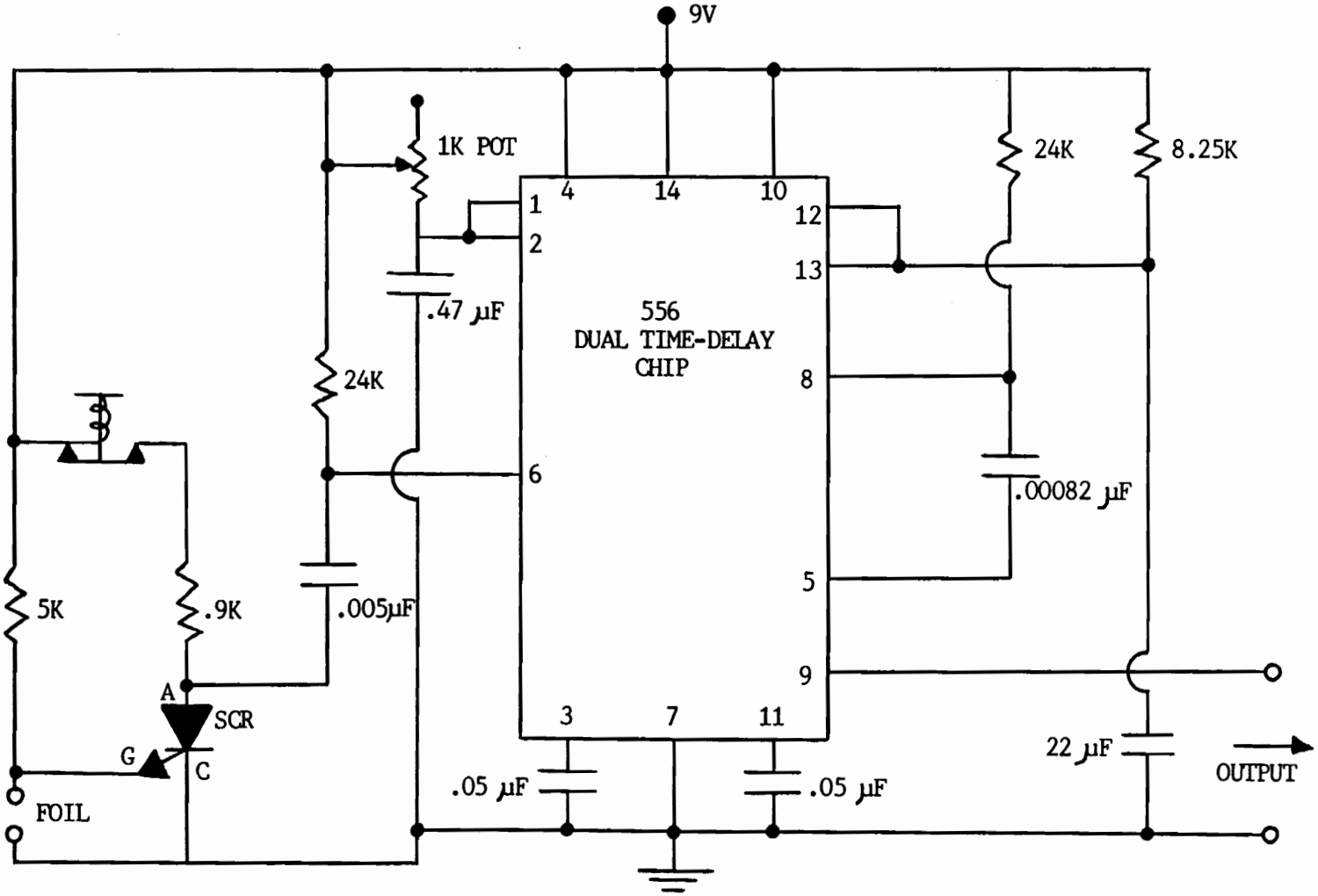

Figure A1: Schematic: time-delay circuit — foil-activated.

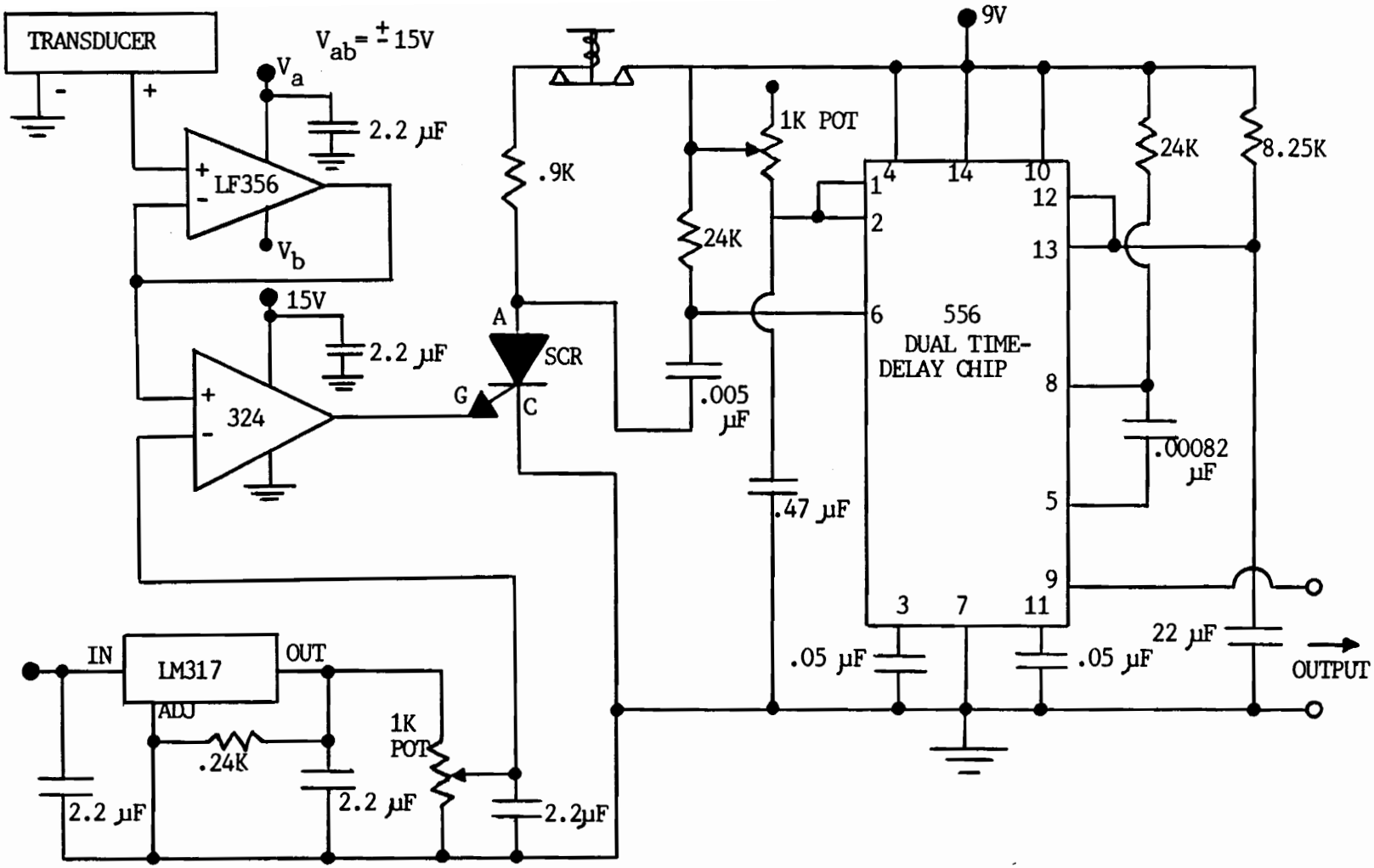

Figure A2: Schematic: time-delay circuit — voltage-activated.

10.0 Appendix B

Unsteady Downstream Pressure Traces

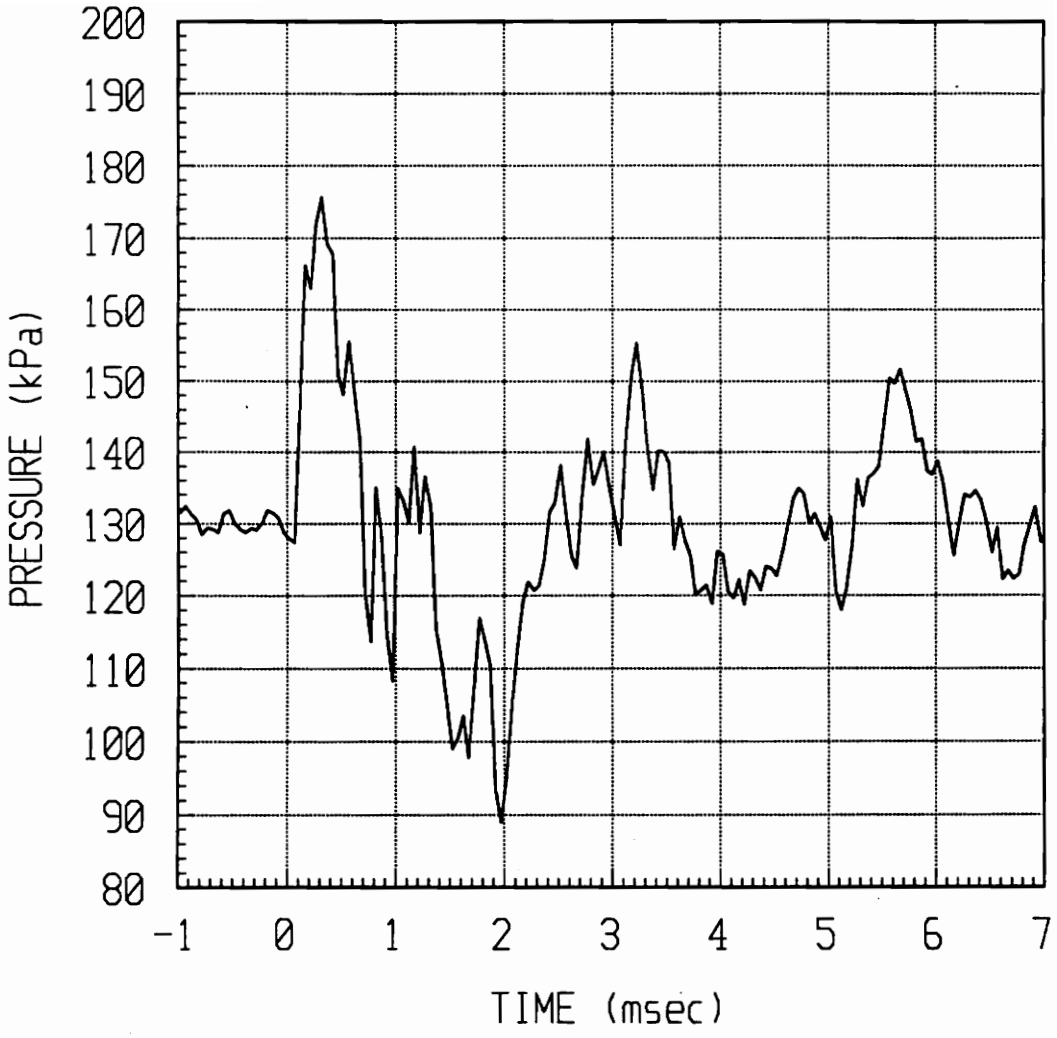

Figure B1: Boxcar-averaged absolute pressure vs time for Kulite #5, position 0.

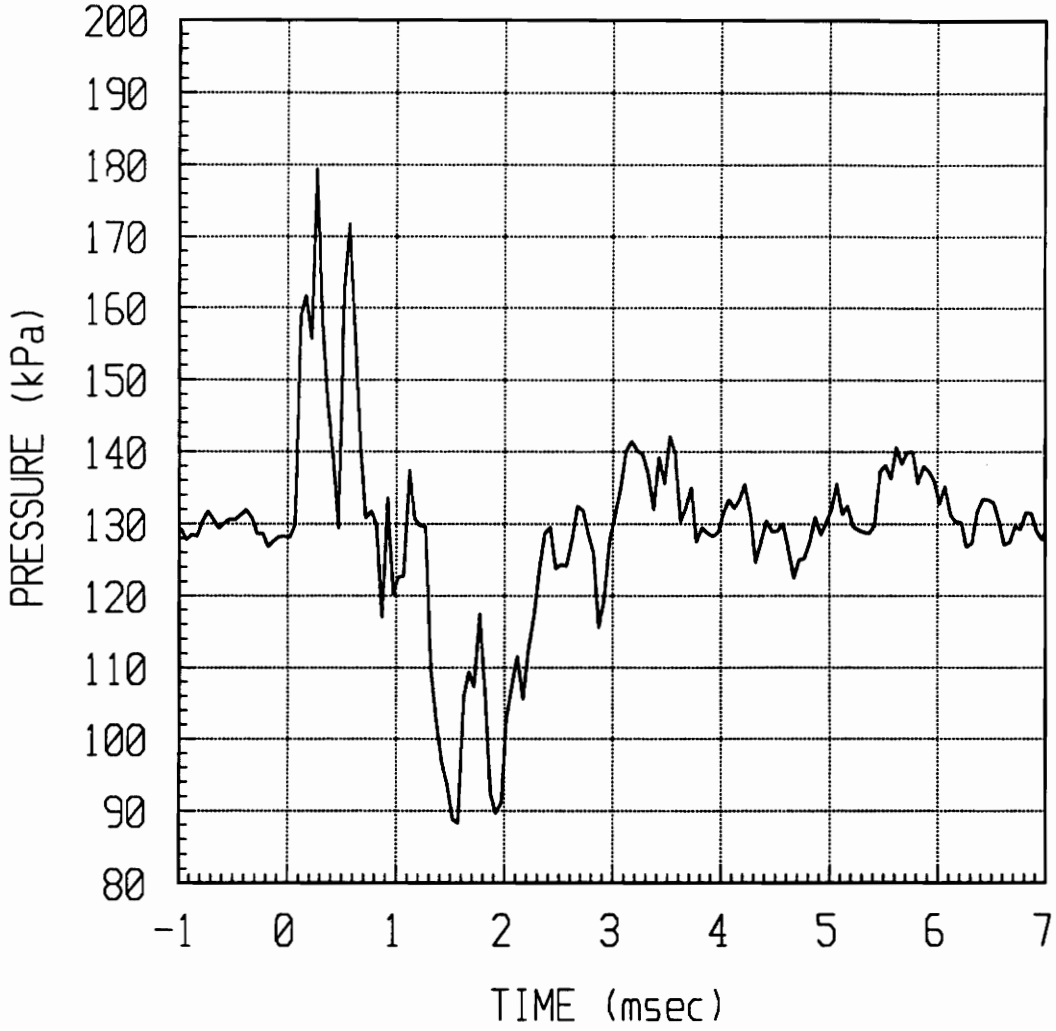

Figure B2: Boxcar-averaged absolute pressure vs time for Kulite #5, position 1.

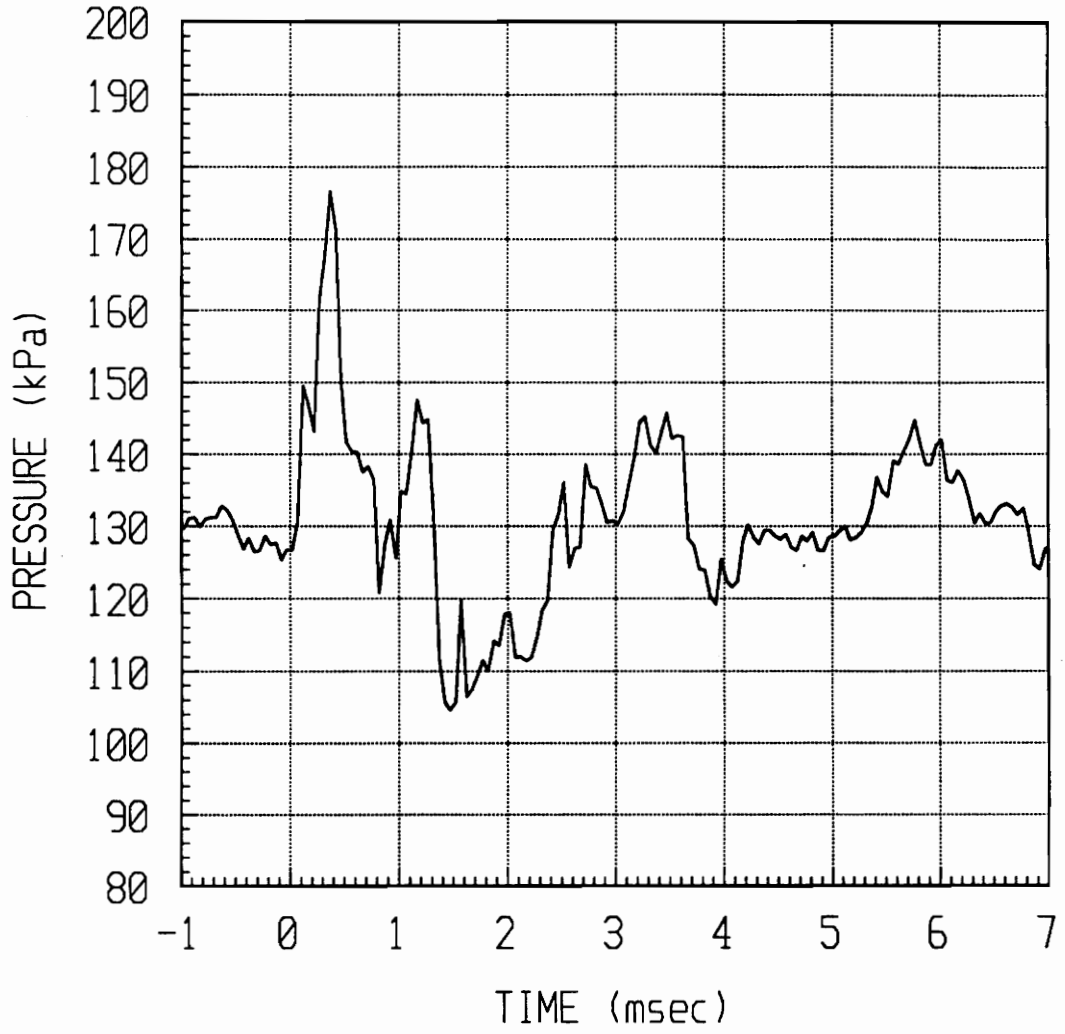

Figure B3: Boxcar-averaged absolute pressure vs time for Kulite #5, position 2.

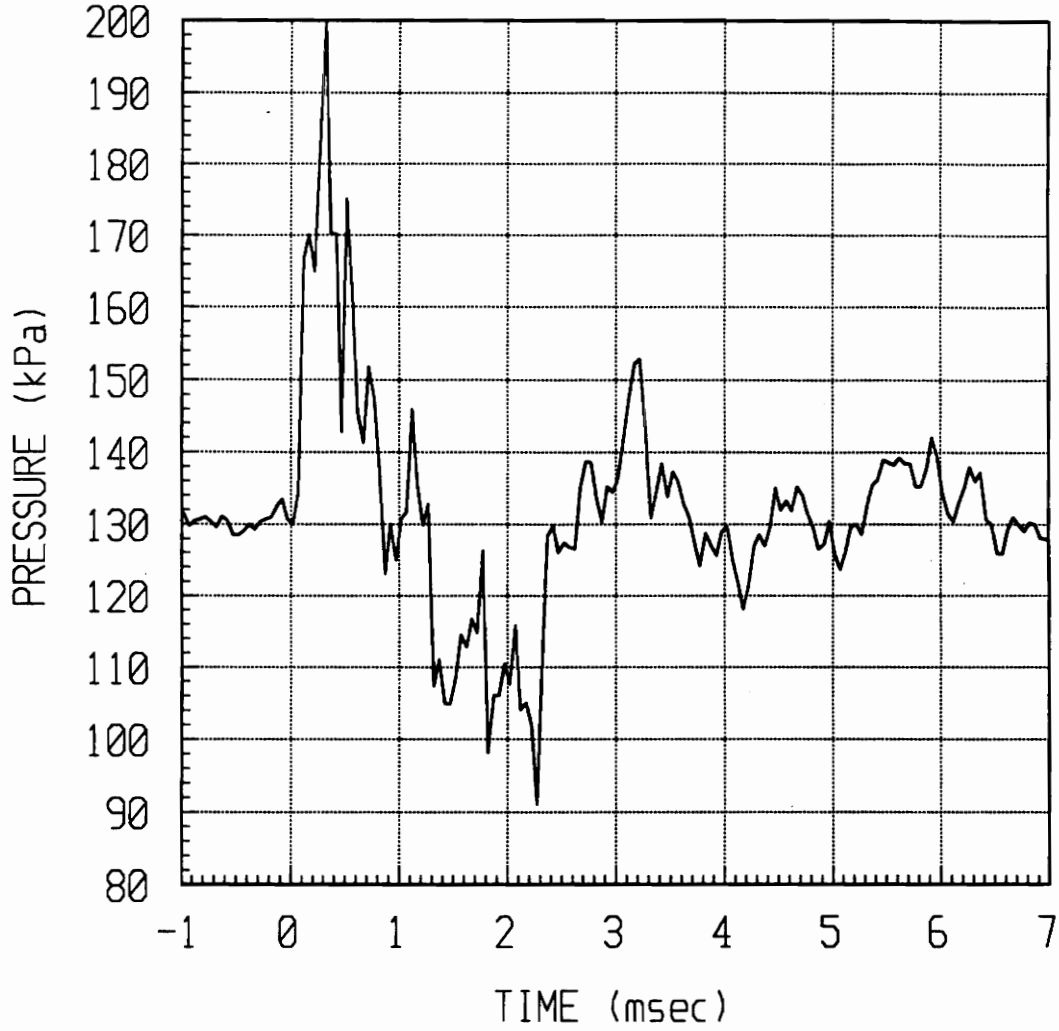

Figure B4: Boxcar-averaged absolute pressure vs time for Kulite #5, position 3.

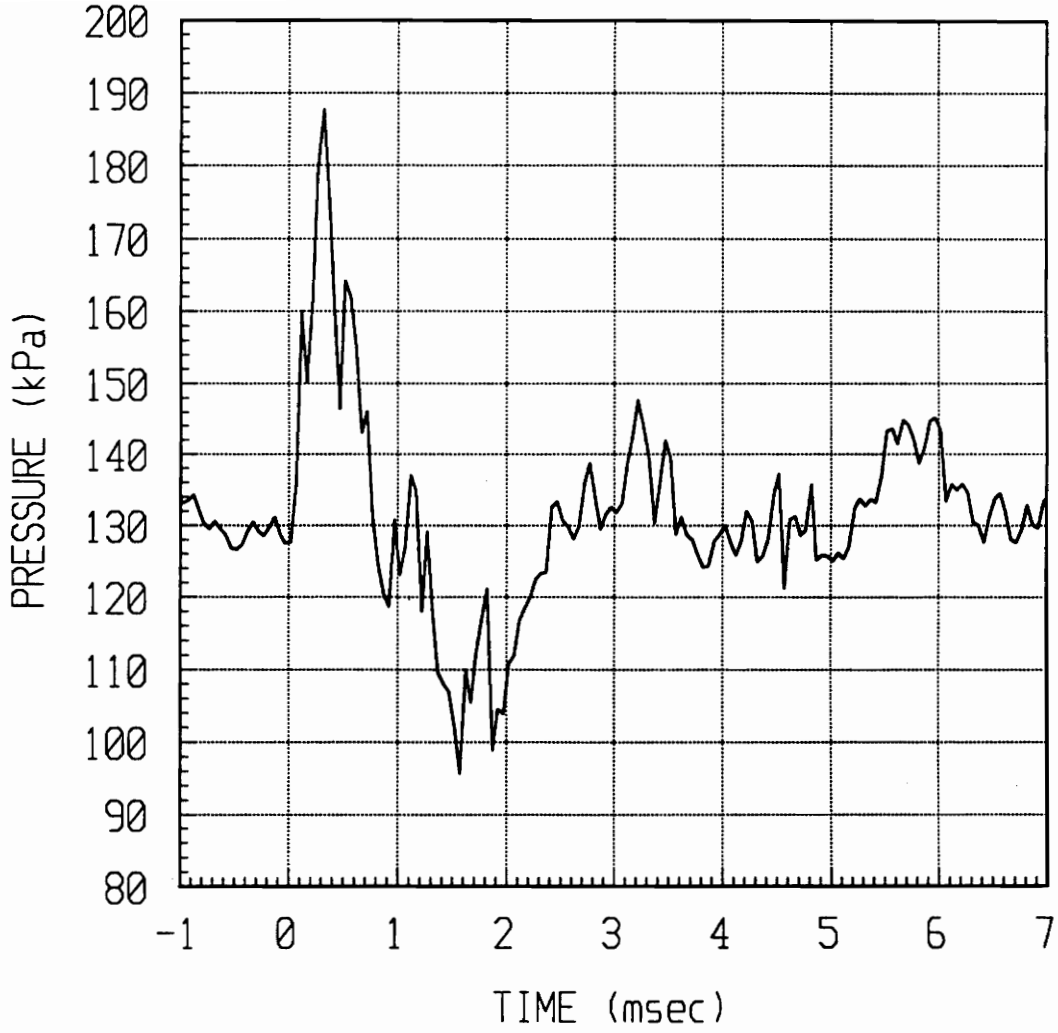

Figure B5: Boxcar-averaged absolute pressure vs time for Kulite #5, position 4.

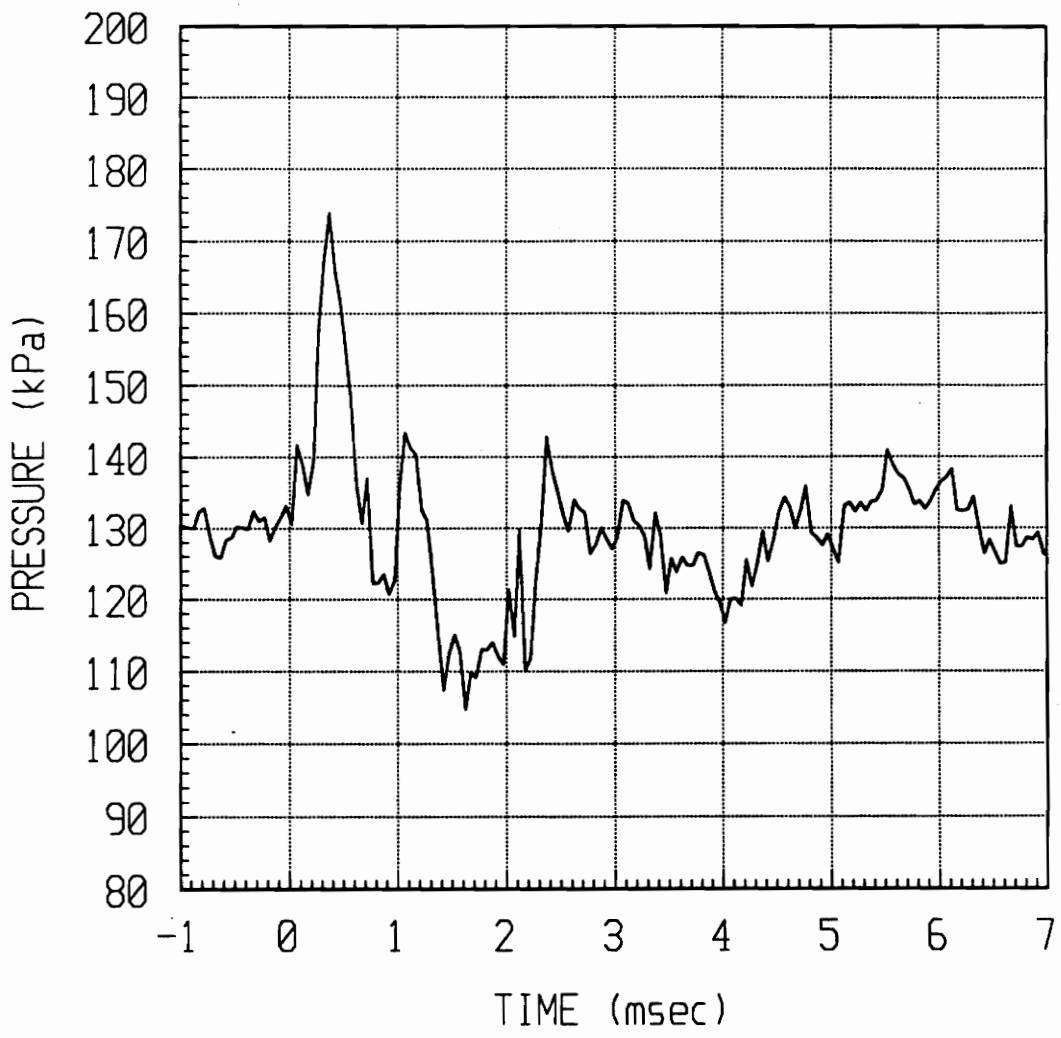

Figure B6: Boxcar-averaged absolute pressure vs time for Kulite #5, position 5.

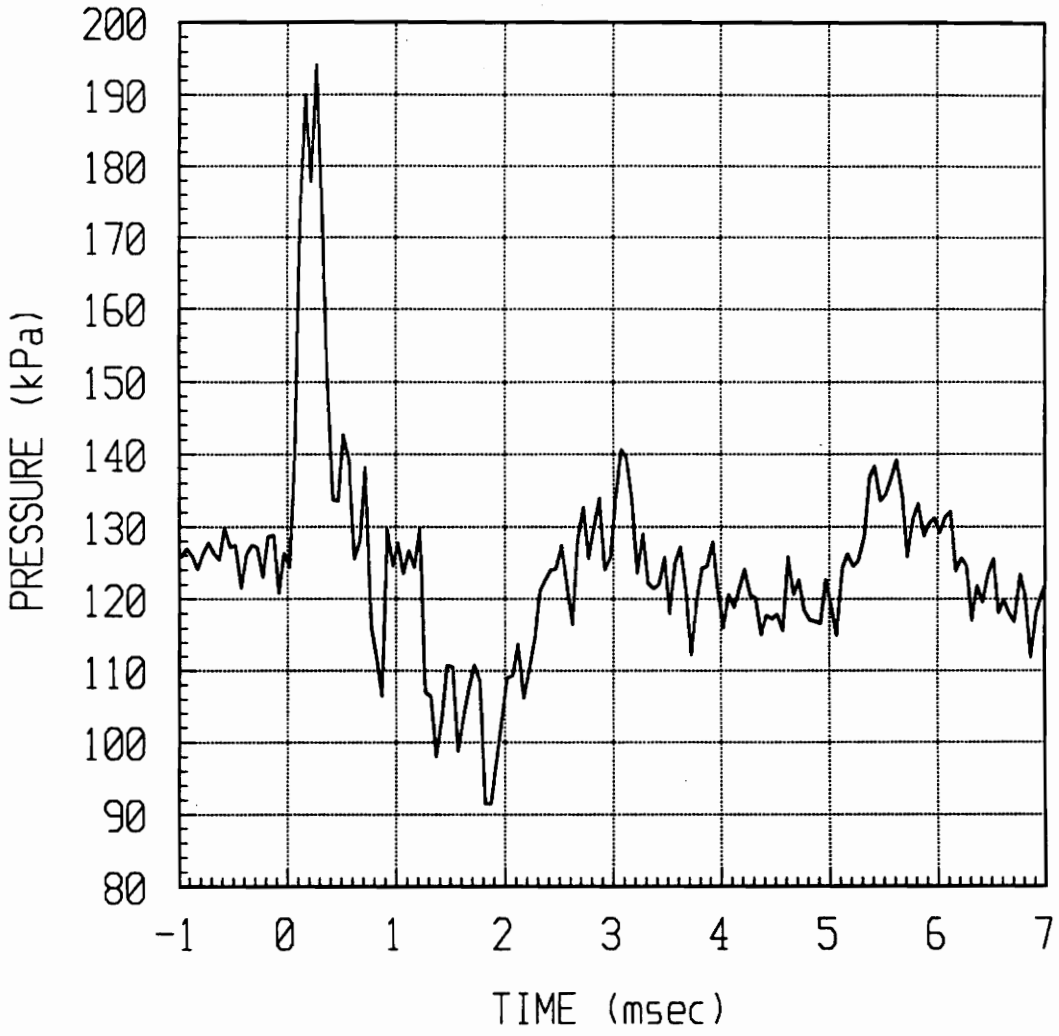

Figure B7: Boxcar-averaged absolute pressure vs time for Kulite #5, position 6.

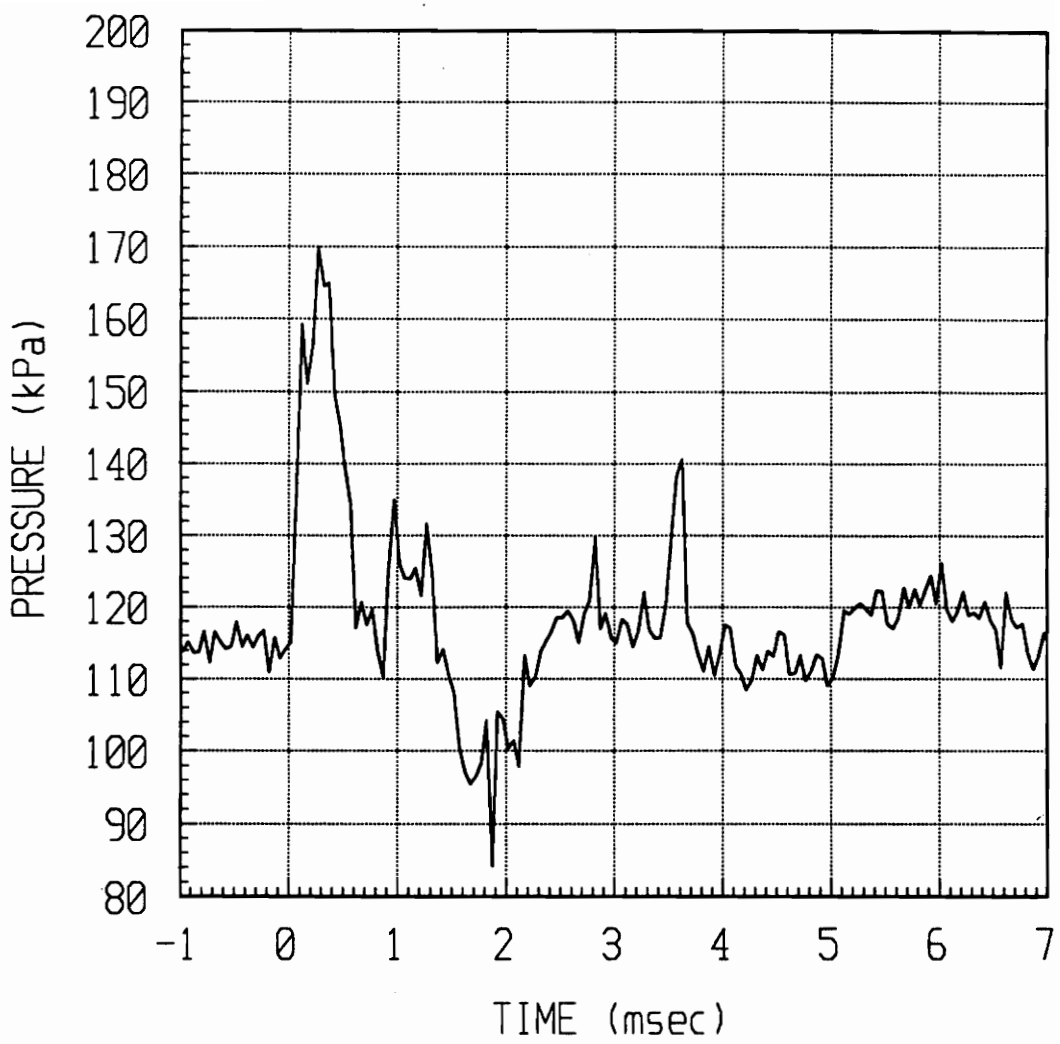

Figure B8: Boxcar-averaged absolute pressure vs time for Kulite #5, position 7.

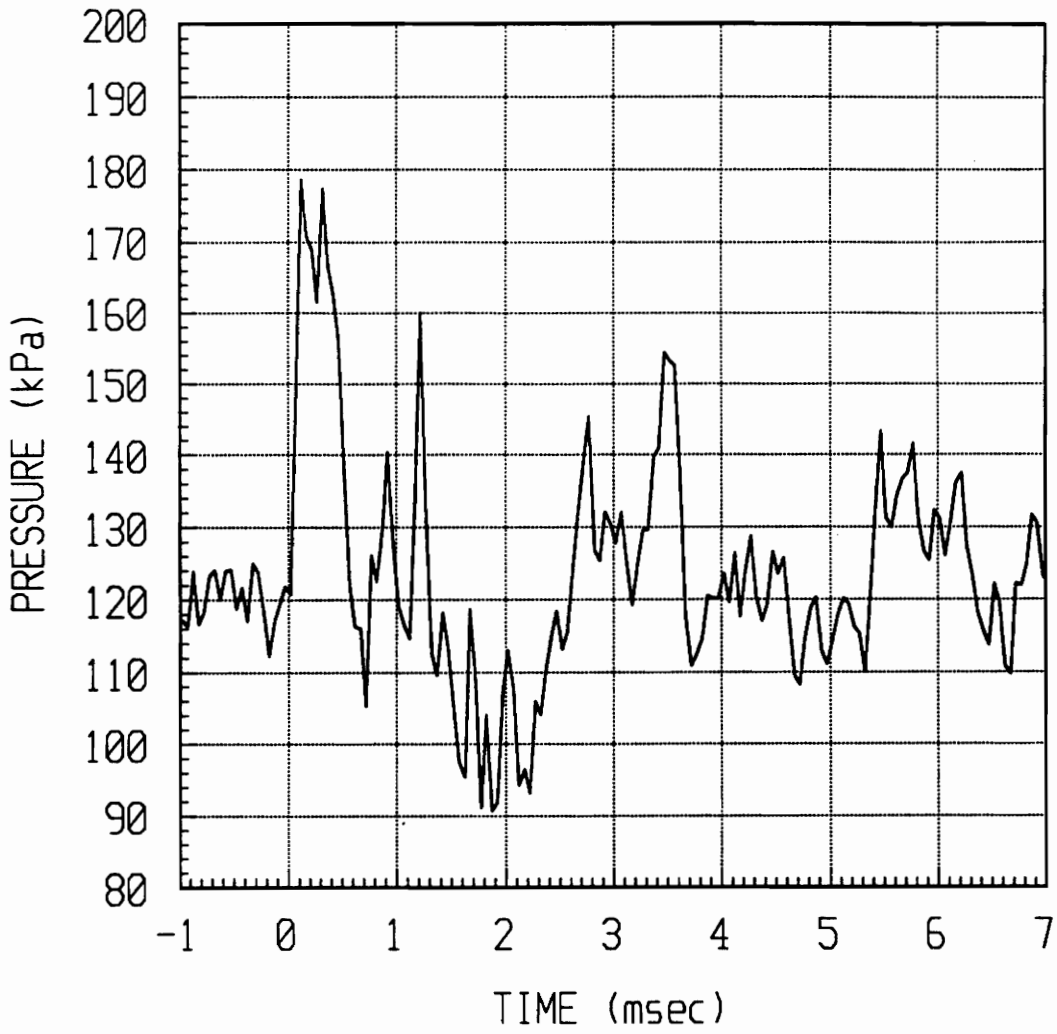

Figure B9: Boxcar-averaged absolute pressure vs time for Kulite #5, position 8.

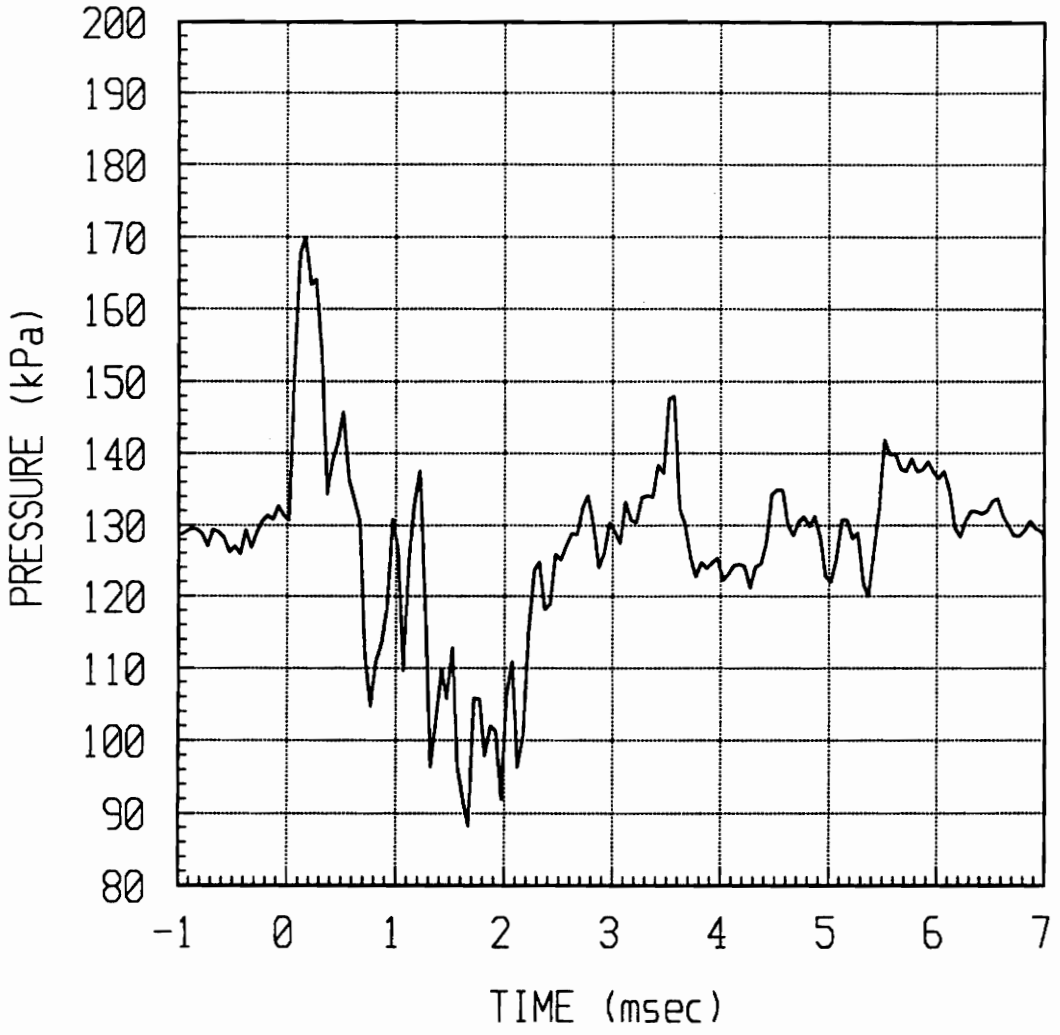

Figure B10: Boxcar-averaged absolute pressure vs time for Kulite #5, position 9.

11.0 Appendix C

Wake Pressure Profiles

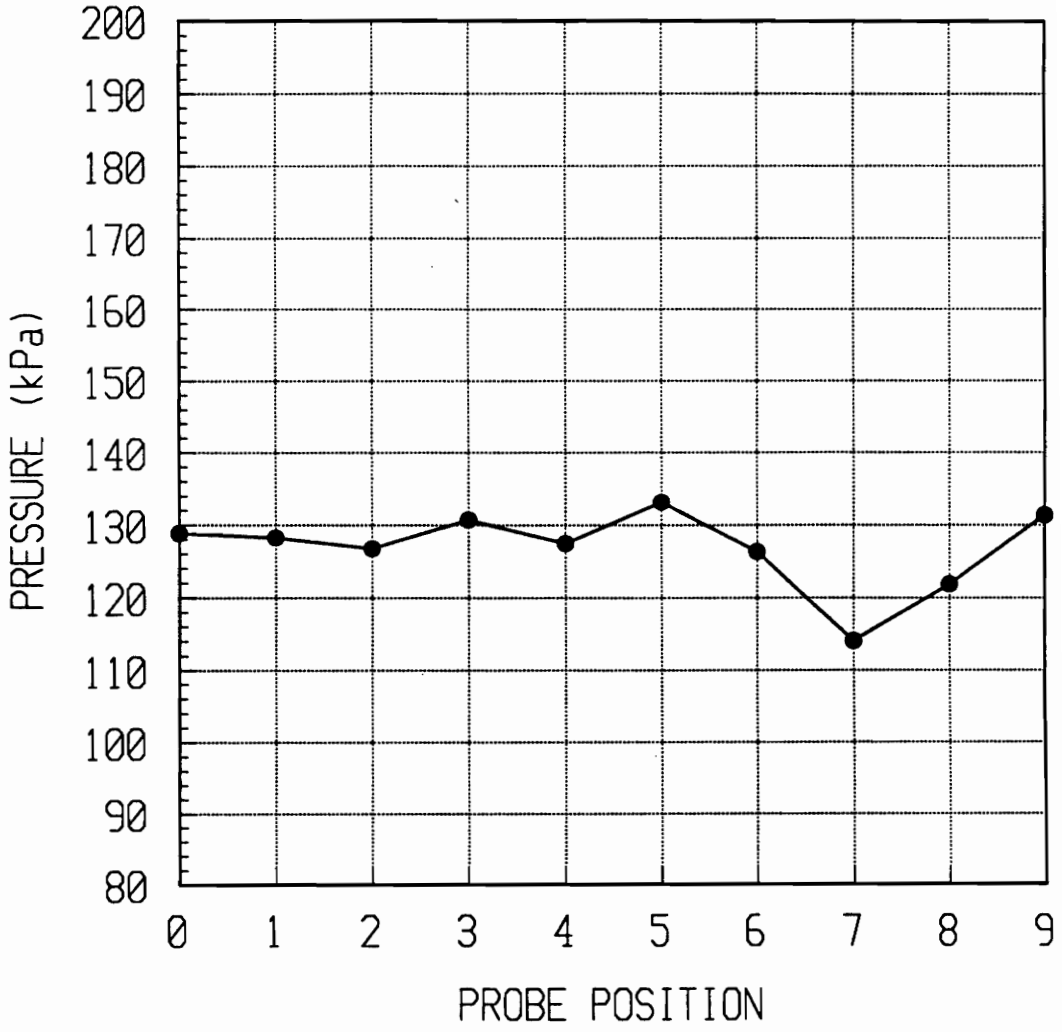

Figure C1: Wake absolute pressure profile at time = –0.03 msec.

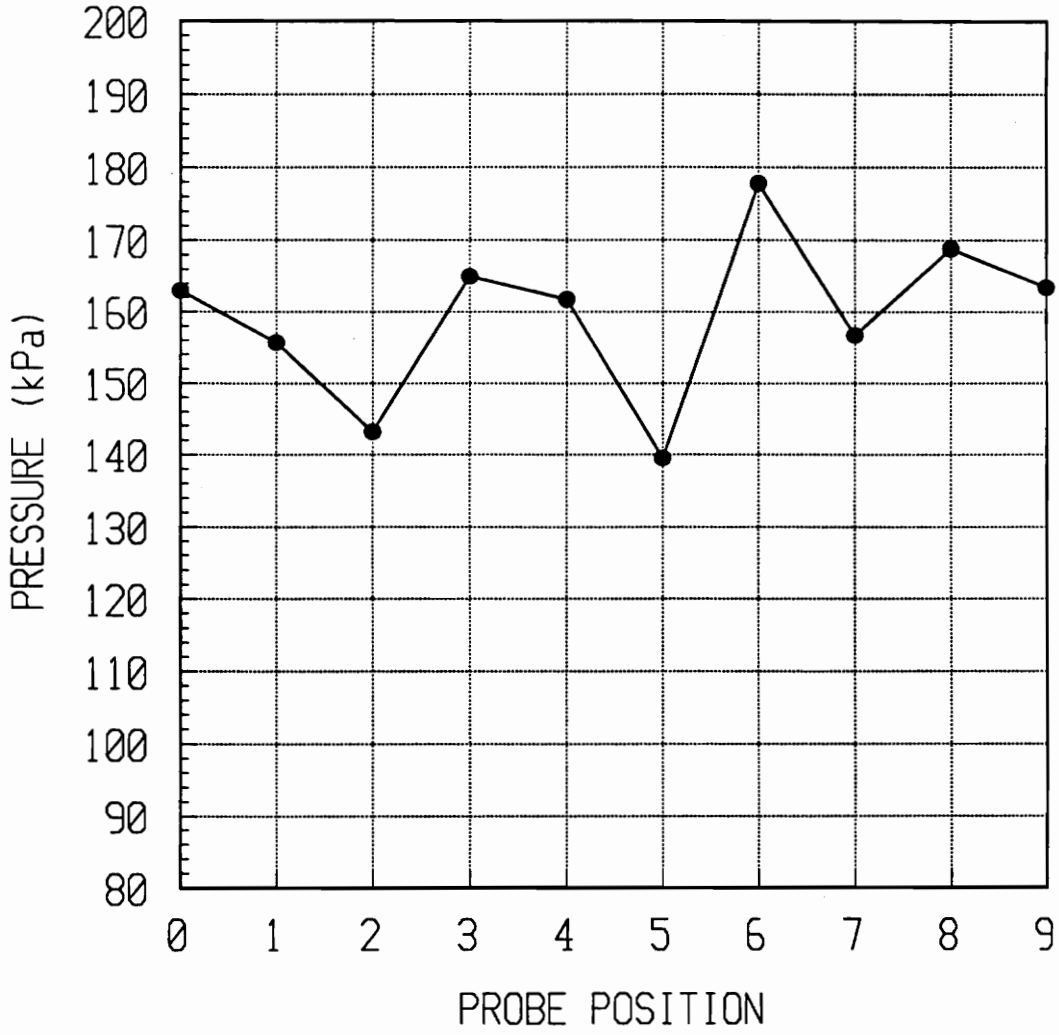

Figure C2: Wake absolute pressure profile at time = 0.22 msec.

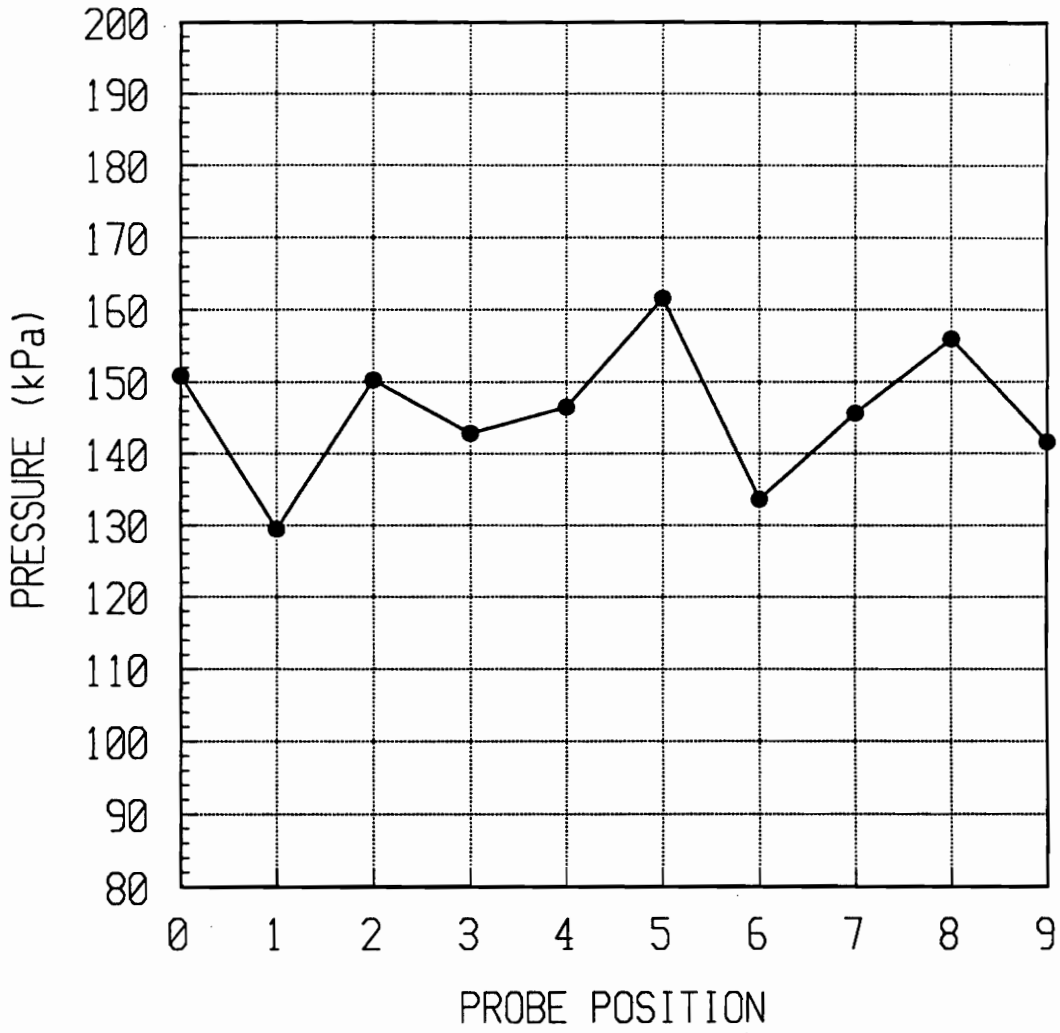

Figure C3: Wake absolute pressure profile at time = 0.47 msec.

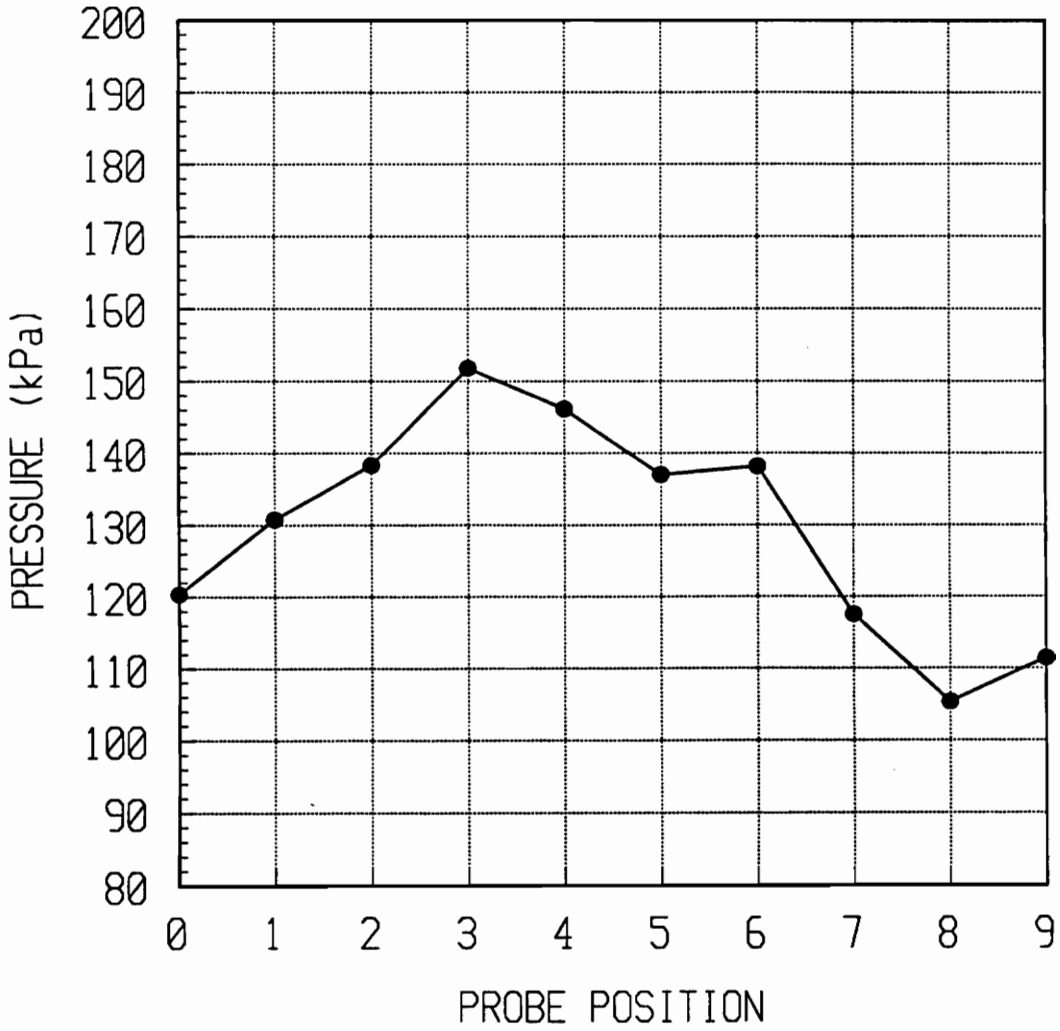

Figure C4: Wake absolute pressure profile at time = 0.72 msec.

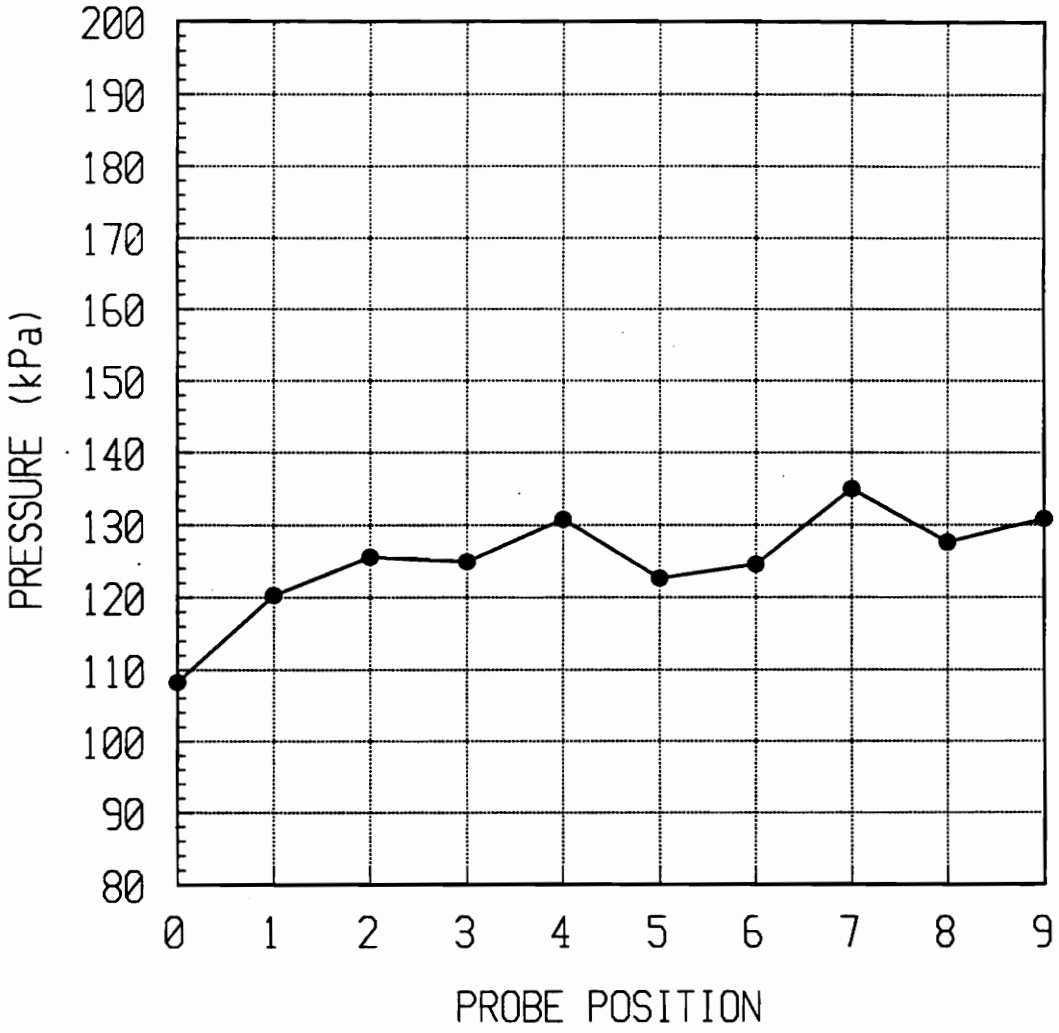

Figure C5: Wake absolute pressure profile at time = 0.97 msec.

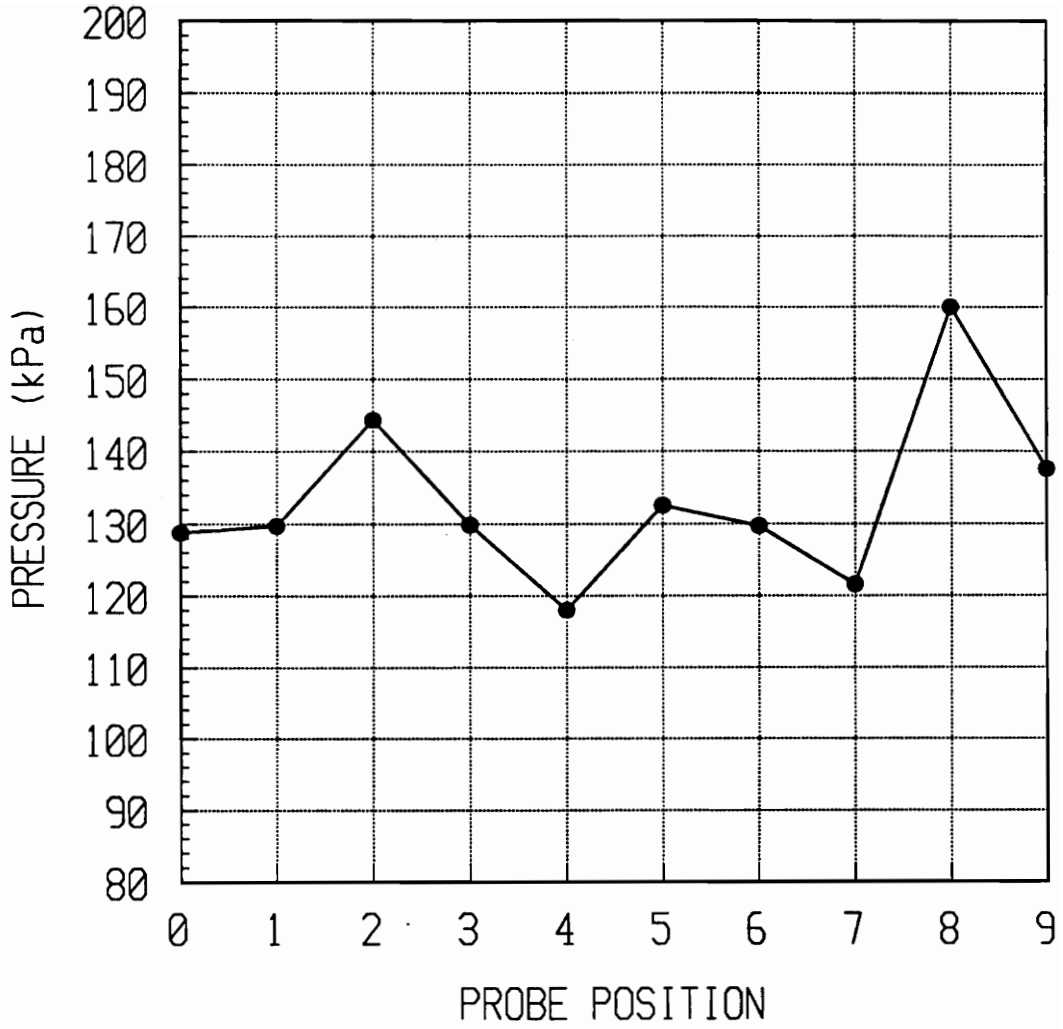

Figure C6: Wake absolute pressure profile at time = 1.22 msec.

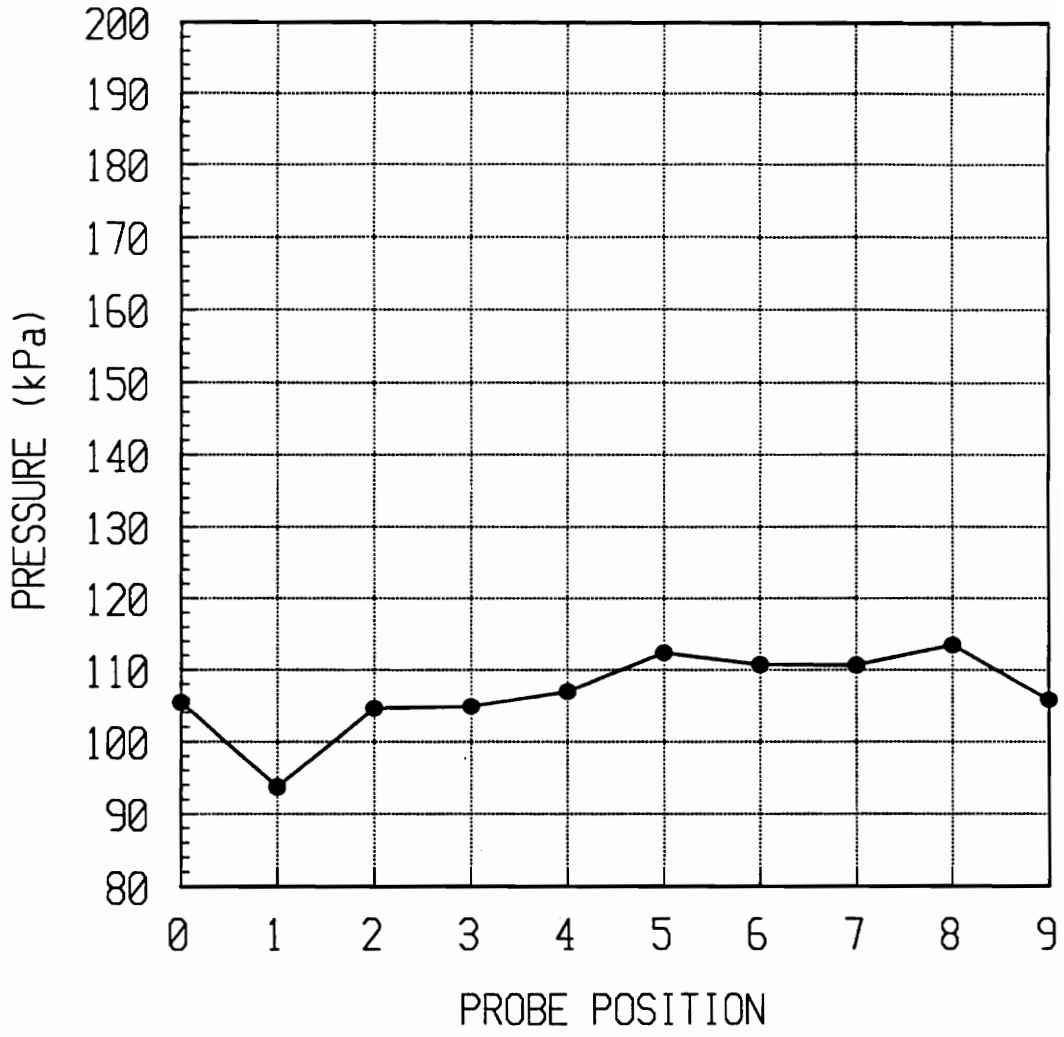

Figure C7: Wake absolute pressure profile at time = 1.47 msec.

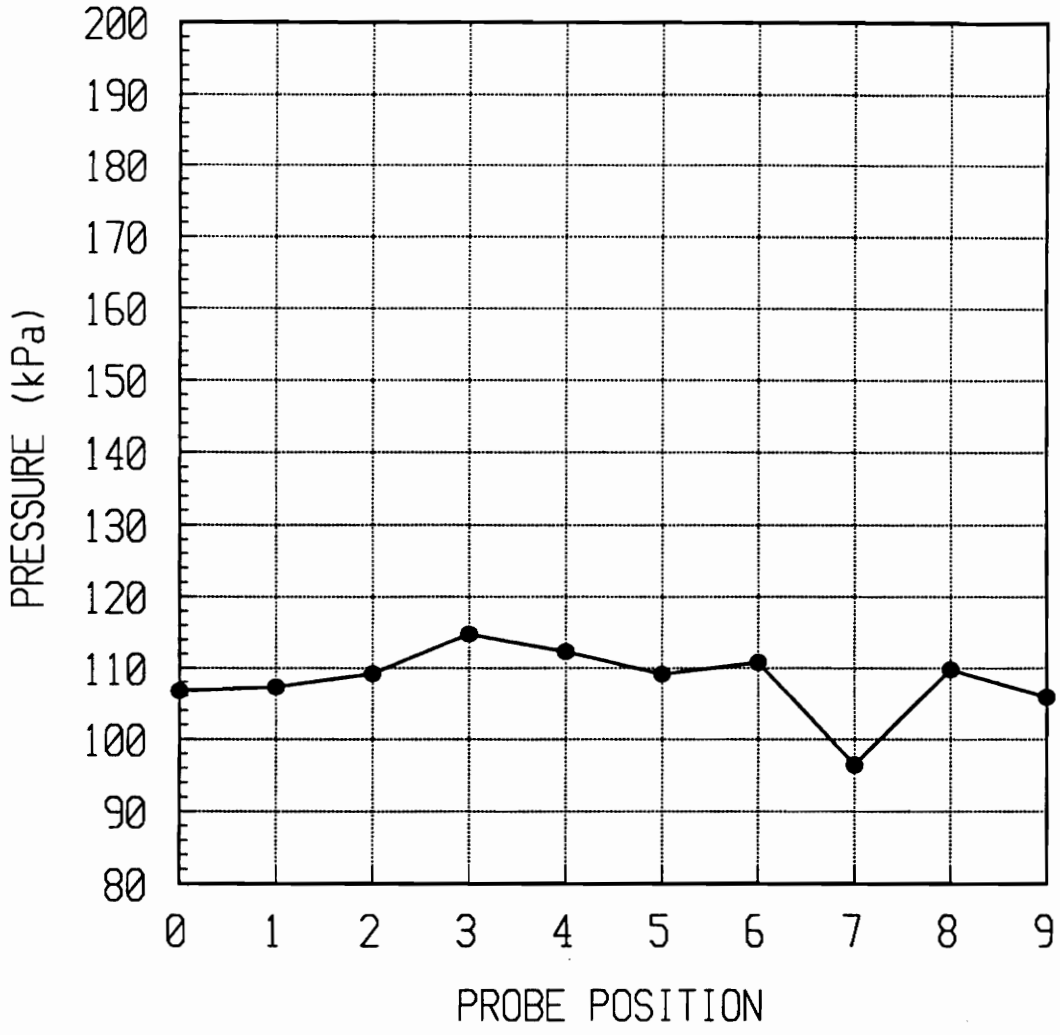

Figure C8: Wake absolute pressure profile at time = 1.72 msec.

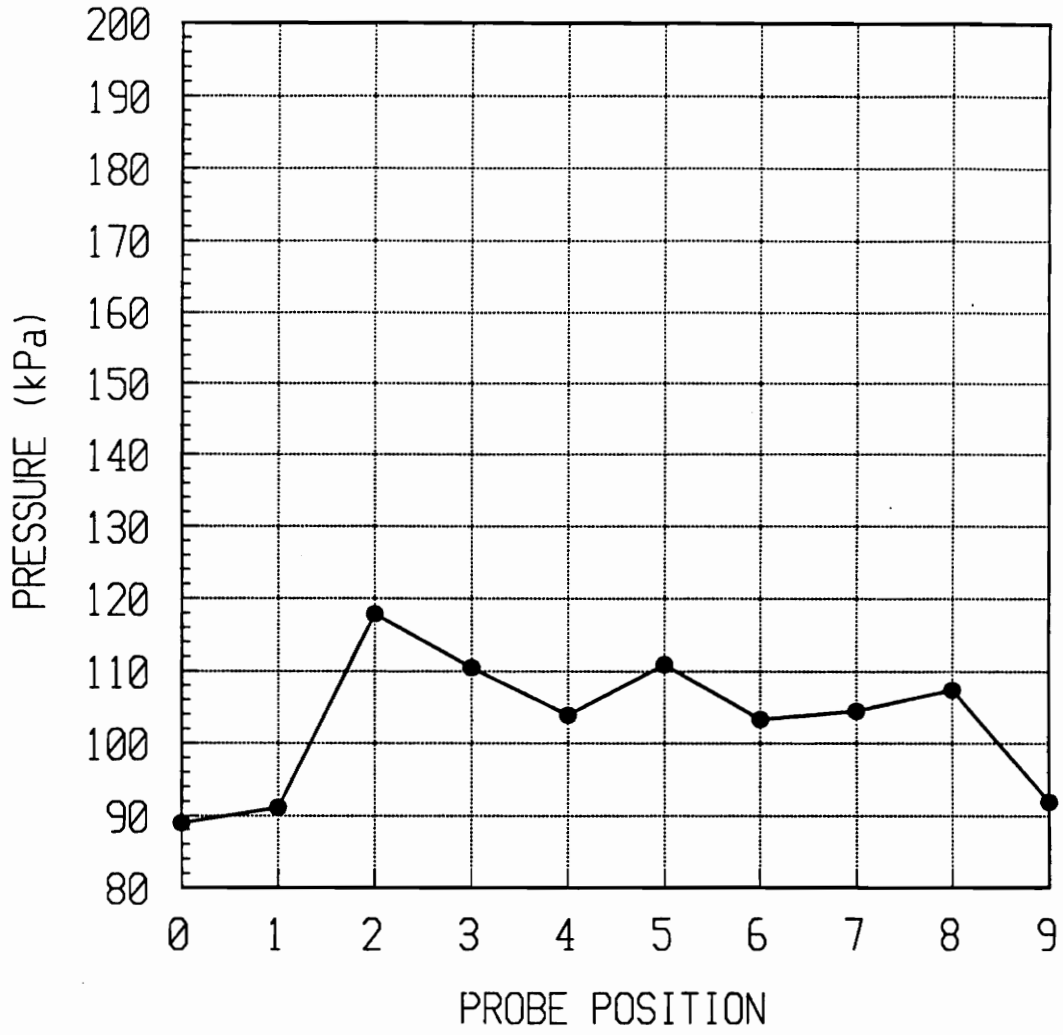

Figure C9: Wake absolute pressure profile at time = 1.97 msec.

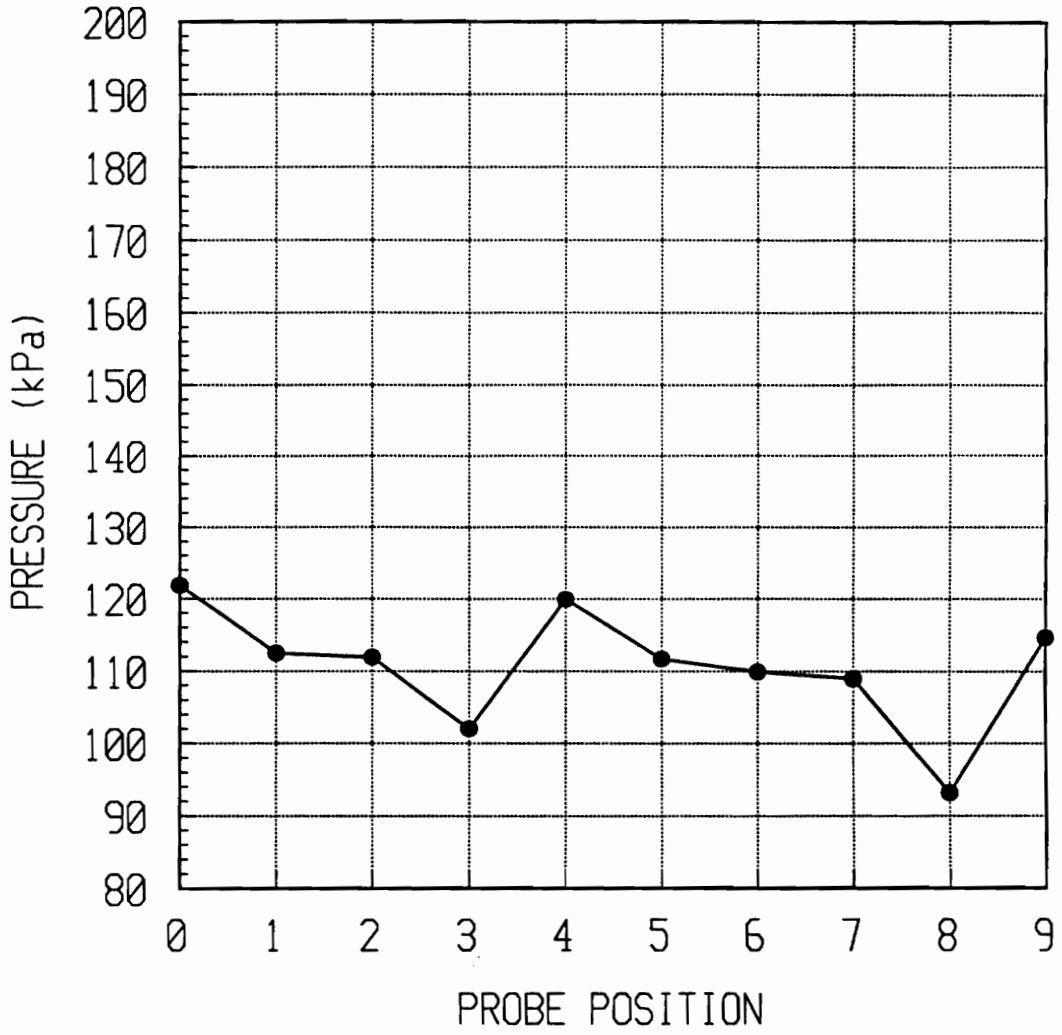

Figure C10: Wake absolute pressure profile at time = 2.22 msec.

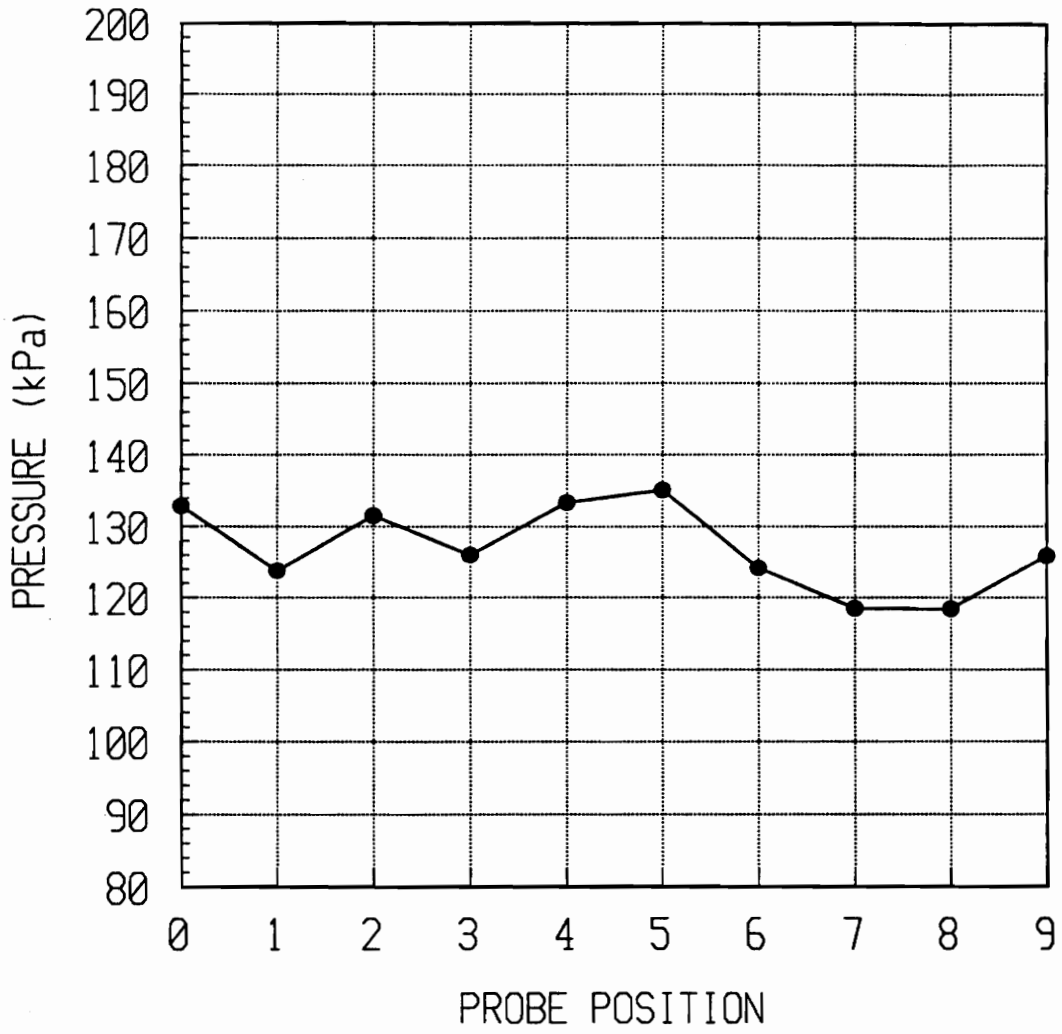

Figure C11: Wake absolute pressure profile at time = 2.47 msec.

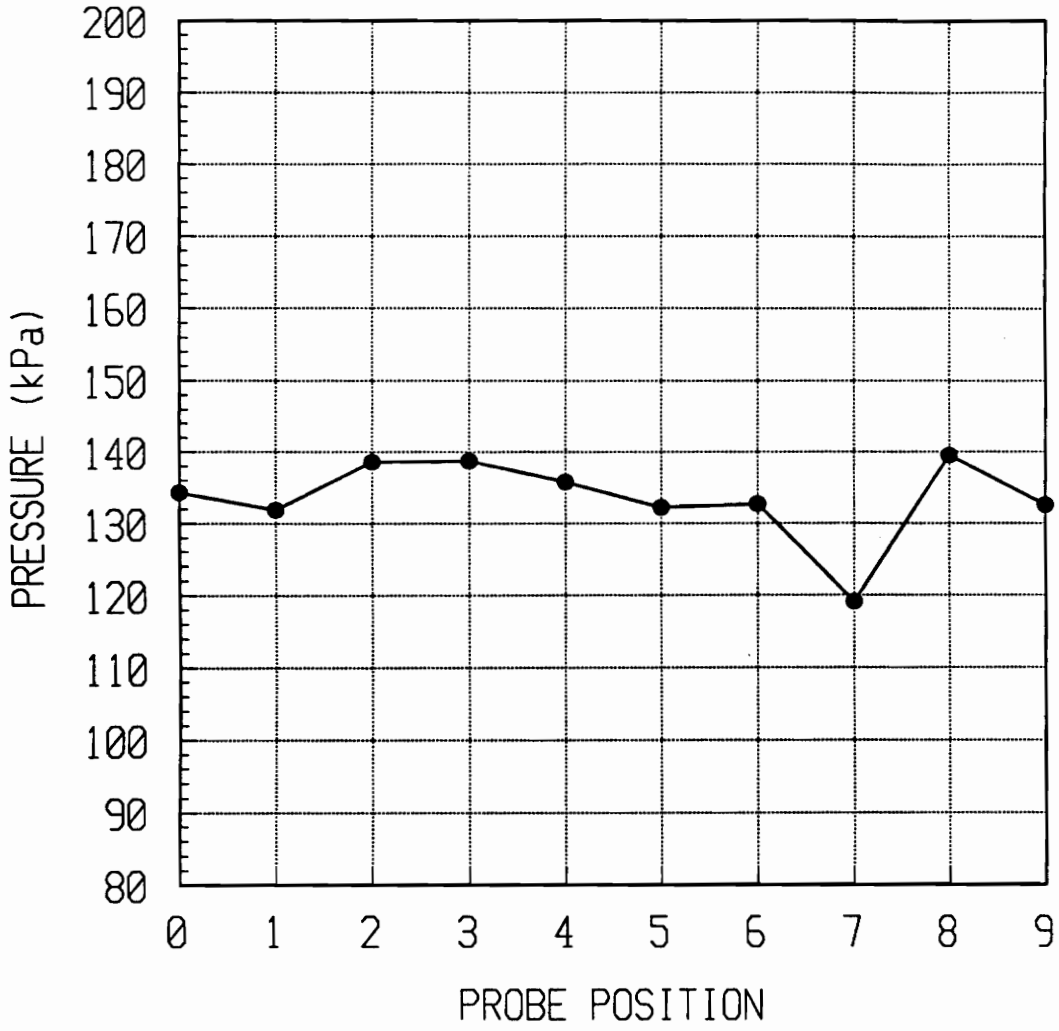

Figure C12: Wake absolute pressure profile at time = 2.72 msec.

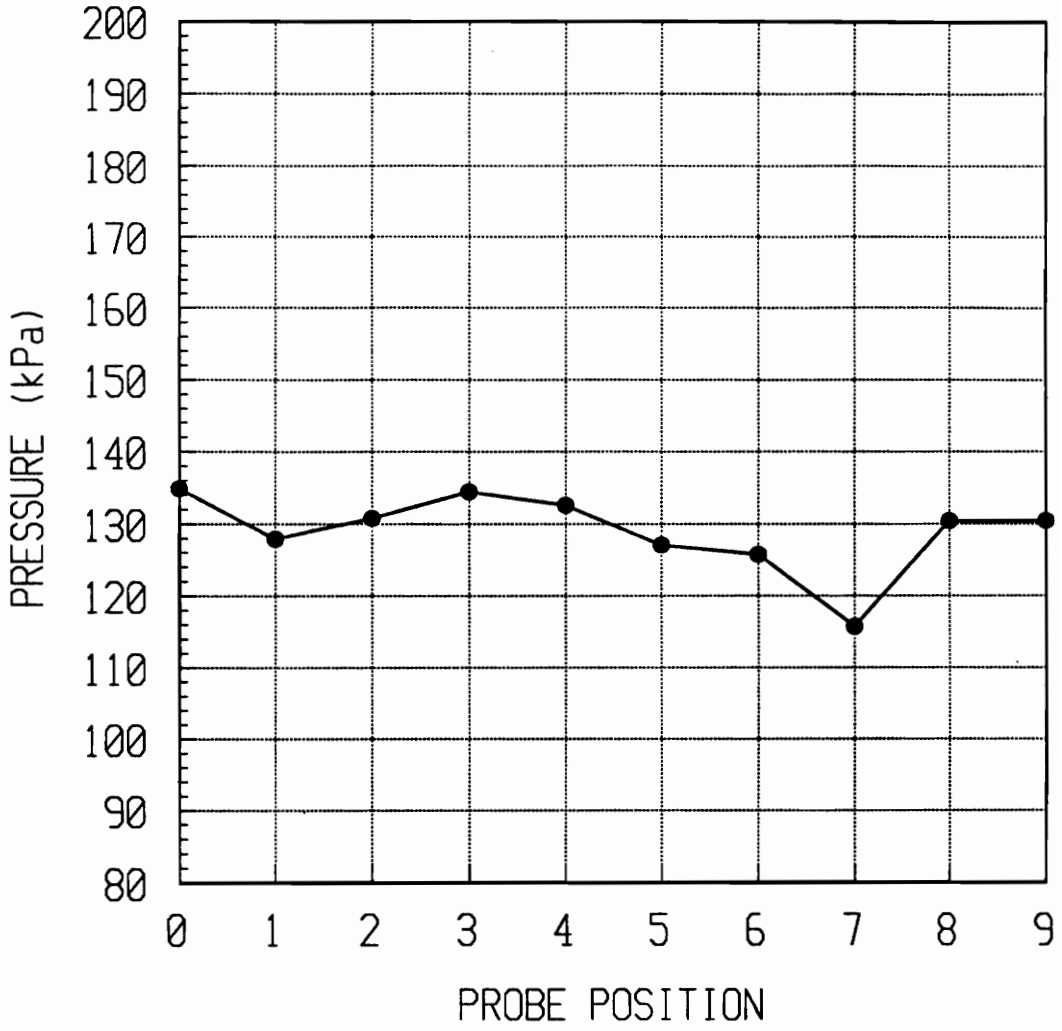

Figure C13: Wake absolute pressure profile at time = 2.97 msec.

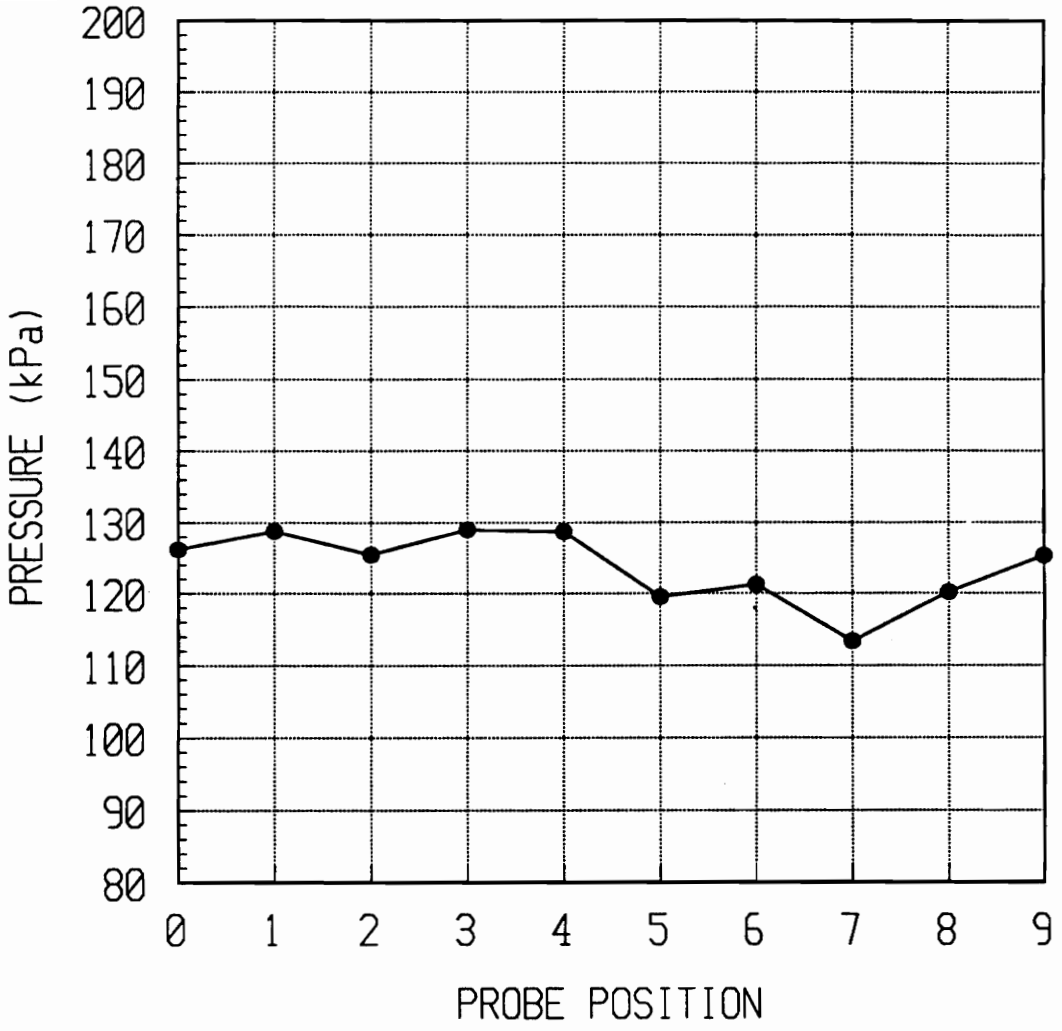

Figure C14: Wake absolute pressure profile at time = 3.97 msec.

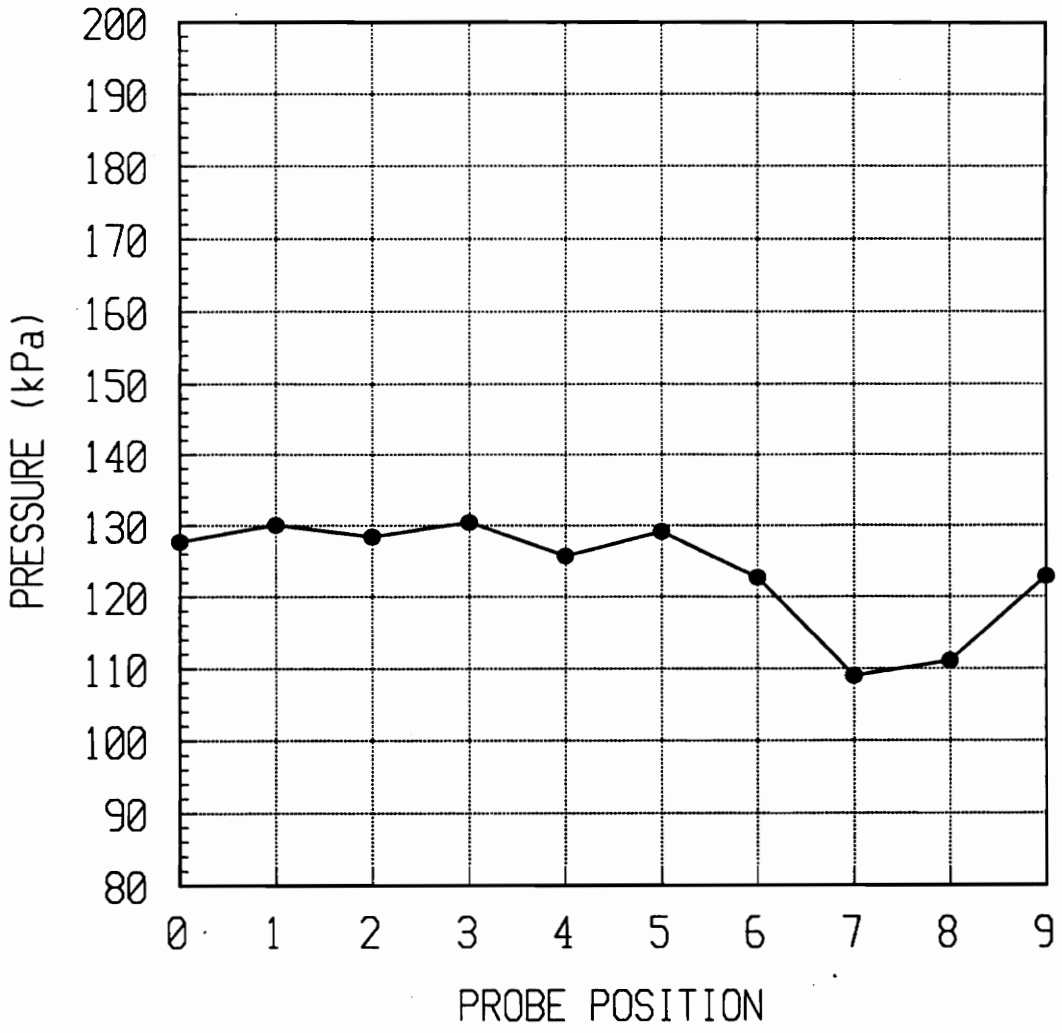

Figure C15: Wake absolute pressure profile at time = 4.97 msec.

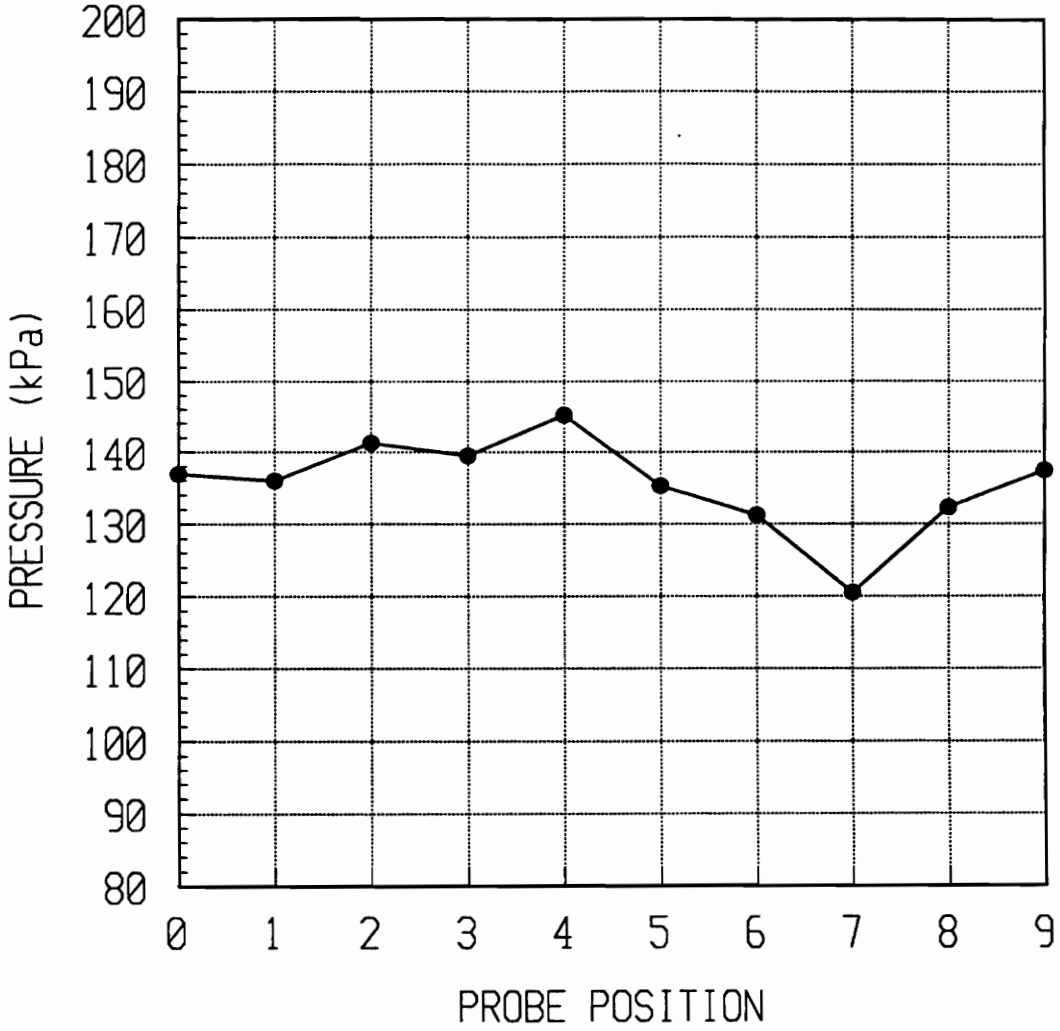

Figure C16: Wake absolute pressure profile at time = 5.97 msec.

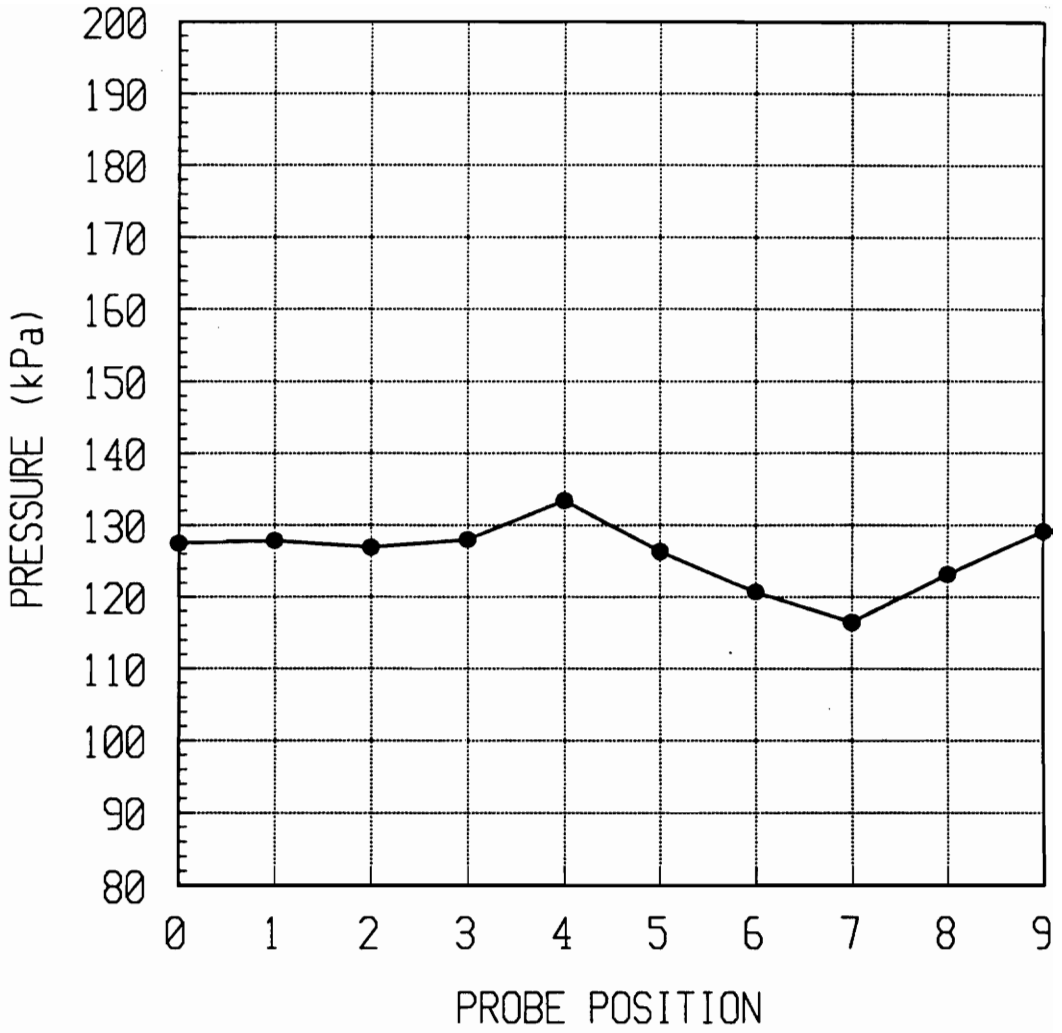

Figure C17: Wake absolute pressure profile at time = 6.97 msec.

12.0 Appendix D

Loss Coefficient Profiles

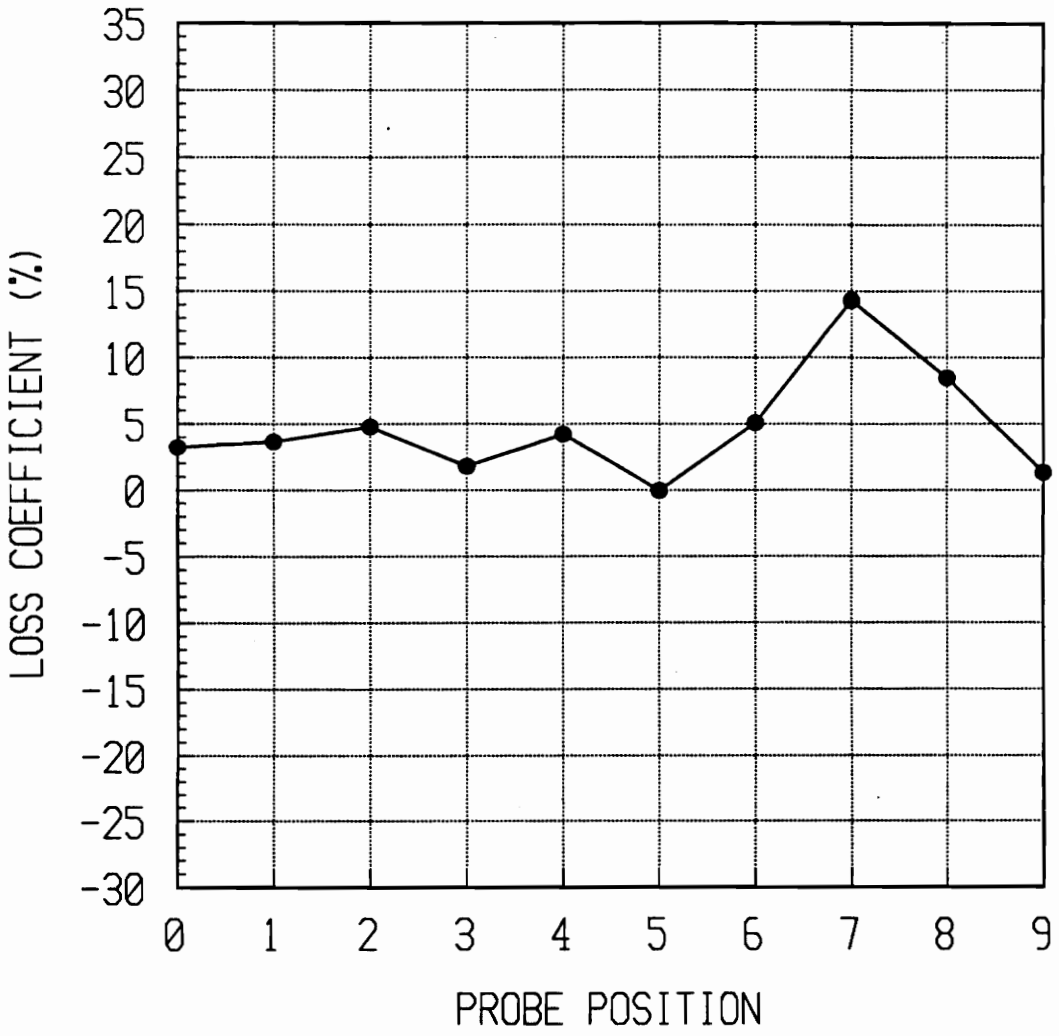

Figure D1: Loss coefficient profile at time = –0.03 msec.

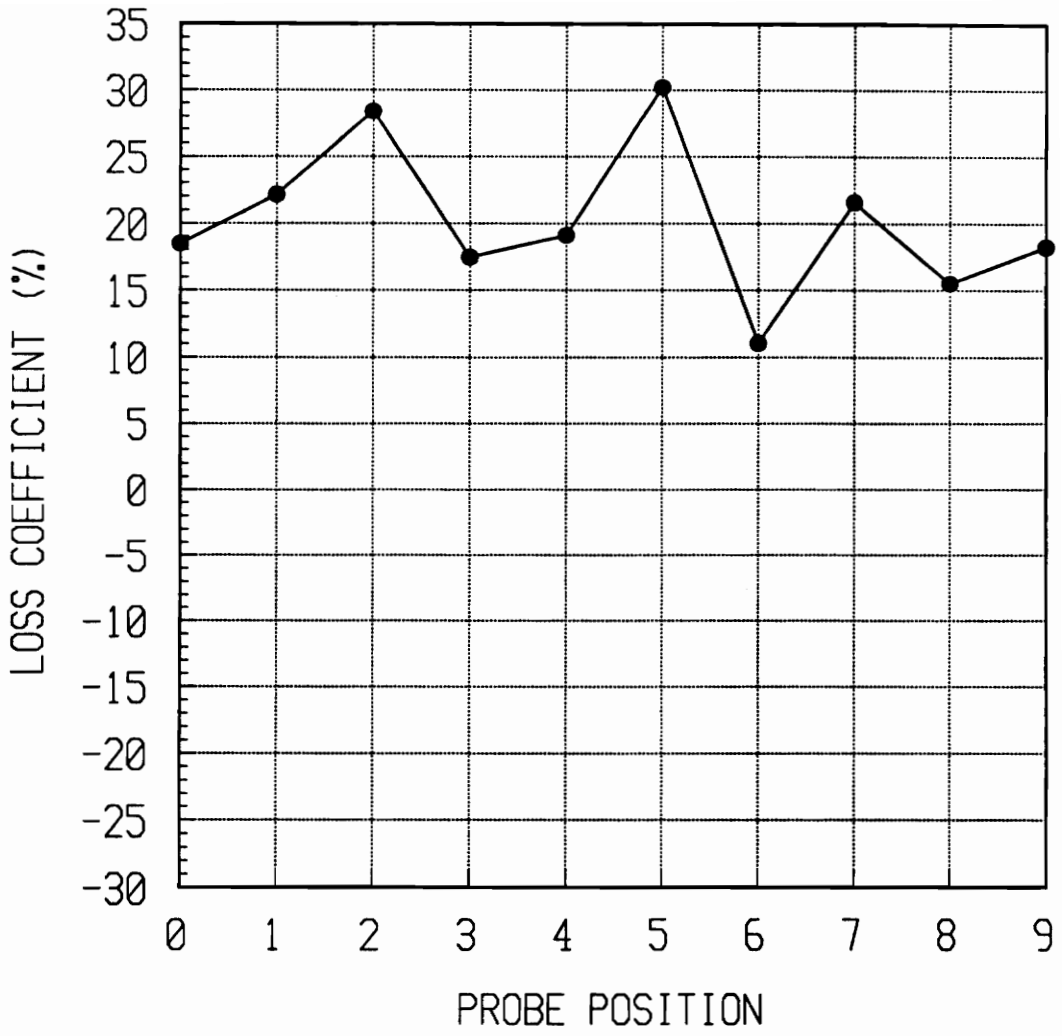

Figure D2: Loss coefficient profile at time = 0.22 msec.

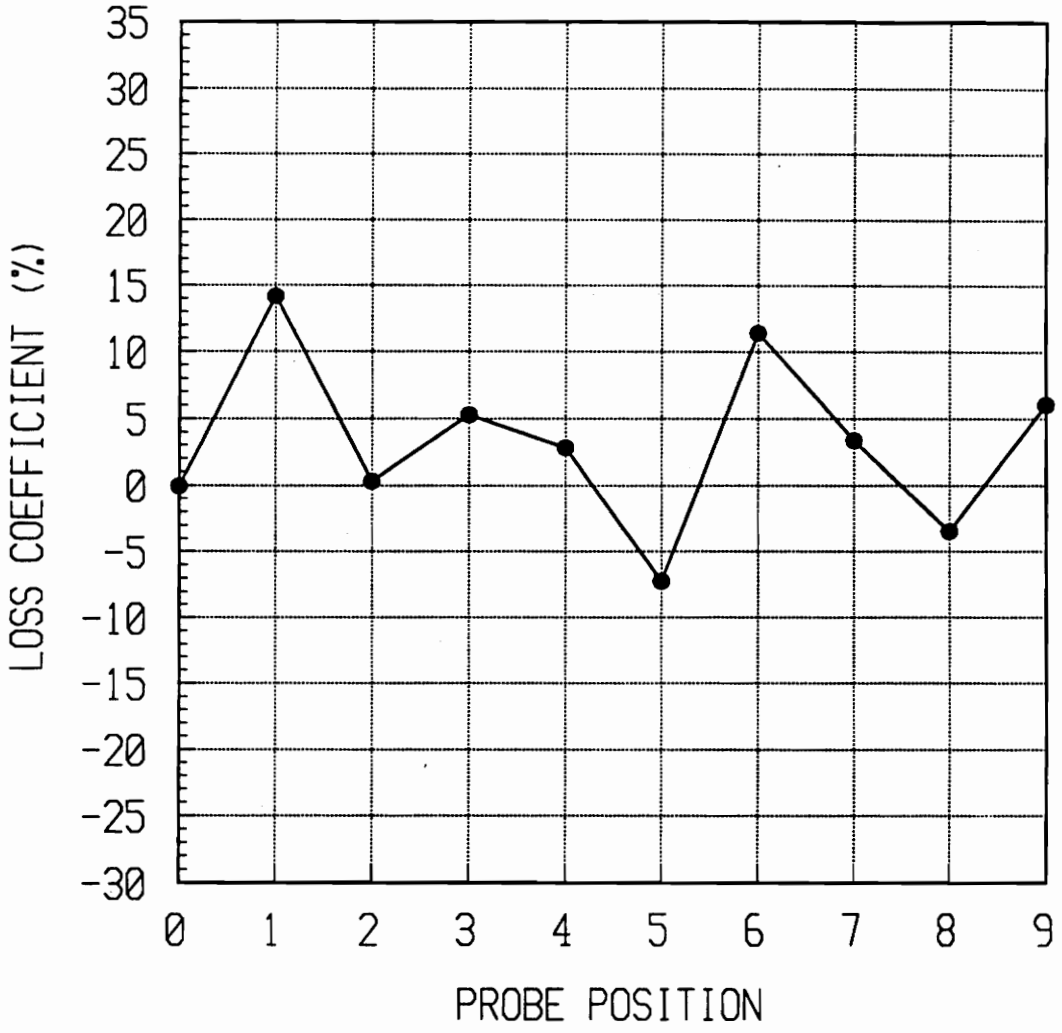

Figure D3: Loss coefficient profile at time = 0.47 msec.

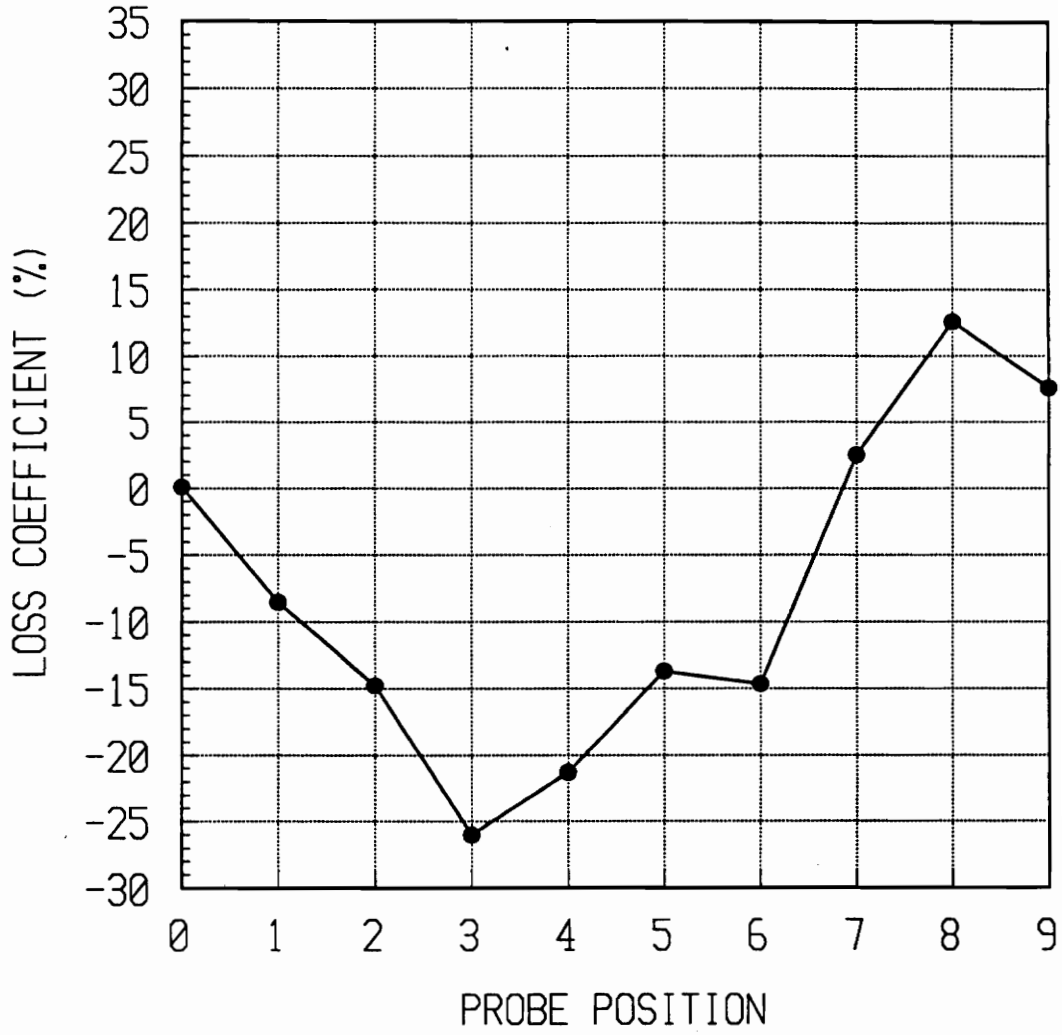

Figure D4: Loss coefficient profile at time = 0.72 msec.

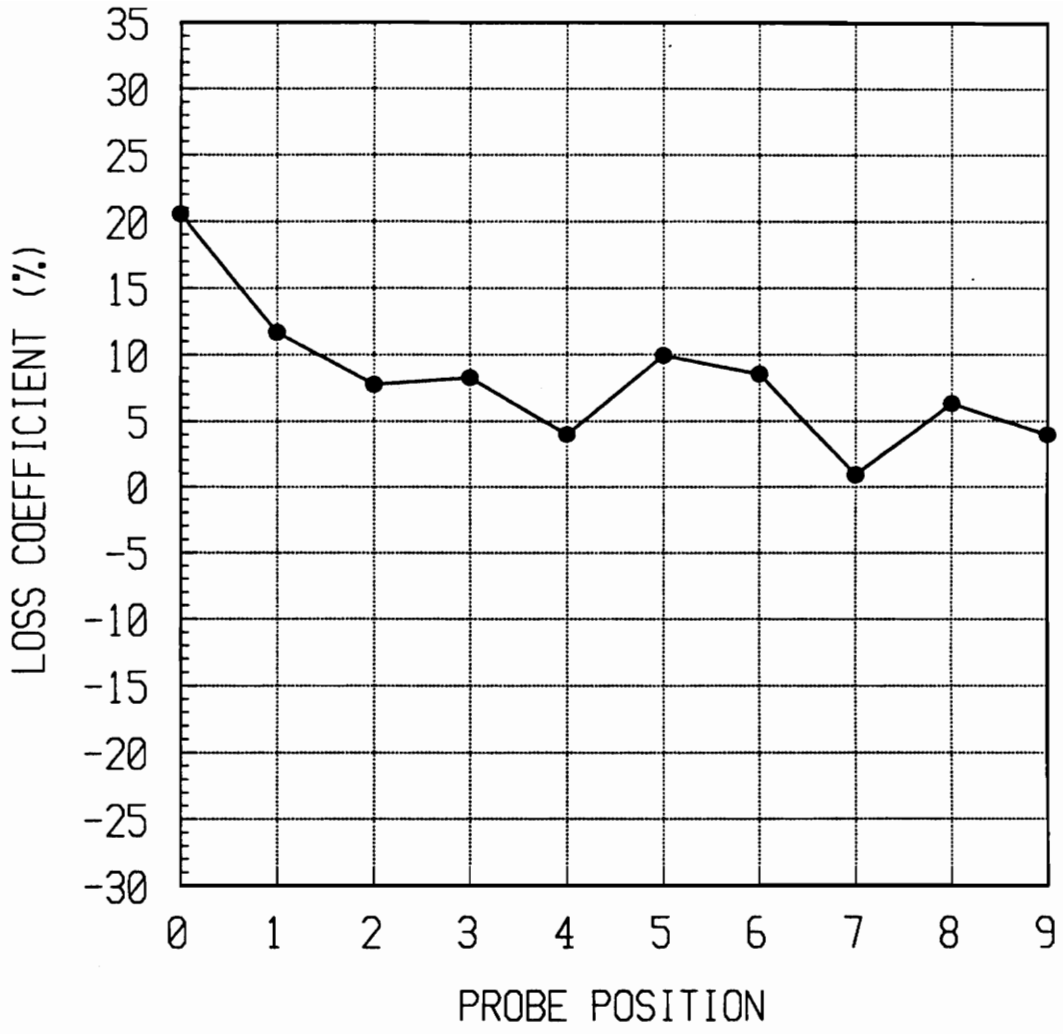

Figure D5: Loss coefficient profile at time = 0.97 msec.

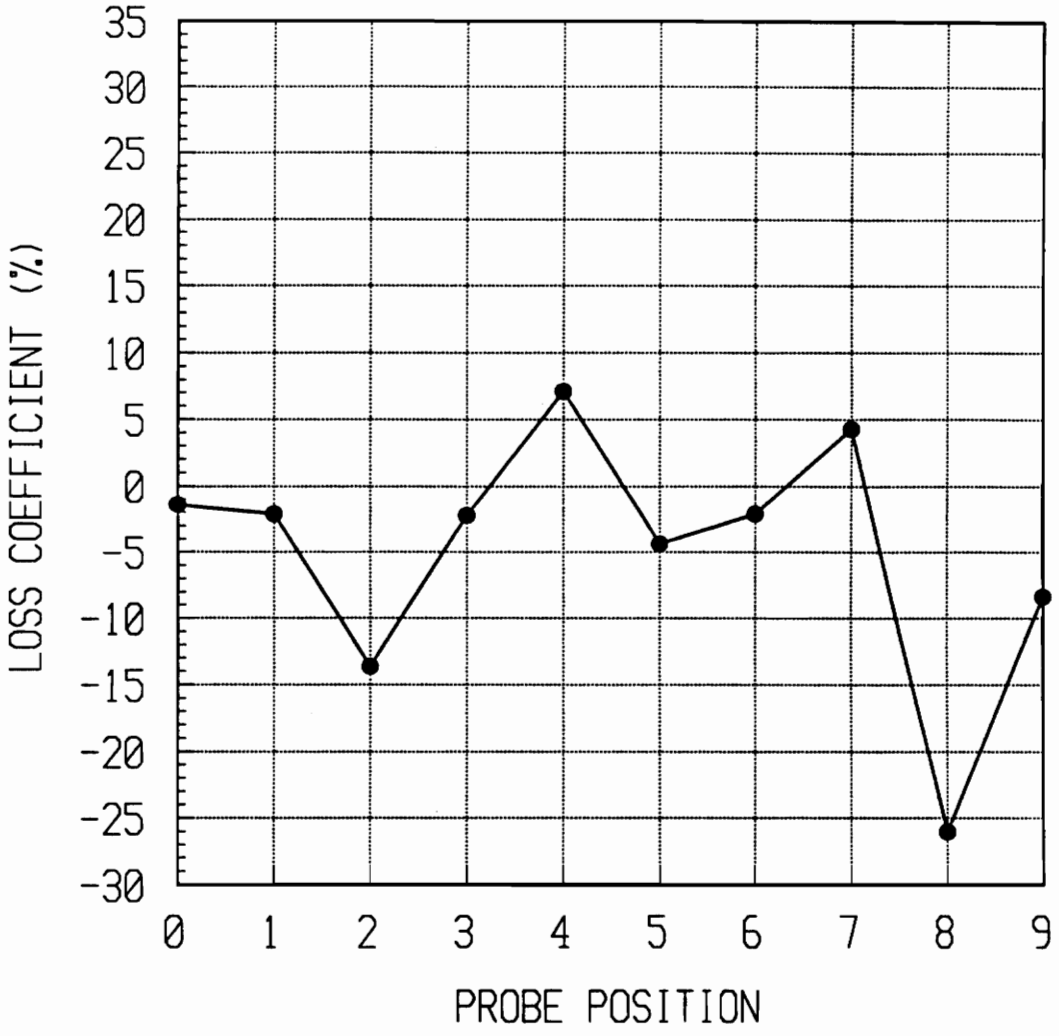

Figure D6: Loss coefficient profile at time = 1.22 msec.

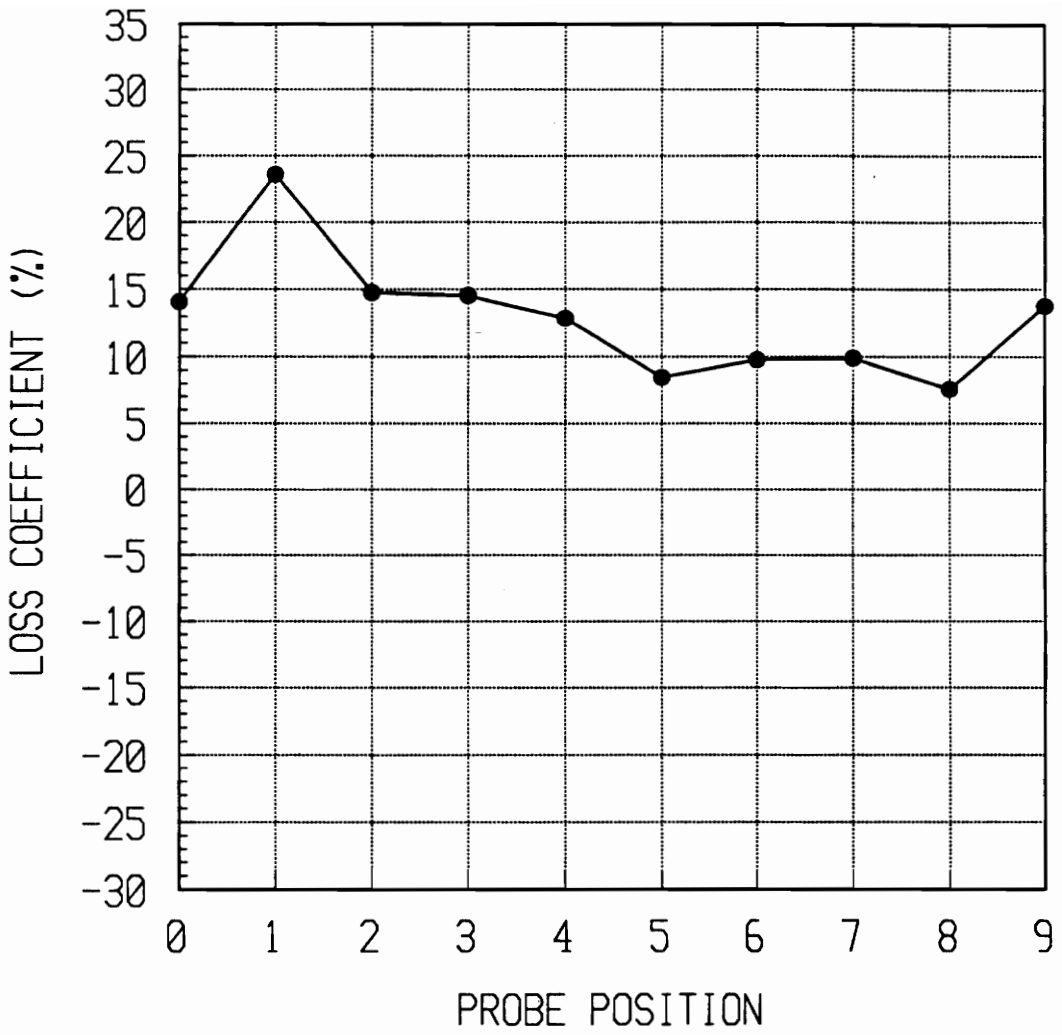

Figure D7: Loss coefficient profile at time = 1.47 msec.

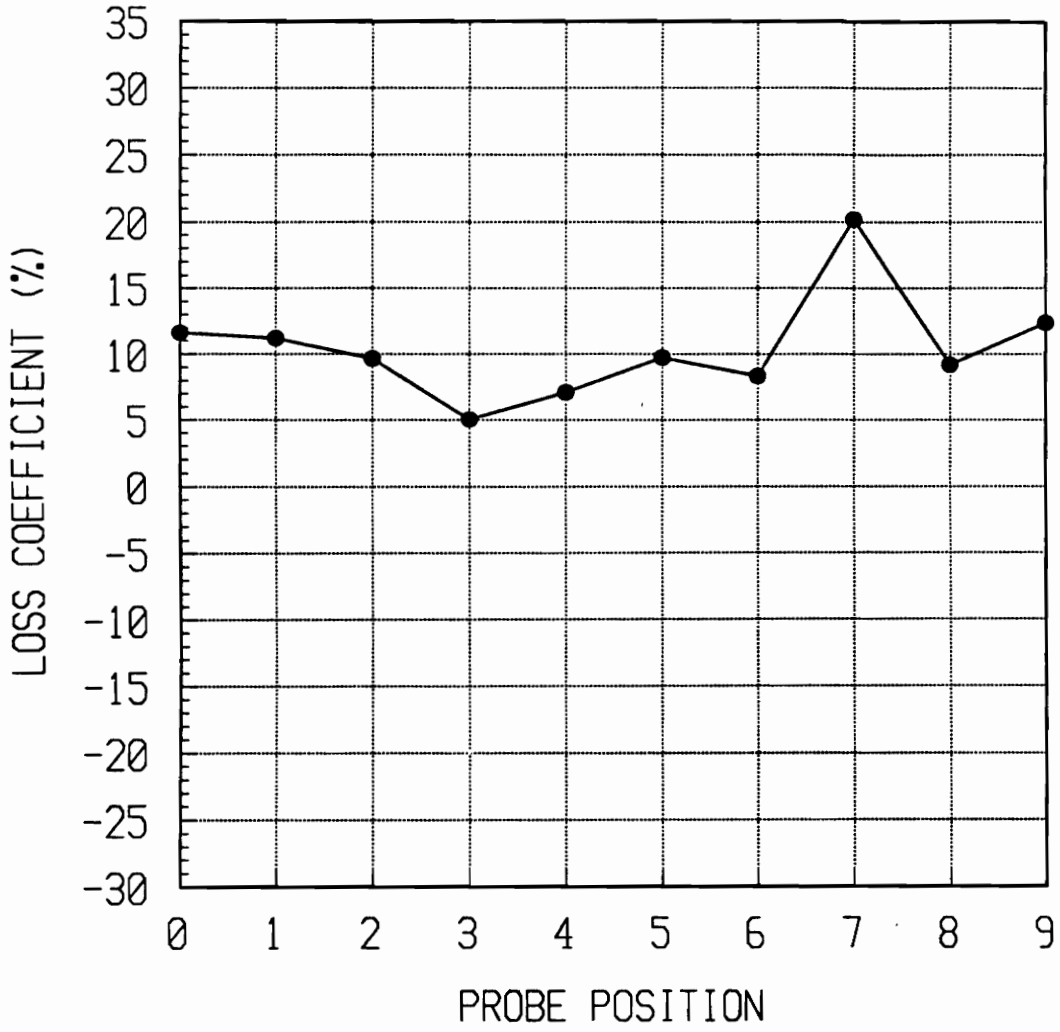

Figure D8: Loss coefficient profile at time = 1.72 msec.

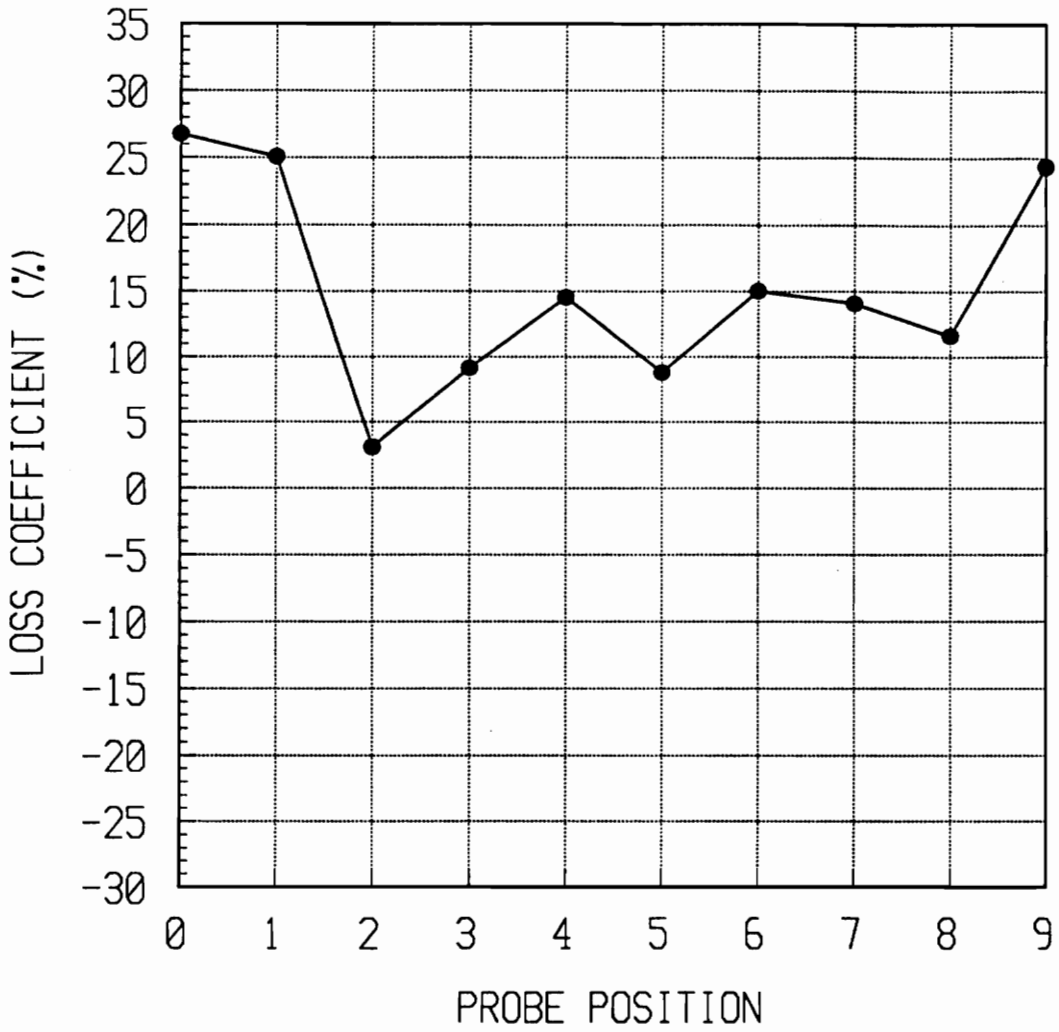

Figure D9: Loss coefficient profile at time = 1.97 msec.

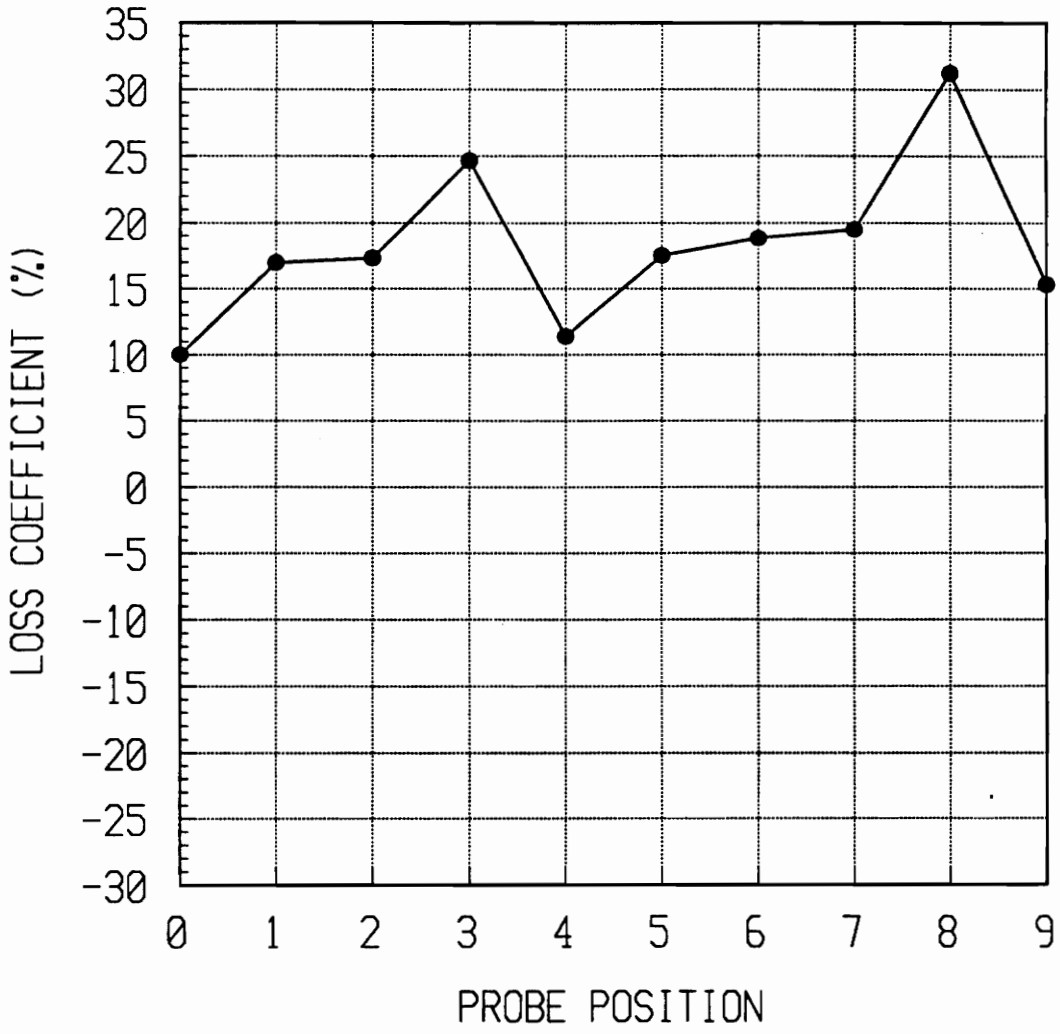

Figure D10: Loss coefficient profile at time = 2.22 msec.

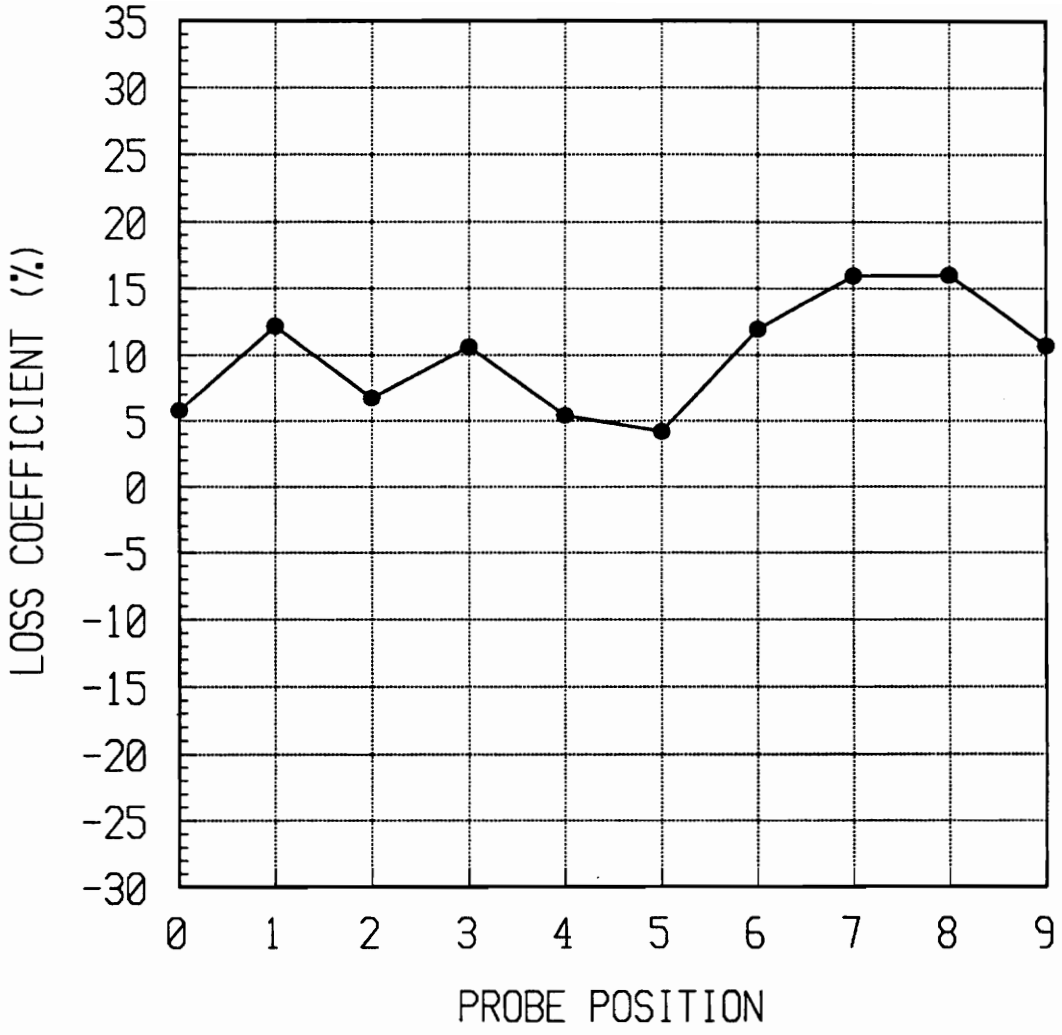

Figure D11: Loss coefficient profile at time = 2.47 msec.

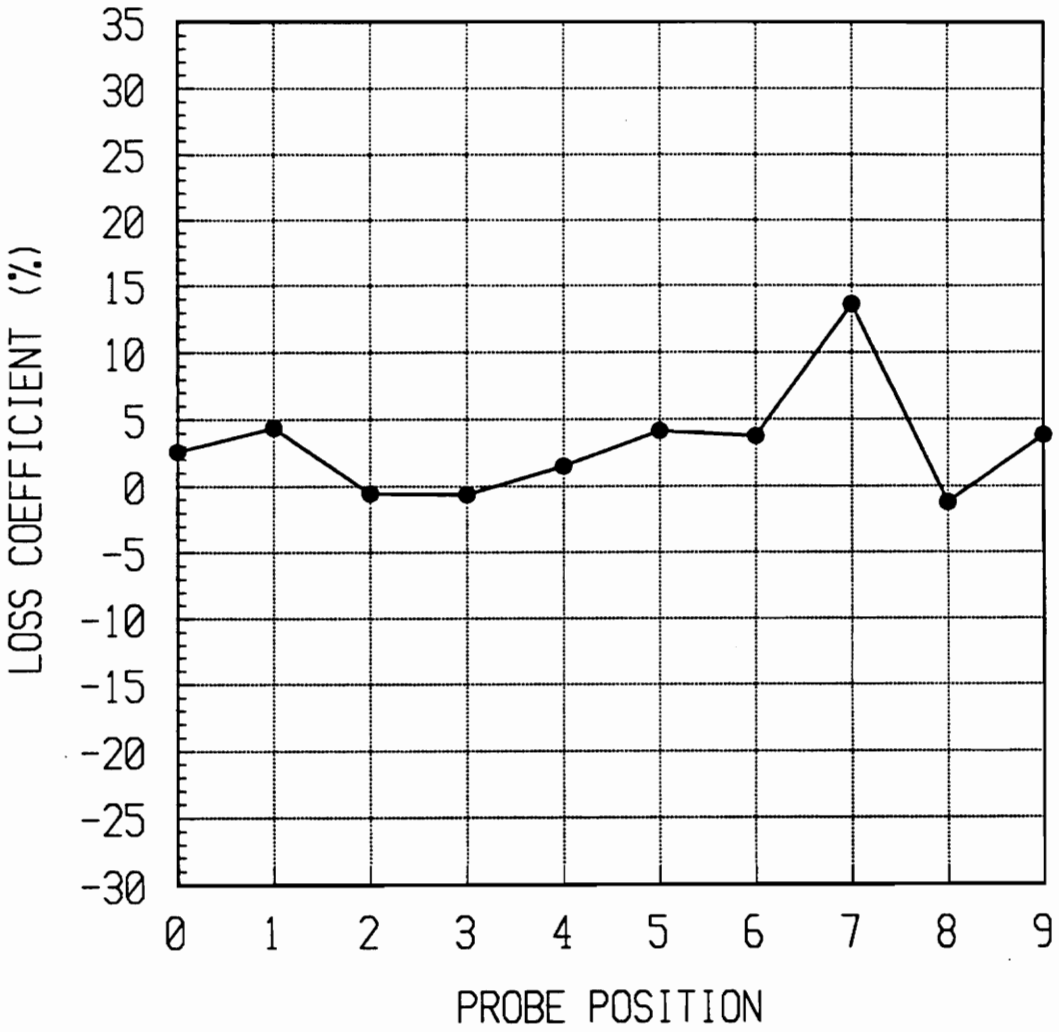

Figure D12: Loss coefficient profile at time = 2.72 msec.

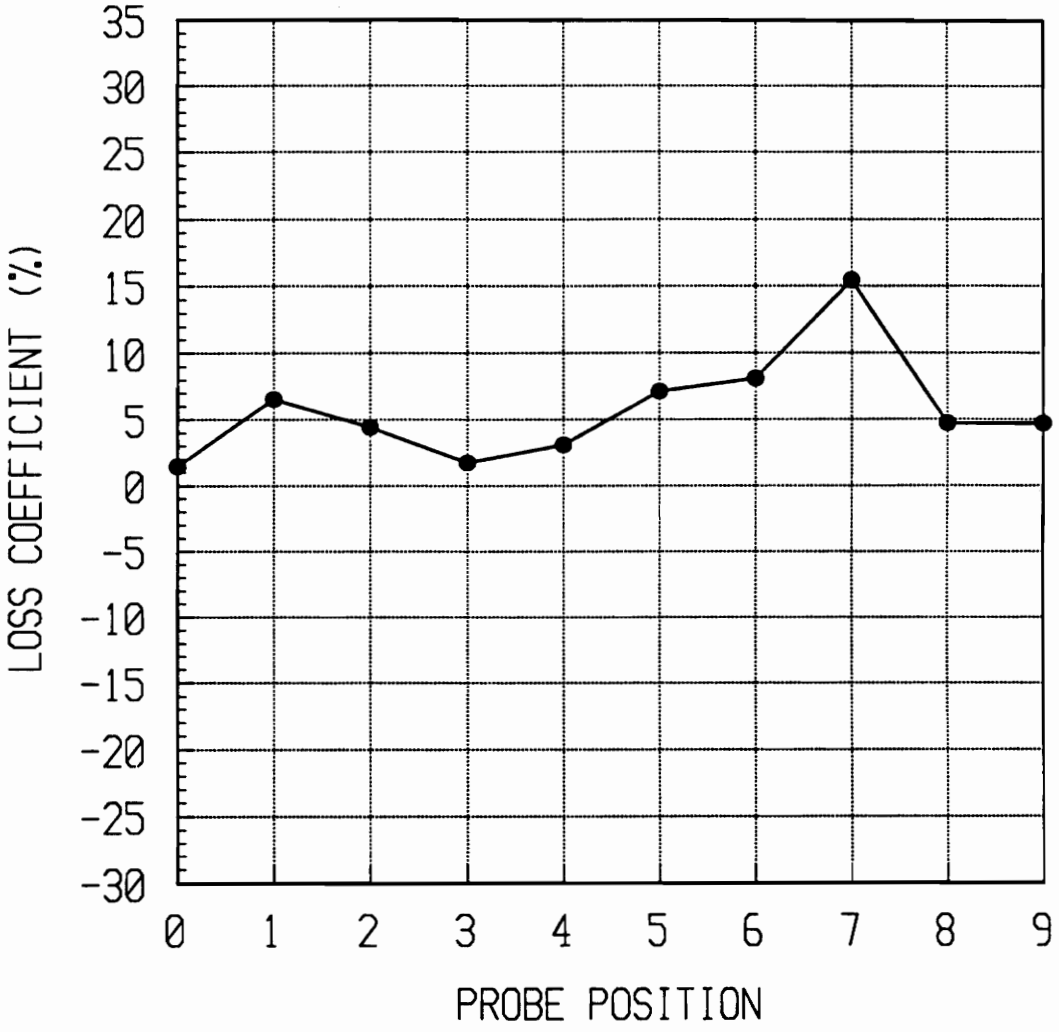

Figure D13: Loss coefficient profile at time = 2.97 msec.

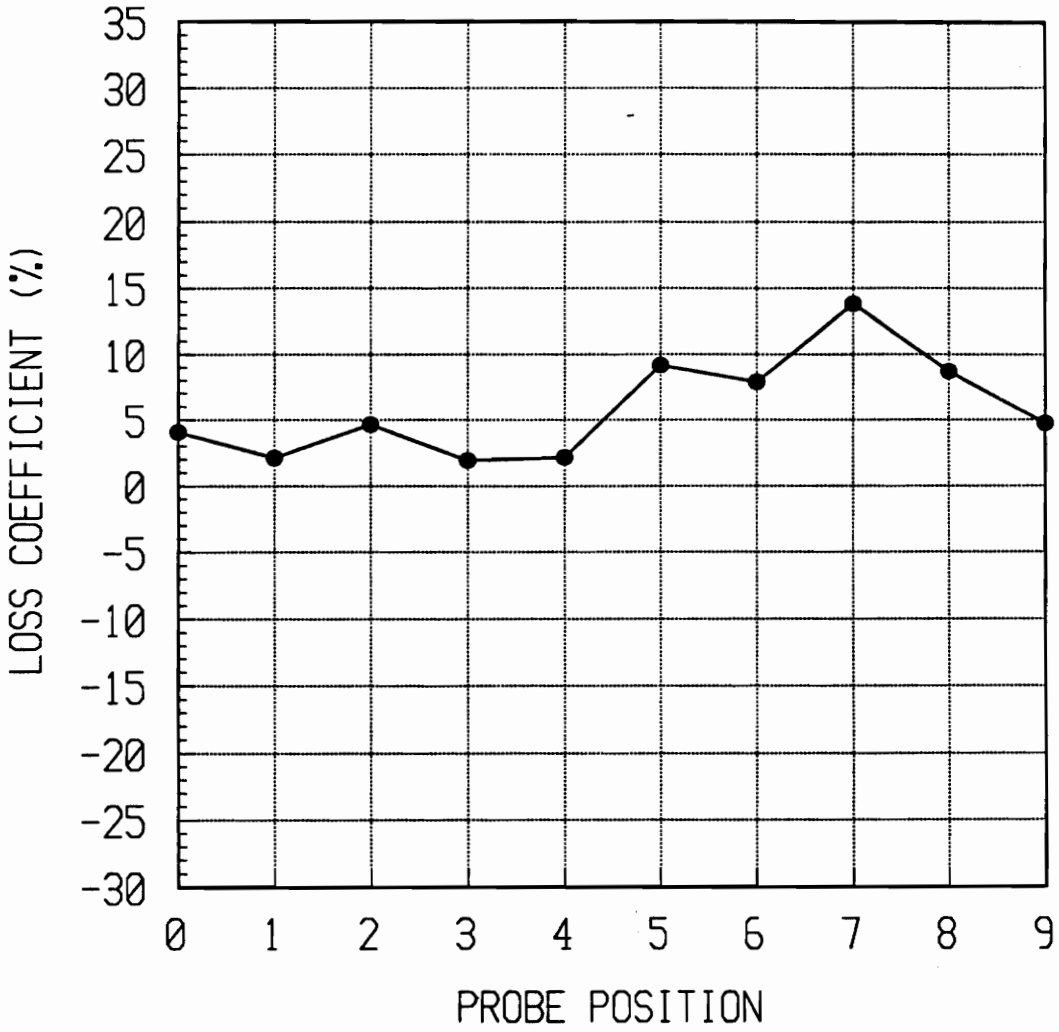

Figure D14: Loss coefficient profile at time = 3.97 msec.

Vita

The author was born on June 19, 1967 in Newport News, Virginia. He graduated from York High School in Yorktown, Virginia in June of 1985. He completed his B.S.M.E. degree in May of 1990 at Virginia Tech, where he also participated in the Cooperative Education Program at the Yorktown Power Station. Deciding to stick it out a little bit longer, he stayed to attend graduate school at Virginia Tech, during which time he married Renée Bush. They are currently attempting to raise their first family member, a Shih Tzu puppy named Tucker with inexhaustible enthusiasm — on numerous occasions has he gladly injected his personal comments during the penning of this thesis! The author has accepted a position at Westinghouse Energy Systems in Monroeville, PA upon graduation from the master's program.